Max-Planck-Institut
für Meteorologie

MAX-PLANCK-GESELLSCHAFT

Impact of thermodynamic surface properties on climate and climate change in a radiative-convective equilibrium version of ECHAM6

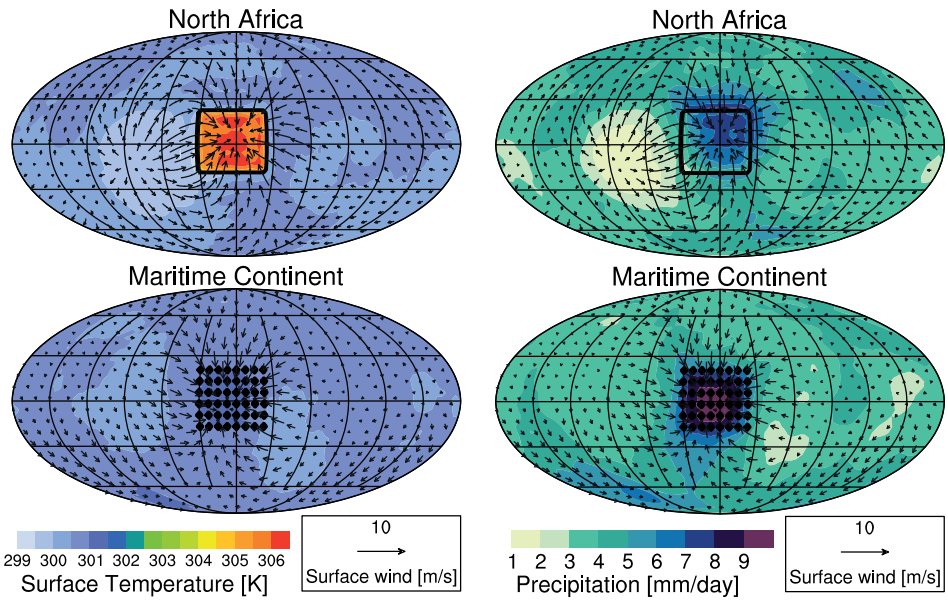

Tobias Becker

Hamburg 2014

Berichte zur Erdsystemforschung
Reports on Earth System Science

156
2014

Hinweis

Die Berichte zur Erdsystemforschung werden vom Max-Planck-Institut für Meteorologie in Hamburg in unregelmäßiger Abfolge herausgegeben.

Sie enthalten wissenschaftliche und technische Beiträge, inklusive Dissertationen.

Die Beiträge geben nicht notwendigerweise die Auffassung des Instituts wieder.

Die "Berichte zur Erdsystemforschung" führen die vorherigen Reihen "Reports" und "Examensarbeiten" weiter.

Notice

The Reports on Earth System Science are published by the Max Planck Institute for Meteorology in Hamburg. They appear in irregular intervals.

They contain scientific and technical contributions, including Ph. D. theses.

The Reports do not necessarily reflect the opinion of the Institute.

The "Reports on Earth System Science" continue the former "Reports" and "Examensarbeiten" of the Max Planck Institute.

Anschrift / Address

Max-Planck-Institut für Meteorologie
Bundesstrasse 53
20146 Hamburg
Deutschland

Tel./Phone: +49 (0)40 4 11 73 - 0
Fax: +49 (0)40 4 11 73 - 298

name.surname@mpimet.mpg.de
www.mpimet.mpg.de

Layout

Bettina Diallo and Norbert P. Noreiks
Communication

Copyright

Max-Planck-Institut
für Meteorologie

MAX-PLANCK-GESELLSCHAFT

Impact of thermodynamic surface properties on climate and climate change in a radiative-convective equilibrium version of ECHAM6

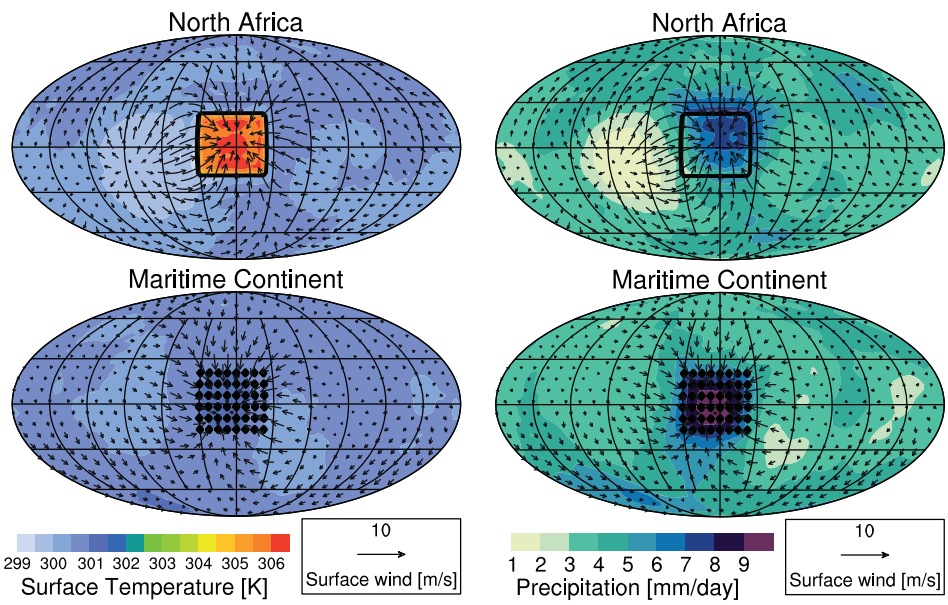

Tobias Becker

Hamburg 2014

Berichte zur Erdsystemforschung
Reports on Earth System Science

156
2014

Tobias Becker

Max-Planck-Institut für Meteorologie
Bundesstraße 53
20146 Hamburg

Master's Thesis

Dies ist eine überarbeitete Version der Masterarbeit (2013), die von der dem Bibliotheks- und Informationsservice zur Verfügung gestellten Version leicht abweicht.

Supervised by
Prof. Dr. Bjorn Stevens
and
Dr. Jürgen Bader
at the Max Planck Institute for Meteorology

Universität Hamburg
MIN-Fakultät, Fachbereich Geowissenschaften
Meteorologisches Institut

ISSN 1614-1199

Abstract

The comprehensive general circulation model ECHAM6 is used in a radiative-convective equilibrium (RCE) setup with the aim to enhance understanding of key processes concerning climate sensitivity and land-sea warming contrast. RCE is ensured by setting earth's angular velocity to zero, specifying homogeneous insolation and defining a thermodynamic mixed-layer ocean (MLO) with no internal horizontal fluxes. The most important thermodynamic properties of the MLO, the heat capacity and the evaporative flux, are reduced in order to get a "land-like" climate.

The ECHAM6-RCE climate resembles the tropical climate over the ocean in the realistic configuration of ECHAM6 remarkably well. This applies in particular to global mean temperature and precipitation as well as to the vertical atmospheric structure, including lapse rate, a bimodal relative humidity distribution and cloud and condensate profiles. Reducing the resolution from T63L47 to T31L47 does not change the main RCE climate features, though convection cluster size and time scale of vertical motions increase.

The heat capacity is reduced by decreasing the MLO depth. The diurnal surface temperature range (DTR) increases, resulting in a shift of maximum precipitation from night- to daytime at an MLO depth of 0.1 m. This has a strong impact on atmospheric processes. For example, there is more convection on the daily average. Climate sensitivity remains approximately constant for sufficiently large MLO depths, but decreases by about a third when DTR starts influencing the atmosphere because boundary layer clouds dissipate in the control experiment. Subsequently, climate sensitivity increases due to a positive feedback mechanism involving 700 hPa cloud formation which encourages low SSTs and which is more effective with a less opaque atmosphere.

The evaporative flux is restricted by introducing a new property, the evaporation resistance. An increase of evaporation resistance leads to a strong decrease of latent heat flux, which is primarily balanced by an increase of net longwave radiation from the surface and secondary by an increase of sensible heat flux, leading to "land-like" Bowen ratios. In response, surface temperatures increase until the atmosphere is so dry that longwave radiation is very efficient. With increasing evaporation resistance, a transition to a climate with only one convective cluster occurs. The self-aggregation leads to drier conditions in the subsidence regime. Concerning climate sensitivity, the experiments with this idealized land surface suggest that climate sensitivity is largest in areas where the negative lapse rate feedback is much smaller than over the ocean, but where the positive water vapor feedback is still large. Experiments in which a 0.1 m deep MLO is combined with increasing evaporation resistances confirm the previous results, especially concerning climate sensitivity, although surface temperatures increase even more and feedback factors change. Simulations with idealized continents show that surface inhomogeneities particularly influence the location where convection is triggered.

Kurzfassung

Das globale Zirkulationsmodell ECHAM6 wird an ein Strahlungskonvektionsgleichgewicht (RCE) mit dem Ziel angepasst, wichtige Prozesse bezüglich Klimasensitivität und Land-See-Erwärmungskontrast besser zu verstehen. RCE wird sichergestellt, indem die Erdrotation ausgeschaltet wird, überall die gleiche Sonneneinstrahlung eingestellt wird und als untere Randbedingung eine rein thermodynamische Deckschicht ohne interne Energieflüsse definiert wird. Die wichtigsten thermodynamischen Eigenschaften der Deckschicht, die Wärmekapazität und die Verdunstungsrate, werden reduziert, um ein "landähnliches" Klima zu erhalten.

Das ECHAM6-RCE Klima ähnelt dem tropischen Klima über dem Ozean in der realistischen Konfiguration von ECHAM6 in hohem Maß. Das gilt insbesondere für die globale Mitteltemperatur, den globalen Niederschlag sowie die vertikale Struktur der Atmosphäre, die durch ein ähnliches Temperaturprofil, eine bimodale Verteilung der relativen Feuchtigkeit und ähnliche Verteilungen von Wolkenwasser charakterisiert wird. Bei geringerer Auflösung (T31L47 statt T63L47) verändern sich die wichtigsten Klimamerkmale nicht, obgleich die Größe von konvektiven Zellen und die Zeitskala von Vertikalbewegungen zunimmt.

Die Wärmekapazität wird reduziert, indem die Deckschichttiefe verringert wird. Der Tagesgang der Deckschichttemperatur nimmt zu, wodurch sich bei einer Deckschichttiefe von 0,1 m der maximale Niederschlag von nachts zu tagsüber verschiebt. Das hat einen starken Einfluss auf atmosphärische Prozesse, zum Beispiel gibt es im Mittel mehr Konvektion. Die Klimasensitivität bleibt bei ausreichend großer Deckschichttiefe ungefähr konstant, nimmt aber um ungefähr ein Drittel ab, sobald der Tagesgang der Deckschichttemperatur atmosphärische Prozesse so sehr beeinflusst, dass sich Grenzschichtwolken im Kontrollexperiment auflösen. Danach nimmt die Klimasensitivität wieder zu, weil die positive Rückkopplung zwischen Wolken im 700 hPa Niveau und der Deckschichttemperatur in einer weniger langwellige Strahlung absorbierenden Atmosphäre stärker ist.

Die Verdunstungsrate wird verringert, indem eine neue Größe, der Verdunstungswiderstand, eingeführt wird. Ein Anstieg des Verdunstungswiderstands führt zu einer starken Abnahme des latenten Wärmeflusses, die in erster Linie durch einen Anstieg der langwelligen Ausstrahlung und zusätzlich durch einen Anstieg des sensiblen Wärmeflusses ausgeglichen wird, was zu "landähnlichen" Bowen-Verhältnissen führt. Die Deckschichttemperatur nimmt zu, bis die Atmosphäre so trocken ist, dass sehr effiziente langwellige Ausstrahlung möglich ist. Mit zunehmendem Verdunstungswiderstand kommt es zu einem Übergang zu einem Klima mit nur einer konvektiven Zelle, was zu trockeneren Bedingungen in den Absinkgebieten führt. Die Experimente mit dieser idealisierten Landoberfläche legen nahe, dass die Klimasensitivität in den Gebieten am größten ist, wo der negative Lapse Rate Feedback sehr viel geringer als über dem Ozean ist und gleichzeitig der positive Wasserdampffeedback noch groß ist. Experimente, in denen eine 0,1 m tiefe Deckschicht mit zunehmendem Verdunstungswiderstand kombiniert wird, bestätigen die vorherigen Ergebnisse insbesondere bezüglich der Klimasensitivität,

obwohl die Deckschichttemperatur stärker zunimmt und sich die Rückkopplungsfaktoren ändern. Simulationen mit idealisierten Kontinenten zeigen, dass Oberflächeninhomogenitäten insbesondere den Ort beeinflussen, an dem Konvektion ausgelöst wird.

Contents

1 Introduction

In the last decades, climate models became more and more complex as more and more processes were incorporated by the atmospheric general circulation models (GCMs). Such processes are, for example, a sea ice sub-model, coupling to the ocean, aerosols and dynamic vegetation. This increase in complexity extended the application range of GCMs, but did not reduce key uncertainties that emerged in early studies with less comprehensive models (Bony et al., 2013a). These key uncertainties include the response of climate models to a perturbation in greenhouse gases, arctic amplification of temperature changes and regional precipitation responses (Stevens and Bony, 2013). It is very difficult to reduce biases stemming from an inadequate representation of basic processes in a complex model because these biases introduce new biases which distort or amplify the basic bias. Because of that, it is helpful to use highly idealized models to improve the understanding of the basic processes and work through a hierarchy of models to connect robust behavior of the most comprehensive models to basic physical processes and laws (e.g. Held, 2005).

Within this hierarchy of models, radiative-convective equilibrium (RCE) is an important approach. In RCE, the radiative cooling of the atmosphere is balanced by the convective response, a transport of latent heat from the surface into the atmosphere. Physically, the convective response can also be interpreted as the tendency to stir the atmosphere until a uniform saturation equivalent potential temperature distribution is maintained. The simplifications of RCE are a good approximation of atmospheric properties everywhere on earth, but they are particularly appropriate for the tropical atmosphere, as vertical heat transfer through convection is the dominant process in the tropics. For comparison, the amount of energy exported from the tropics to the extratropics per unit time is only half as large as the energy released into the tropical atmosphere by condensation. The weak Coriolis force is the main reason for the dominance of convective processes over large-scale processes in the tropics. As a result, the average length scale of convective clusters is much smaller in the tropics than in the extratropics. This is one reason why a good parameterization of tropical convection is essential.

The assumption that radiative cooling and convective heating are the basic drivers of the vertical temperature structure has a long history in climate sciences. Already in 1862, Lord Kelvin introduced the concept of RCE by adding convection to radiation as the basic driver of the temperature lapse rate in the troposphere (Chandrasekhar, 1957). One century later,

Manabe and Strickler (1964) and Manabe and Wetherald (1967) studied the relationship between radiative cooling and convective heating in detail with a single-column model. Their realization that the atmosphere, to a sensible degree of approximation, is well described by RCE, revolutionized the understanding of atmospheric processes. Since then RCE has been used in many climate studies. A review of RCE in single-column models is given by Ramanathan and Coakley (1978). Tompkins and Craig (1998a) introduced the concept of RCE in a new environment, in three-dimensional cloud-resolving models with an explicit representation of the convective scale. The concept of RCE has been surprisingly rarely used in GCM studies, as far as known only by Held et al. (2007), who used the full GCM physics package in a cartesian geometry with fixed sea-surface temperatures (SSTs), before Popke et al. (2013) picked up this idea in a slightly different approach. They coupled the ECHAM6 model of the Max Planck Institute for Meteorology to an aquaplanet with a mixed-layer ocean (MLO) and homogeneous boundary conditions, which include spatially uniform solar insolation and inhibited rotation of the planet. Nonetheless, inhomogeneous SSTs, clouds and water-vapor concentrations were allowed to develop consistently with the circulation in the model. Compared to the first RCE studies with single-column models (Ramanathan and Coakley, 1978), the great advantage is that atmospheric profiles of clouds and water vapor do not have to be prescribed. Hence, column-to-column interaction of physical processes is enabled and feedback analysis is possible. The study presented in this thesis builds on the results of Popke et al. (2013), so the same three-dimensional GCM setup is used.

It may seem like a step backwards to examine RCE in a hydrostatic model at GCM resolution while other studies investigate RCE with a cloud-resolving model (CRM). Nevertheless, idealized models using a GCM's resolution and physics package are already themselves objects worthy of study, especially if that GCM is used for climate change predictions which are the basis for society's reaction to global warming. Furthermore, RCE experiments are also methodologically promising, as they can fill a gap in model hierarchy between high resolution models like large eddy simulation (LES) models on the one hand and GCMs on the other hand. RCE is well suited to bridge this gap because processes in an RCE environment have the advantage that they are approximately scale independent. In addition, RCE experiments with a fully fledged GCM are especially well suited for the identification and understanding of basic processes because they can be compared with simple models of climate change on the one hand and comprehensive GCMs with realistic boundary conditions on the other hand. Good examples are convective organization and convective precipitation, which can be analyzed in an RCE environment easily without the interaction with large scale dynamics. Hence, RCE experiments with fully fledged GCMs are an important element in the already mentioned hierarchy of models which connect robust behavior of complex systems to basic physical principles.

As a counterpart to the RCE setup of Popke et al. (2013) with the underlying mixed-layer ocean, the ambition in this thesis is the transition to a "land-like" climate by changing some thermodynamic surface properties. Apart from the fact that this transition helps investigate and understand climate dynamics on the RCE planet, there is hope that this study can contribute to the understanding of land-sea warming contrast in climate change. As humans live on land and most of our food is produced on land, it is crucial for us to know by which extent climate change is amplified over land. However, this question is hard to answer as various processes are involved. Besides, it is important to note that equilibrium simulations show different climate sensitivities than transient simulations. If greenhouse gas concentrations are increased, land will always adapt faster due to the smaller heat capacity. Nonetheless, a greater land-sea contrast in a warmer equilibrium state is less obvious. Joshi et al. (2008) showed with idealized GCM experiments that the land-sea warming contrast can be associated with local feedbacks and the hydrological cycle over land. Their main argument is that atmospheric profiles over land are less often saturated than over sea, which means that the time-averaged lapse rate over land is closer to the dry adiabat, and so decreases less if temperature increases. Given uniform warming aloft, this implies that the land surface warms more than the ocean. In this thesis, the change of lapse rate feedback over idealized land will be investigated together with other key processes that are different over land and ocean and that may lead to different climate sensitivities. So besides the question whether the climate resulting after some changes of thermodynamic surface properties is really "land-like", another main question in this thesis is how the changes of climate and climate sensitivity can be explained.

The remainder of this thesis is organized as follows: In Section 2, the model configuration and methodology of this study are described. In Section 3, the RCE climate and its phenomenology are introduced and resolution dependence is investigated. In Section 4, the transition to a "land-like" planet is analyzed. This is divided in a subsection concentrating on the impact of MLO depth, a subsection focusing on the reduction of latent heat fluxes by introducing an evaporation resistance that makes evaporation from the ocean more difficult and a subsection examining the combination of these two effects. In Section 5, the interaction of the ocean with idealized continents with reduced MLO depth and increased evaporation resistance is investigated.

2 Methods

The experiments in the radiative-convective equilibrium (RCE) setup are performed with ECHAM6, which is an atmospheric general circulation model. ECHAM6 is the atmospheric component of the fully comprehensive Earth System Model MPI-ESM of the Max Planck Institute for Meteorology (Stevens et al., 2013). The present version of the MPI-ESM is described by Giorgetta et al. (2013). ECHAM branched from an early release of the ECMWF (European Center for Medium Range Weather Forecasts) model (Roeckner et al., 1989). It is a hydrostatic model with physics calculated on a latitude-longitude grid, while dynamics are computed in spectral space. ECHAM's physics package is also implemented in ICON, which is the new icosahedral non-hydrostatic GCM on a triangular grid which is currently developed by the Max Planck Institute for Meteorology and the German Weather Service (DWD). In the last 25 years, ECHAM has been improved continuously, with 6 main releases. In all releases, the dynamical core is based on the primitive equations in the vorticity and divergence form, with temperature and surface pressure being the thermodynamic coordinates (Stevens et al., 2013). In the default suite of the actual version, ECHAM6, subgrid-scale cloudiness is parameterized with a critical relative humidity function (Sundqvist et al., 1989), cloud condensate and cloud ice are calculated prognostically (Lohmann and Roeckner, 1996), and shallow as well as mid level convection are parameterized with a mass-flux framework developed by Tiedtke (1989), while the parametrization of deep convection incorporates changes proposed by Nordeng (1994). Radiative transfer is based on the Rapid Radiation Suite of models as optimized for the general circulation modeling studies (Iacono et al., 2008), which is a two-stream radiation scheme. A more detailed description of the parameterized physical processes is presented by Stevens et al. (2013).

2.1 The RCE version of ECHAM

The idea to combine RCE experiments with a GCM is relatively new. Traditionally, RCE experiments have been conducted with single column models. Ramanathan and Coakley (1978) give an overview about possible setups for single column RCE studies concerning trace gases, aerosols and cloud amount. They state that these models give valuable insights into problems of climate theory and climate change, but have limited applicability to the real climate system. This is mainly because some atmospheric properties like the cloud amount

need to prescribed. As a consequence, the principle weakness of these models is the inability to simulate the cloud feedback. Another issue is the humidity profile, which also needs to be prescribed. Fixed relative humidity is most commonly chosen, following Manabe and Wetherald (1967). If a three-dimensional GCM is used instead of the single column model, a circulation with subsidence and upsidence regions develops and the atmospheric properties are calculated by the model, so fewer assumptions are required. Besides, compared to a single column model, a GCM has the advantage that multiple equilibria are not possible. In RCE, homogeneous boundary conditions are necessary to avoid differences in the mean state of the vertical columns of the GCM. If this condition is fulfilled, radiation and convection are the only processes that determine the vertical thermal structure (Ramanathan and Coakley, 1978). Homogeneous boundary conditions are achieved by choosing an aquaplanet with a mixed layer ocean as surface boundary condition, removing the latitudinal insolation gradient by specifying the same diurnal cycle of solar insolation for the whole planet, setting the angular velocity of the planet to zero and defining horizontally uniform trace gas and aerosol concentrations. An overview is given in Table 1.

	ECHAM6	RCE setup
surface boundary	land-ocean mask	mixed layer ocean
Coriolis force	yes	no
solar constant	$1361\,\mathrm{W\,m^{-2}}$	$1069\,\mathrm{W\,m^{-2}}$
mean insolation	$340.3\,\mathrm{W\,m^{-2}}$	$340.3\,\mathrm{W\,m^{-2}}$
trace gas concentrations	heterogeneous	homogeneous
aerosol concentrations	heterogeneous	homogeneous

Table 1: Overview about the main changes in the RCE setup.

In order to reduce complexity and ensure homogeneity, a slab ocean with fixed heat capacity defines the lower model boundary. Compared to the RCE setup with prescribed SSTs (e.g. Held et al., 2007), this has the advantage that SSTs can respond to an atmospheric forcing. The ocean heat transport is switched off. Consequently, the ocean can only warm thermodynamically due to surface energy imbalances. The pace of adaptation depends on the heat capacity of the ocean, which is proportional to the MLO depth as the model assumes that temperatures are constant with depth in the mixed layer and that the mixed layer is perfectly isolated from the deep ocean by the thermocline. In the control RCE setup, the MLO depth is 50 m. Homogeneous boundary conditions are ensured by removing the ocean surface albedo dependence on zenith angle and setting it to a constant value of 0.07 instead. With this setup, the time-weighted average temperatures are everywhere the same, although they can adapt to changes in the atmosphere. This is desirable since it allows the formation and propagation of large-scale circulation systems. Consequently, the MLO setup is chosen. For comparison, an experiment with prescribed SSTs and with constant solar insolation was conducted.

On earth, radiative-convective equilibrium is most appropriate for the tropics on a regional scale because in the tropics, both Coriolis force and latitudinal temperature gradients are small. Furthermore, tropical convection is not triggered by frontal systems, but by surface heating and converging air masses. Consequently, in the RCE setup, insolation and ozone concentrations are set to values that are reasonable for the tropics, so that a comparison of RCE climate with the climate in the tropics is possible. In the RCE setup, the diurnal cycle of solar insolation is defined as

$$F(t) = I_0 \mu_0(t), \tag{1}$$

where I_0 is the solar constant and μ_0 is the cosine of the solar zenith angle. The solar zenith angle is set to be zero at noon, so every grid point experiences perpendicular insolation as well as the other phases of the equatorial diurnal cycle at the same time. If the solar constant were the same as on earth, every grid point would receive as much insolation as if it were located at the equator. Hence, the global mean insolation would increase. In compliance with the assumption that the amount of energy transported from the tropics to the extratropics corresponds to the surplus in the tropical energy balance, it is more promising to keep the diurnally averaged global mean insolation at $340.3\,\mathrm{W\,m^{-2}}$, which corresponds to the global mean insolation on earth. For this purpose, the solar constant is decreased by a factor of $\frac{\pi}{4}$ from $1361\,\mathrm{W\,m^{-2}}$ to $1069\,\mathrm{W\,m^{-2}}$. The solar irradiance in ECHAM6 is resolved in 14 spectral bands. In order to reduce the solar constant to $1069\,\mathrm{W\,m^{-2}}$, the irradiance in every band is rescaled with the factor $\frac{\pi}{4}$.

In the default ECHAM6 setup, the parametrization of planetary boundary layer height is defined as the minimum of the convective and dynamic boundary layer height. The dynamic boundary layer height is the height where the wind direction changes, which depends on the Coriolis parameter. In contrary, the convective boundary layer is the layer that is directly influenced by convection initiated at the surface, which is independent of the Coriolis parameter. As earth's angular velocity is set to zero in the RCE setup, the boundary layer height has to be redefined to be the convective boundary layer height. This is consistent with the boundary layer behavior in the tropics.

Horizontally uniform trace gas and aerosol concentrations are achieved by prescribing equatorial preindustrial time-mean zonal-mean ozone profiles for every grid point in the RCE model according to Popke et al. (2013) and by setting aerosol concentrations to zero. Another necessary adaptation is an increase of the atmospheric mass in order to keep the mean sea-level pressure (SLP) at 1013.25 hPa. The SLP would decrease otherwise, because there are no mountains in the aquaplanet setup. It is also important to note that the RCE model version was not tuned, so the same tuning constants are used as in the default ECHAM6 model setup (Mauritsen et al., 2012).

Nevertheless, there is one aspect in which the boundary conditions are not homogeneous. In ECHAM6, a Gaussian grid is used, so the grid size decreases towards the poles. However,

this grid inhomogeneity does not lead to areas where convection is enhanced or favored, as discussed in Section 3.

2.2 Experiments

ECHAM-6.1.05 is used for the RCE experiments presented here. This version does not differ much from ECHAM-6.0.13, which is the release that Popke et al. (2013) used for their RCE simulations. In order to achieve the highest degree of comparability, the boundary conditions of the RCE experiments presented here are identical to the boundary conditions set by Popke et al. (2013). Nevertheless, there are some differences due to the newer model version. Besides, Popke et al. (2013) employed a time step of 450 s, while the standard time step of 900 s is employed here. In both model setups, the output is generated in 6-hourly intervals.

In all experiments, climate change is studied by quadrupling CO_2 concentrations from the preindustrial concentration of 278 ppmv to 1112 ppmv. Only in one case the CO_2 concentration is doubled to 556 ppmv instead of quadrupled because the 4xCO_2 experiment did not reach a stable equilibrium. The volume mixing ratios of other trace gases were held constant at the preindustrial level of 650 ppbv for methane and 270 ppbv for nitrous oxide. The contribution of a single process in response to a forcing, e.g. in response to a radiation imbalance, can be quantified with a feedback parameter λ (Stocker, 2011). The influence of the water vapor, lapse rate and cloud feedback on climate sensitivity is diagnosed using the accurate but computational expensive partial radiation perturbation (PRP) method, which is described in detail by Klocke et al. (2013) and has been successfully implemented in ECHAM6 by Mauritsen et al. (2013). The PRP module is relatively fast, since it works in parallelization on all processors. The idea to calculate radiative transfer off-line was first introduced by Wetherald and Manabe (1988). The basic principle is to substitute the radiation relevant variables from the perturbed simulation separately into the control simulation, so the feedback factor

$$\lambda_x = \frac{\Delta_x R}{\Delta x} \frac{\Delta x}{\Delta T_\mathrm{s}} \tag{2}$$

can be calculated separately for any three-dimensional, time-resolved quantity x (Klocke et al., 2013). Δx and ΔT_s represent the difference between control and perturbed experiment, with ΔT_s standing for the surface temperature change. $\Delta_x R/\Delta x$ is from off-line radiation calculations, with R representing the top of atmosphere (TOA) net radiation flux. Hence, the advantage of this method is that the partial derivatives can be calculated directly. This leads to very small errors in comparison to other methods, for example using the cloud radiative effect (CRE) for estimating the cloud feedback. Soden et al. (2004) show that using the CRE leads to a systematic error because non-cloud feedbacks are overestimated due to masking effects, resulting in a systematic underestimate of cloud feedback. When using the PRP

method, no masking effects can occur if the perturbed and control simulations are uncorrelated. Simulations are uncorrelated in the RCE experiments because there are no seasonal, orographic or latitudinal effects which might lead to a correlation. However, as radiation can be perturbed unintendedly when decorrelating variables, the PRP method is applied twice. Once forward, by substituting a variable from the perturbed into the control climate, and once backward, by substituting a variable from the control into the perturbed climate. The final radiative perturbation is then estimated with the average of forward and backward perturbation (Klocke et al., 2013). The only assumptions remaining are that interactions between feedbacks are small and that the difference between perturbed and control simulation is small enough to allow for the discrete approximation of the derivative by the differentiation. In this thesis, when the PRP method is used, all relevant instantaneous fields are written out every 22 hours in the control simulation and are inserted as described above in the experiments with doubled or quadrupled CO_2 concentrations.

Five different types of ECHAM6 experiment series in the RCE setup are presented (Table 2 and Table 3). In the first sequence of experiments, the resolution dependence and the influence of resolution dependent parameterizations is examined (Section 3). In the subsequent experiments, the influence of surface properties on climate and climate change is analyzed, concentrating on thermodynamic surface properties which are fundamentally different over ocean and land. As a first step, the influence of MLO depth with and without a diurnal cycle of solar insolation is investigated (Section 4.1). As a second step, the moisture fluxes at the surface of the MLO are reduced by introducing an artificial evaporation resistance (Section 4.2). As a last step towards a "land-like" planet, the combined effect of decreased MLO depth and increased evaporation resistance is examined in Section 4.3. Besides, in two final experiments the influence of surface inhomogeneities is analyzed (Section 5). Therefore, the MLO depth is reduced and evaporation resistance is increased only in certain areas. In the first experiment, this area has approximately the shape of North Africa and in the second experiment there are grid point islands which are reminiscent of the Maritime Continent.

In ECHAM6, there are several spectral model resolutions available. In the horizontal, the most common modes ordered from high to low resolution are T255, T127, T63 and T31. In this thesis, T63, which refers to a longitude-latitude grid of 192 x 96, is compared with T31, which corresponds to a 96 x 48 grid. In the vertical, the most common resolutions are L95, L47 and L31. The L47 grid is identical to the L31 grid up to 100 hPa and the L95 grid is identical to L31 and L47 for the lowermost 12 levels up to 611 hPa. Above these levels, the resolution is enhanced. The top level of L31 is 10 hPa, whereas L47 and L95 resolve the atmosphere up to 0.01 hPa (Stevens et al., 2013). In the experiments regarding resolution dependence, the horizontal resolution is decreased from T63 to T31, while the vertical resolution is kept constant at L47. In addition, some tuning parameters that depend on the model resolution are kept constant at the T63 values in order to improve comparability.

Simulation	Simulation length [years]	Equilibrium length [years]	PRP module [years]
Resolution			
T63, ECHAM 6.0.13	60	30	-
T63	30	20	-
T31, zinhomi like T31	50	30	-
T31, zinhomi like T63	70	60	10
insolation + SST const.	1	1	-
MLO depth - without diurnal cycle			
50 m, 4xCO_2	30	20	10
1 m, 1xCO_2	30	20	10
1 m, 4xCO_2	30	20	10
0.1 m, 1xCO_2	30	20	10
0.1 m, 4xCO_2	30	20	10
0.02 m, 1xCO_2	30	20	10
0.02 m, 4xCO_2	30	20	10
MLO depth - with diurnal cycle			
50 m, 1xCO_2	70	60	10
50 m, 4xCO_2	60	50	10
5 m, 1xCO_2	30	20	10
5 m, 4xCO_2	30	20	10
1 m, 1xCO_2	60	50	10
1 m, 4xCO_2	60	50	10
0.1 m, 1xCO_2	30	20	20
0.1 m, 4xCO_2	30	20	20
0.05 m, 1xCO_2	30	20	10
0.05 m, 4xCO_2	30	20	10
0.02 m, 1xCO_2	60	50	10
0.02 m, 4xCO_2	60	50	10

Table 2: Overview of simulations, Part I. The years in which the PRP module is used are part of the years in equilibrium. "T63, ECHAM 6.0.13" is a run with the same RCE settings, but an older model version by Popke et al. (2013).

The affected resolution-dependent tuning parameters are the convective cloud mass-flux above the level of non-buoyancy (cmfctop), the conversion rate to rain in convective clouds (cprcon) as well as the homogeneity of liquid clouds (zinhomi, zinhoml1 and zinhoml2), as described by Mauritsen et al. (2012). In the following, zinhomi, zinhoml1 and zinhoml2 will be consolidated as zinhomi.

For the experiments with different MLO depths, essentially no changes are necessary in ECHAM6, only the parameter defining the MLO depth, dmixsea, needs to be converted into an individually adjustable constant. The implementation of an additional resistor that reduces

Simulation	Simulation length [years]	Equilibrium length [years]	PRP module [years]
Evaporation resistance with 50 m MLO depth			
rsoil=1, 1xCO_2	40	30	10
rsoil=1, 4xCO_2	40	30	10
rsoil=3, 1xCO_2	40	30	10
rsoil=3, 4xCO_2	40	30	10
rsoil=7, 1xCO_2	40	30	10
rsoil=7, 4xCO_2	40	20	10
rsoil=15, 1xCO_2	40	30	10
rsoil=15, 4xCO_2	40	20	10
rsoil=31, 1xCO_2	40	30	10
rsoil=31, 4xCO_2	40	20	10
rsoil=63, 1xCO_2	40	30	10
rsoil=63, 4xCO_2	40	20	10
Evaporation resistance with 0.1 m MLO depth			
rsoil=1, 1xCO_2	30	20	20
rsoil=1, 4xCO_2	30	20	20
rsoil=3, 1xCO_2	30	20	20
rsoil=3, 4xCO_2	30	20	20
rsoil=7, 1xCO_2	30	20	20
rsoil=7, 4xCO_2	30	20	20
rsoil=15, 1xCO_2	30	20	20
rsoil=15, 4xCO_2	30	20	20
rsoil=31, 1xCO_2	30	20	20
rsoil=63, 1xCO_2	30	20	20
rsoil=63, 2xCO_2	30	20	20
Idealized continents			
North Africa	30	20	-
Maritime Continent	30	20	-

Table 3: Overview of simulations, Part II. The years in which the PRP module is used are part of the years in equilibrium.

moisture fluxes at the surface is more complex. In ECHAM6, the turbulent flux of a variable χ at the surface is obtained from the bulk transfer relation

$$\left(\overline{\omega'\chi'}\right)_{\mathrm{s}} = -C_\chi \left|\overrightarrow{V_{\mathrm{l}}}\right| (\chi_{\mathrm{l}} - \chi_{\mathrm{s}}), \tag{3}$$

where C_χ is the transfer coefficient, $\overrightarrow{V_{\mathrm{l}}}$ is the horizontal wind vector and the subscripts l and s refer to values at the lowest model level and at the surface (Roeckner et al., 2003). The parameter zcfhw in ECHAM6 is defined like the turbulent flux in Equation 3, except that the variable χ is specified to be heat, that the vertical heat gradient is not included and that it is multiplied by some factors:

$$\text{zcfhw} = \frac{\text{cvdifts} \cdot \Delta t \cdot g \cdot p_\text{l} \cdot \left|\overrightarrow{V_\text{l}}\right| \cdot C_\text{h}}{R \cdot T_\text{l}}. \tag{4}$$

Here cvdifts is the time step weighting, Δt is the forecast time step, g is gravitational acceleration, p_l and T_l are pressure and temperature at the lowest model level, R is the specific gas constant and C_h is the heat transfer coefficient, which depends on the bulk Richardson number, the height of the lowest model level and the roughness length for momentum and heat. Among others, zcfhw is used to calculate the moisture flux zqhflw:

$$\text{zqhflw} = \frac{1}{\text{cvdifts} \cdot \Delta t \cdot g} \cdot \text{zcfhw} \cdot (q_\text{l} - q_\text{s}). \tag{5}$$

In all the cases where zcfhw affects moisture variables like the moisture flux, it is reduced by adding a second resistor in series:

$$\text{zcfhw}^* = \frac{1}{\frac{1}{\text{zcfhw}} + \frac{\text{rsoil}}{\overline{\text{zcfhw}}}}. \tag{6}$$

The parameter rsoil can be interpreted as the additional resistor that increases evaporation resistance, which makes it comparable to evaporation from soil or plants. As zcfhw has typical values of about 200, $\overline{\text{zcfhw}} = 200$ is assumed. This means that zcfhw* is approximately halved for rsoil $= 1$. If rsoil $= 0$, zcfhw* is equal to zcfhw, so this is the standard ECHAM setup for moisture fluxes from the ocean.

In order to be able to do some experiments with idealized continents, the MLO depth and the evaporation resistance need to be changed in specific areas. Therefore, a land-sea mask is defined and read into ECHAM. The evaporation resistance rsoil and the MLO depth dmixsea are then defined on arrays and altered by the land-sea mask.

Apart from the changes described above, no further modifications of the standard ECHAM6 setup are necessary for the RCE experiments conducted in this thesis. Thus, the complete model physics is sustained.

A simpler analysis of the model results is made possible by introducing a mass-weighted average of the vertical velocity in the troposphere between 925 and 200 hPa. The mass is calculated from the layer height and the air density. This definition conforms with the definition of the mass-weighted vertical velocity by Popke et al. (2013). The introduction of the mass-weighted vertical velocity has the advantage that a sampling in subsidence and upsidence regimes is both easy and accurate.

3 Phenomenology of ECHAM-RCE climate and resolution dependence

Before analyzing climate and climate change in a "land-like" RCE setup, the RCE climate in the control aquaplanet setup needs to be understood. This ambition can be combined with the analysis of the influence of the model resolution on the result. If the model resolution is enhanced, some processes that have been subgrid-scale beforehand can be directly simulated afterward, so the number of processes that have to be parameterized is reduced. Hence, the model's physics change and some tuning parameters are adapted. This adaptation partly fails in the RCE setup because RCE climate differs significantly from the climate the resolution dependent parameters were tuned to. In order to enhance comparability, it is therefore advantageous not to change the tuning parameters for different resolutions in the RCE setup. The affected tuning parameters are introduced in Section 2.2. The impact of the adaptation of the tuning parameter zinhomi (homogeneity of liquid clouds) is examined in the experiment which is named "T31, zinhomi like T31". The control experiment has constant tuning parameters and is named "T31, zinhomi like T63". In this chapter, along with the resolution dependence, the model version dependence is explored. As this thesis builds on the results of Popke et al. (2013), a high degree of alignment between RCE climate in ECHAM 6.0.13 and 6.1.05 is desirable.

Figure 1 shows the dependence of monthly mean SSTs in equilibrium on resolution, model version and the tuning parameter zinhomi. The global mean equilibrium SST differences are approximately within a range of 1 K as Table 4 illustrates. This offset is reduced to 0.4 K if the tuning parameters cmfctop, cprcon and zinhomi are kept constant. As the histograms of monthly averaged SSTs strongly overlap (Figure 1), it can be concluded that the offset of 0.4 K is rather small. The equilibrium global mean SSTs of the T31 run with constant tuning parameters ("T31, zinhomi like T63") and the T63 run in the older model version ("T63, ECHAM 6.0.13"), which is a result of Popke et al. (2013), are closest to each other. This is counterintuitive because not only the resolution, but also the model version has changed. The high level of agreement is probably due to compensating errors because the SST offset is larger both in the experiments with changed model version (0.4 K offset between "T63" and "T63, ECHAM 6.0.13") and in the experiments with changed resolution (0.4 K offset between "T63" and "T31, zinhomi like T63"). The main reason for the equilibrium SST offset of the experiments with different model versions is not the model version itself, as the model versions

are very similar, but the different time step. The time step influences the equilibrium climate state as some parameterizations depend on the time step. For example, in ECHAM 6.0.13, an increase of the time step from 450 s to 600 s leads to a decrease of global mean SSTs by approximately 0.4 K.

Table 4 further shows that the global mean precipitation correlates with the global mean SST. Precipitation and SST are connected because the Clausius-Clapeyron (CC) equation

$$\frac{d \ln e_{\mathrm{s}}}{dT} = \frac{L_{\mathrm{v}}}{R_{\mathrm{v}} T^2} \tag{7}$$

states, that the saturation specific humidity e_s depends on the temperature T only because the latent heat of vaporization L_{v} is approximately constant as well as the water vapor gas constant R_{v}. From the CC equation follows that the saturation vapor pressure increases by approximately 7 % K^{-1} at common near surface temperatures (Held and Soden, 2006). Climate models tend to maintain a fixed relative tropospheric humidity while warming (Manabe and Wetherald, 1967), so the humidity content of the atmosphere should also raise approximately by 7 % K^{-1}. Nevertheless, Held and Soden (2006) have shown that precipitation increases roughly by 2 % K^{-1} on global scales. In Table 4, precipitation increases approximately by 5 % K^{-1} in the T31 experiment with an adjusted tuning parameter zinhomi, which is more than expected by Held and Soden (2006), but which is consistent with the sensitivity of the global hydrological cycle of 4 % K^{-1} that Lindzen et al. (1982) found in their one-dimensional radiative-convective model. Overall, the precipitation changes agree well with the SST changes.

	SST [K]	σ_{SST} [K]	$\sigma_{<\mathrm{SST}>}$ [K]	ξ_{SST}	P [mm/d]
T31, zinhomi like T31	301.0	0.91	0.13	-0.13	4.30
T31, zinhomi like T63	300.1	0.86	0.13	-0.20	4.09
T63	299.7	0.78	0.08	-0.52	4.01
T63, ECHAM 6.0.13	300.1	0.7	0.07	-0.36	4.1

Table 4: Statistical moments of SST and global mean precipitation for different model resolutions with or without constant tuning parameters. T31, zinhomi like T31 represents the experiment with the adapted homogeneity of liquid clouds parameter (zinhomi) and T31, zinhomi like T63 represents the experiment with the constant tuning parameters zinhomi, cprcon and cmfctop. T63, ECHAM 6.0.13 is a run with the same RCE setup, but an older model version by Popke et al. (2013). σ_{SST} and ξ_{SST} denote the spatial standard deviation and skewness of the monthly mean SST fields averaged over time, while $\sigma_{<\mathrm{SST}>}$ denotes the temporal standard deviation of the monthly global mean SST. P stands for the global mean precipitation.

Figure 1 illustrates that the distribution of monthly averaged SSTs is in all experiments negatively skewed. A negative skewness is confirmed in Table 4 with values between -0.52 and -0.13. Consequently, there must be at least one feedback mechanism which leads to disproportionately low SSTs. The negatively skewed distributions are further analyzed in

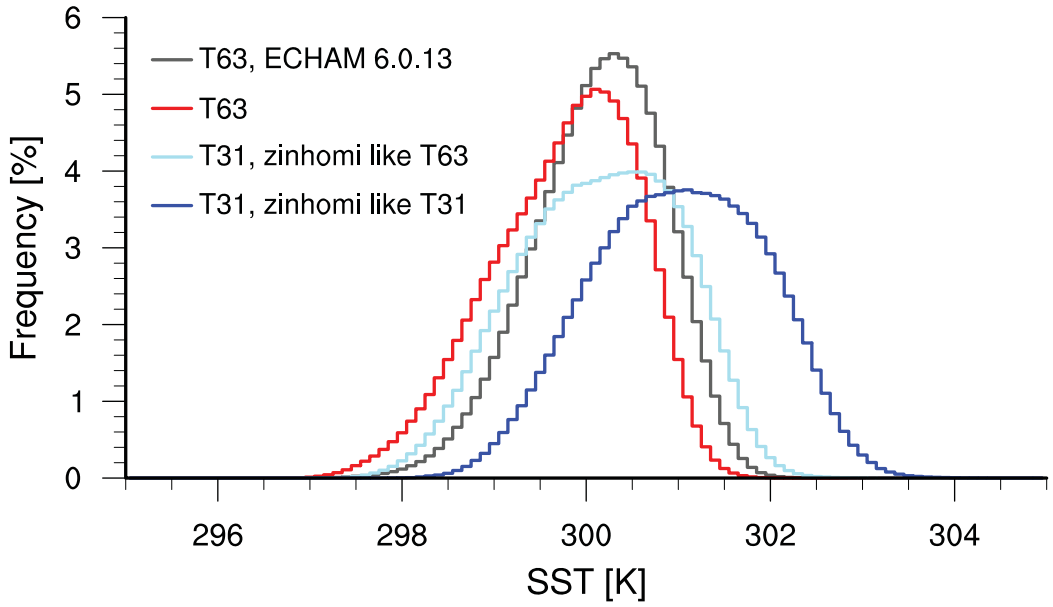

Figure 1: Histogram of monthly averaged SSTs at all grid points in equilibrium for different model versions and different model resolutions. Each grid point is weighted by its area. The bin size is 0.1 K. T63, ECHAM 6.0.13 is an RCE experiment with the same setup, but an older model version by Popke et al. (2013).

Section 4.1. The spatial standard deviations of the monthly mean SST fields averaged over time lie between 0.7 and 0.9 K. Hence, the spatial standard deviations are larger than the temporal standard deviations of global mean SST, which range between 0.07 and 0.13 K (Table 4). On this account, the spatial SST fluctuations dominate temporal fluctuations and could be an important trigger of precipitation.

Table 5 provides an overview of the correlation of SST and precipitation as well as the correlation of one of these variables with the trend of the other variable. Weekly data are used as input, but 6 hourly or monthly data do not give fundamentally different results. The correlation of SST and precipitation is in all experiments positive with values between 0.46 and 0.29. This means that the probability of precipitation is enhanced over regions of high SST, but it does not provide any information concerning cause and effect. The cause-and-effect relationship is investigated with the correlations of tendency and deviation. The negative correlation of SST tendency and precipitation with values between -0.28 and -0.33 indicates that temperatures tend to decrease in areas with precipitation. The correlation of precipitation tendency and SST is slightly positive. A positive correlation implies that precipitation tends to increase if the ocean is warm. However, such a small positive correlation is not statistically significant, although the sample is quite large. Nevertheless, it can be concluded that precipitation clusters form in RCE climate in regions of high SSTs because the atmosphere is least stratified there. This encourages upward motion and convergence of

the surface wind field. The increase of surface wind speed enhances evaporation in a positive feedback mechanism. On the other hand, the formation of deep clouds cools the surface. This is a reason for the movement of the cloud clusters.

Correlation	SST | P	P | SST_{t+1} - SST_t	SST | P_{t+1} - P_t
T31, zinhomi like T31	0.46	-0.28	0.04
T31, zinhomi like T63	0.42	-0.30	0.04
T63	0.29	-0.33	0.04

Table 5: Correlation of SST and precipitation (P) with weekly data. In addition, the correlation of one of the variables with the tendency of the other variable is presented, t denoting the current time step and t+1 denoting the time step one week later.

The discovered net cooling effect of the cloud clusters is no necessity because there are two competitive radiative effects. If there are clouds, on the one hand less shortwave radiation penetrates to the surface, but on the other hand, clouds contribute to the greenhouse effect because outgoing longwave radiation is absorbed by the clouds. Which of these processes is dominant depends mainly on cloud height. High clouds warm the surface because they reduce outgoing longwave radiation efficiently. The temperature difference compared to surface temperatures is large, so the amount of emitted thermal radiation differs significantly. Low clouds cool the surface because their temperature is not very different from the SST. Thus, the impact on thermal radiation is small. Besides, the optical thickness of low clouds is in general high, so the penetration of solar radiation to the surface is reduced effectively.

The energy fluxes at the surface and at TOA are presented in Table 6. In equilibrium, the global mean net flux at the surface

$$\mathrm{SFC_{net}} = \mathrm{SW_{SFC,net}} + \mathrm{LW_{SFC,net}} + \mathrm{SH} + \mathrm{LH} \tag{8}$$

and the global mean net flux at TOA

$$\mathrm{TOA_{net}} = \mathrm{SW_{TOA,net}} + \mathrm{LW_{TOA,net}} \tag{9}$$

should both be zero. SW and LW denote the net shortwave and longwave radiation at TOA or at the surface, respectively, while SH and LH stand for sensible and latent heat fluxes. However, in ECHAM-6.1.05, a known issue is an energy leakage of the atmosphere

$$\mathrm{ATM_{net}} = \mathrm{TOA_{net}} - \mathrm{SFC_{net}} + S, \tag{10}$$

which depends on the global mean SST (Popke, 2012). S denotes the latent heat flux of fusion, which is neglectable in the RCE setup. As a result of the energy leakage in the atmosphere, there are nonzero equilibrium net radiation fluxes at TOA with values between -0.2 and -0.4 $\mathrm{W\,m^{-2}}$, while the global mean net flux at the surface is approximately zero.

	$SW_{TOA,net}$	$LW_{TOA,net}$	$SW_{SFC,net}$	$LW_{SFC,net}$	SH	LH
T31, zinhomi like T31	-272.1	272.4	-197.3	59.9	12.9	124.4
T31, zinhomi like T63	-268.2	268.4	-194.1	62.2	13.6	118.3
T63	-271.5	271.9	-199.6	69.7	13.9	116.0
T63, ECHAM 6.0.13	-272.5	272.9	-200.5	69.7	13.8	117.0

Table 6: Energy fluxes at the surface and at the top of atmosphere (TOA) for different model resolutions with or without constant tuning parameters. T63, ECHAM 6.0.13 is an RCE experiment with an older model version by Popke et al. (2013). $SW_{TOA,net}$ and $LW_{TOA,net}$ denominate the net shortwave and longwave fluxes at the TOA, while $SW_{SFC,net}$ and $LW_{SFC,net}$ denote the net shortwave and longwave fluxes at the surface and SH and LH stand for sensible and latent heat fluxes. Upward fluxes are defined to be positive and units are $W\,m^{-2}$.

Figure 2 gives an overview about the vertical atmospheric distribution of temperature, relative humidity, cloud fraction, cloud liquid water and cloud ice. The distribution of relative humidity is bimodal with a liquid cloud layer near the surface and an ice cloud layer in the upper troposphere with a dry middle troposphere in between. In the T31 experiment with an adjusted tuning parameter zinhomi, the cloud fraction is higher at the tropopause. As a consequence, the temperature is higher in the troposphere in this experiment. In the T31 experiment with unchanged tuning parameters, the cloud fraction is not only higher at the top, but throughout the whole upper troposphere. This leads to compensating effects and to a surface temperature which is very similar to the T63 experiments. The vertical profiles of the T63 experiments with the different model versions are nearly indistinguishable. All in all, the structural accordance of the vertical atmospheric profiles of the T31 and T63 experiments is very good.

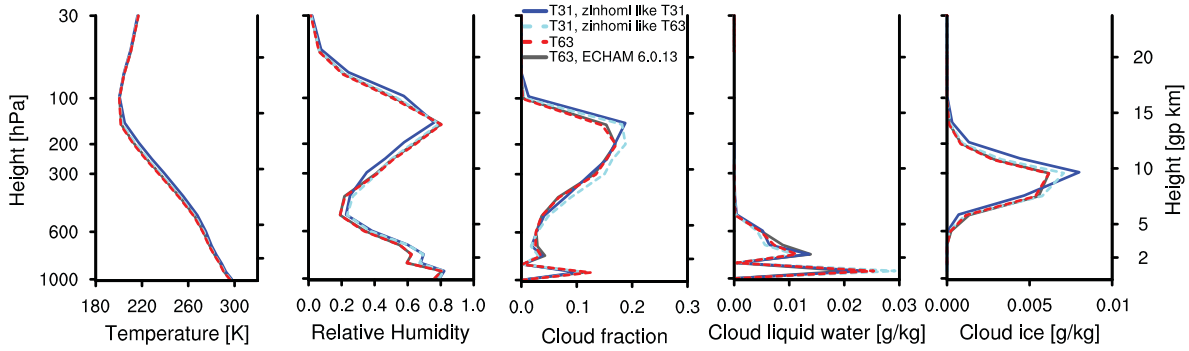

Figure 2: Vertical equilibrium profiles of atmospheric properties for different model resolutions with or without constant tuning parameters. T63, ECHAM 6.0.13 is a run with the same settings, but an older model version by Popke et al. (2013).

In Figure 3, the control RCE climate (T31, zinhomi like T63) is compared to the climate over the tropical ocean simulated by the piControl run of the CMIP5 experiments (Giorgetta

et al., 2013). The vertical atmospheric profiles and even mean SSTs are remarkably similar. In piControl, the mean SST over the tropical ocean is 298.4 K (Popke et al., 2013). Hence, the ocean is in the T31 version of ECHAM6-RCE 1.7 K warmer, although the mean insolation in the tropics is approximately 400 W m^{-2}, whereas it is set to 340 W m^{-2} in ECHAM6-RCE. The similar SSTs imply that the net transport of energy from the tropics to the extratropics matches the energy surplus due to enhanced solar insolation. Popke et al. (2013) also found a very good agreement of tropical climate and RCE climate. In their study, the accordance of the mean vertical profiles of piControl and of the RCE experiment with the Nordeng convection scheme is stronger than the accordance of the two RCE experiments with differing convection schemes (Nordeng and Tiedtke).

Another, even more idealized RCE setup that is frequently used in other RCE studies is based on fixed SSTs and no diurnal cycle (e.g. Held et al., 2007). Instead, the solar insolation is kept constant at 340.3 W m^{-2}. Figure 3 shows that the vertical profiles in this setup are similar to the control RCE setup, although especially the temperatures in the upper troposphere are somewhat enhanced. Fixed SSTs have the advantage that an equilibrium state is reached within days and not within years, as the atmosphere can adapt much faster than the ocean. Nonetheless, the critical questions in this thesis include surface-atmosphere interactions, so an MLO which can adapt to atmospheric changes is a necessity.

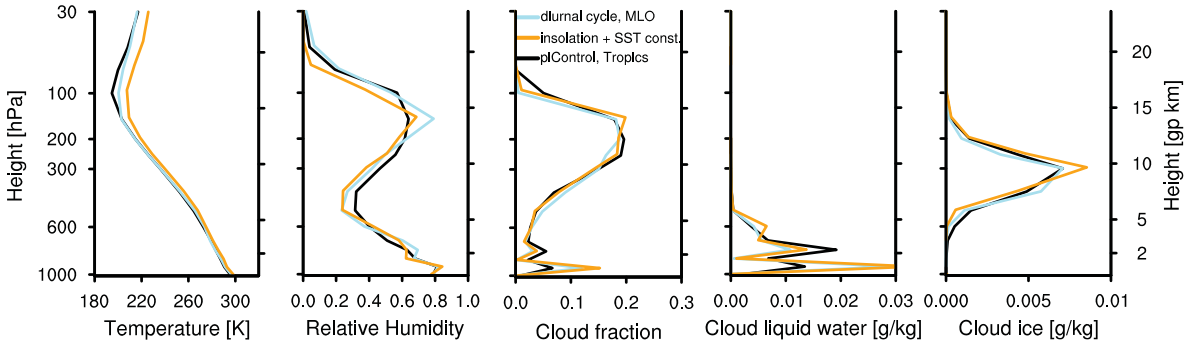

Figure 3: Vertical equilibrium profiles of atmospheric properties in different RCE model configurations (in the control RCE setup with a diurnal cycle and an MLO (T31, zinhomi like T63) and in the setup with fixed SST and fixed solar insolation) compared to the piControl run of the CMIP5 experiments (Giorgetta et al., 2013), considering only values over the tropical ocean of the last 20 years.

The lifetime τ of precipitation clusters in one location can be estimated with the autocorrelation function of the mass-weighted vertical velocity (Figure 4). However, the uncertainty of the calculated timescales is high because the decay of the autocorrelation function is quite different from an exponential decay function:

$$y = \exp\left(\frac{-x}{\tau}\right). \tag{11}$$

Thus, the result depends on the fitting method. Nevertheless, the relative lifetime differences among the experiments can be interpreted.

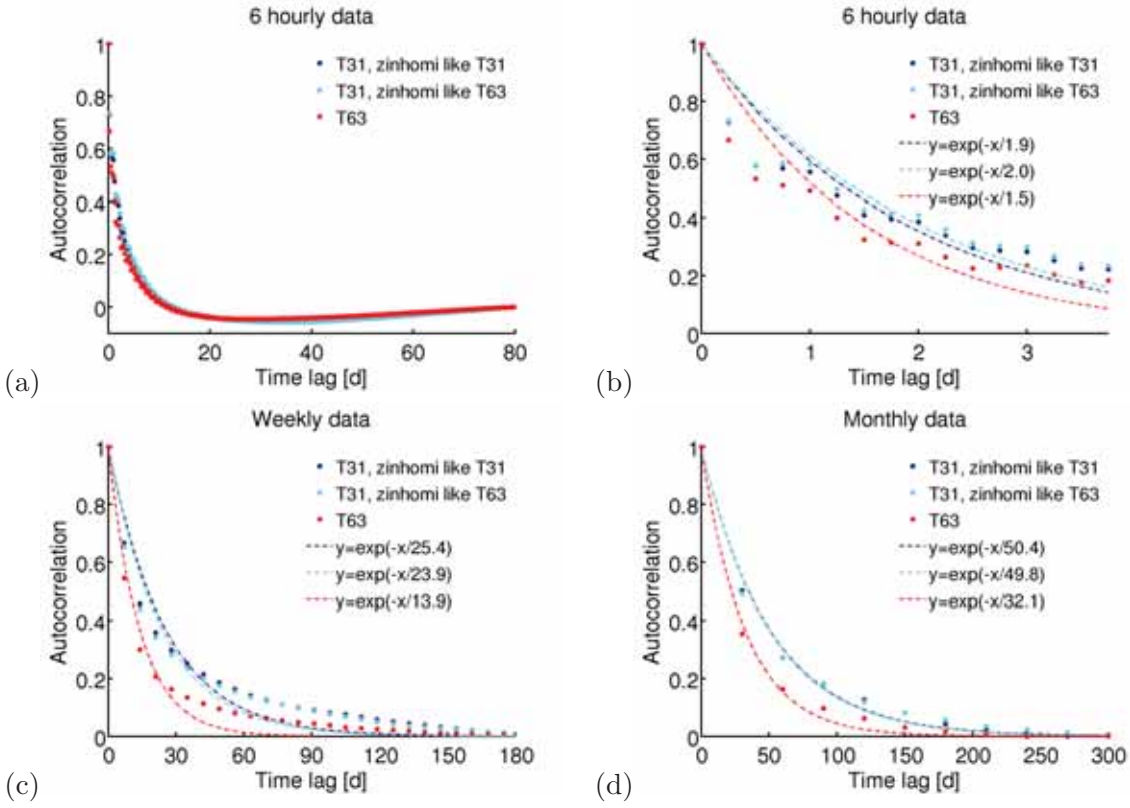

Figure 4: Autocorrelation function of the mass-weighted vertical velocity with (a,b) 6 hourly, (c) weekly and (d) monthly data for different model resolutions with or without constant tuning parameters. The best fitting exponential decay functions are calculated with the least squares method.

Based on the autocorrelation functions with 6 hourly data, the lifetime of the precipitation clusters in one location is rather short, with a lifetime τ between 1.5 and 2.0 days in all the experiments (Figure 4). If weekly data are used, the lifetime increases to values between 25 and 14 days and if monthly data are used, the lifetime further increases to values between 50 and 32 days. This is due to a superposition of short-term processes like the formation of individual convective updrafts and long-term processes which are driven by SST inhomogeneities. Processes on multiple time scales are also reported by Tompkins and Craig (1998b), who conducted RCE experiments with a fixed SST. They found two mixing timescales, a fast timescale related to cumulus updraft mass flux (~2 days) and a slow timescale governed by radiative cooling subsidence speed and the depth of the convecting layer (~20 days). The

latter mechanism is hard to detect in our setup, as it has about the same timescale as the SST inhomogeneities. In the experiment with fixed SSTs and without a diurnal cycle, the cluster lifetime is the same with 6 hourly data, but if monthly data are used, there is already a negative correlation after one month. Probably, an autocorrelation only in the subsidence regime would be needed to identify the subsidence timescale. Because of the multiple timescales, the best averaging period always depends on the timescale of the processes which are important for the specific study.

Although the absolute lifetimes are so different with 6 hourly, weekly and monthly data, the lifetime decreases for all averaging periods robustly by a factor between 25 % and 45 % if the model resolution is increased from T31 to T63. An explanation is that in high resolution, small scale processes with short lifetimes are better resolved. Concerning the 6 hourly data, an interesting sideline is that the autocorrelation is always a little bit enhanced if the time of day is the same. This is due to the impact of the diurnal cycle on convection and vertical velocities. In the experiments without a diurnal cycle of solar insolation, this phenomenon is gone.

The estimated lifetime with the autocorrelation function of the mass-weighted vertical velocity is smaller than the actual lifetime of the precipitation clusters, as the precipitation clusters slowly propagate. Large clusters can be followed up to one year. A preferred direction of propagation is not evident, which is expected as the boundary conditions are homogeneous and as there is no rotation. An influence of the polewards decreasing grid size is not visible.

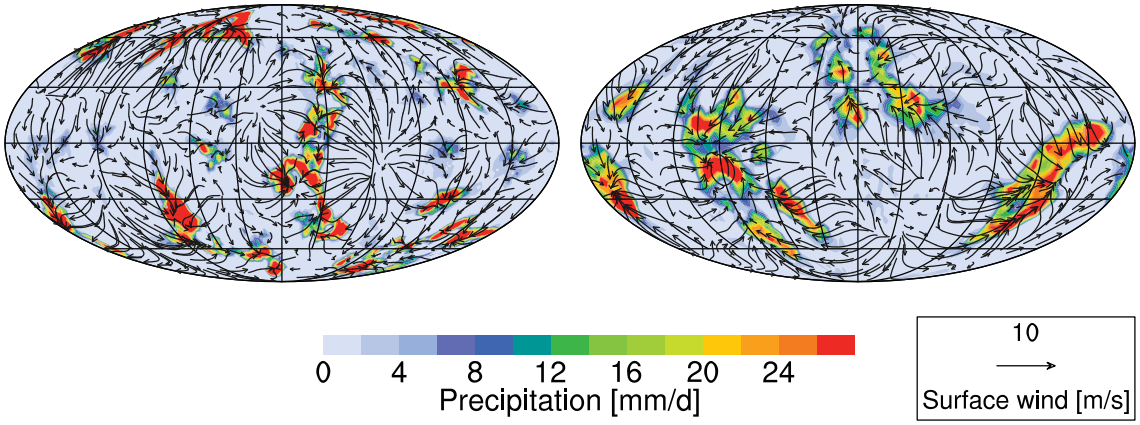

Figure 5: Random snapshots of precipitation clusters and surface wind field in T63 (left) and in T31 (right) averaged over 6 hours.

Apart from the lifetime, another important characteristic of the precipitation clusters is their size. In Figure 5, two random snapshots of precipitation clusters in T31 and T63 are presented. Although two random snapshots are not statistically significant, other snapshots show the same characteristics. The snapshots indicate that in low resolution, areas with high precipitation tend to be connected, while in high resolution, clusters tend to be separated. The surface wind field shows convergence in the areas of the precipitation clusters and divergence in the

areas where convection is suppressed. Hence, in both resolutions, the precipitation clusters are sufficiently long-lived, so the wind field can adapt and an overturning circulation can build up with upsidence in the convective area and subsidence in the regions with suppressed convection. Although there is no Coriolis force, the surface wind speed is similar to observations on earth.

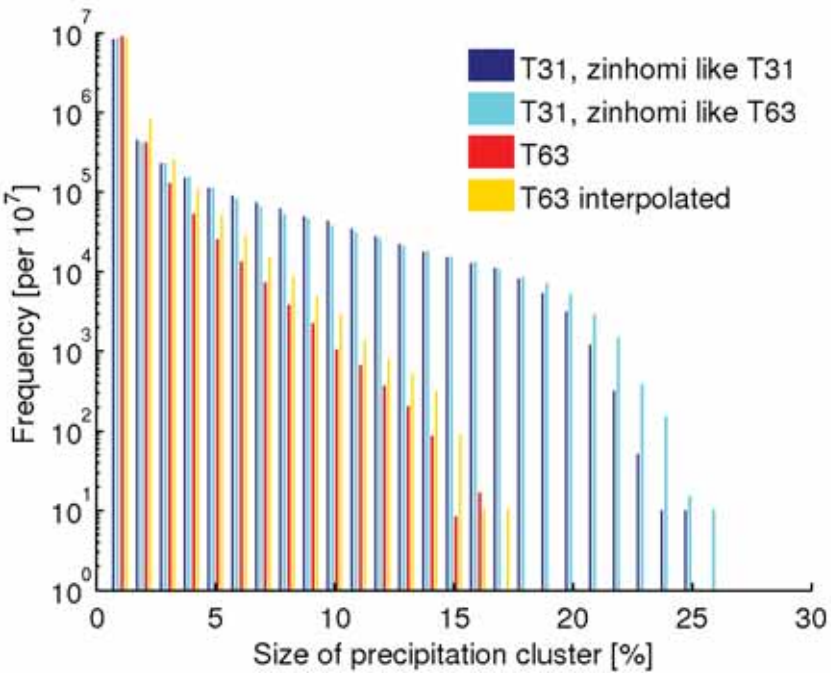

Figure 6: Precipitation cluster size distribution in proportion to earth's surface area for different model resolutions with or without constant tuning parameters. T63 interpolated is the T63 experiment interpolated on a T31 grid. The cluster size is determined by the number of connected grid points with precipitation that is larger than the global mean value, with 6 hourly data.

In order to enhance the level of statistical significance, the cluster size distribution is calculated statistically in Figure 6. The cluster size is determined by counting the connected grid points with precipitation that is larger than the global mean value at each time step. Because of this technique, some clusters are interpreted as being independent although they belong to a larger cluster, but have an area of slight precipitation in between. As a consequence, 85-95 % of the counted precipitation clusters have a size that is smaller than 1 % of earth's surface area. The most important finding is that the cluster sizes in the T31 experiments and the T63 experiment differ significantly. The probability of clusters with sizes larger than 5 % is one to four orders of magnitude higher for the T31 experiments and the maximum cluster size is around 15 % of earth's surface area in T63, while it is around 25 % of earth's surface area in T31. Since the probability is much higher that small clusters can be resolved in high resolution, there are on average 82 clusters per time step in T63, while there are only 30 clusters per time

step in T31. But there are only 2.0 clusters that cover more than 2 % of earth's surface in T63, whereas there are 2.9 of such clusters in T31. This tendency becomes even more obvious when counting the number of clusters that are larger than 5 % of earth's surface per time step, with only 0.24 clusters in T63, while there are still 1.36 of such clusters in T31.

The simplest explanation for the increase of cluster size with decreasing resolution would be that the probability decreases that dry areas within a cluster are resolved. These regions have the potential to cut the cluster in two parts. However, after interpolating the T63 experiment results on a T31 grid, the clusters are still smaller. Instead, the increase of cluster size is related to a change not only in size, but also in shape. In T31, the precipitation clusters tend to be connected, thus they are very long and narrow. Often there is only one large precipitation cluster, meandering over all of the sphere.

4 Transition to a “land-like” planet

The transition of the control aquaplanet RCE setup to a planet with a “land-like” climate needs the adaptation of a couple of key surface features. One of the most important differences is the heat capacity of the mixed layer ocean and the soil. These thermal inertia influence the diurnal cycle of temperature and therefore the stability of the atmosphere. Very important is also the water supply. Whereas the water can evaporate easily over the ocean, the water has to evaporate from wet soil or plants over the land, so for example the stomatal resistance has to be incorporated. This influences the Bowen ratio, which is the ratio of sensible heat flux to latent heat flux (Bowen, 1926). Other important surface properties which will not be investigated in this study are surface albedo and surface roughness. A homogeneous increase of surface albedo leads to a homogeneous decrease of surface temperatures. However, the equilibrium mean surface temperature also depends on the solar insolation. As the solar insolation is highly idealized in the RCE setup, the same is true for the equilibrium mean SST. Hence, there is little point in altering the equilibrium SST by changing the surface albedo. Besides, compared to spatial temperature gradients, the equilibrium mean SST is of minor importance for atmospheric processes. Surface roughness mainly affects the wind field. The influence of surface roughness will be neglected in the following because the focus of this study is more on thermodynamical features.

4.1 Dependence of RCE climate on mixed layer ocean depth

A reduction of mixed layer ocean (MLO) depth and the associated decrease of surface heat capacity results in a faster adaptation of the surface to an energy imbalance. Atmospheric processes are influenced in two ways. On the one hand, a surface with small heat capacity is more closely coupled to the atmosphere because it adapts quickly to local energy imbalances. This can influence for example the time span for which clusters stay in one location. On the other hand, the temperature of a surface with small heat capacity can be altered more easily by the diurnal cycle of solar insolation, leading to an increase of the daily SST amplitude. This can influence clouds and convection and the time of day when they preferentially form. In order to be able to distinguish between those two effects, two experiment series are performed, one with constant solar insolation of 340.3 $\mathrm{W\,m^{-2}}$ and one with a diurnal cycle where the diurnal average of solar insolation is 340.3 $\mathrm{W\,m^{-2}}$.

Popke (2012) reduced the MLO depth from 50 m to 25 m and found slightly more variance in surface temperatures, but otherwise an almost negligible influence on RCE climate. Because of that, in all of the experiments presented here, the MLO depth is reduced more strongly. In the experiment series without a diurnal cycle, the MLO depth is reduced thrice, from 50 m to 1 m to 0.1 m to 0.02 m. In addition to these MLO depths, experiments with intermediate MLO depths of 5 m and 0.05 m are carried out in the experiment series with a diurnal cycle in order to enhance resolution and simplify analysis.

4.1.1 Effect of enhanced surface coupling on RCE climate

In the RCE setup without a diurnal cycle of insolation, a reduction of MLO depth leads to a stronger coupling of the surface to the atmospheric energy fluxes. Figure 7 explains this fact. For smaller MLO depths, the distribution of monthly averaged SSTs is broadened. This is simply due to non-equilibrium atmospheric fluxes which can perturb the SST in a short period of time more strongly if the heat capacity of the surface is small. Respectively, the SST perturbations can alter atmospheric processes. The result is a stronger coupling of the atmosphere to the SST. The most striking result is a similar shape of the SST distribution for MLO depths of 1 m, 0.1 m and 0.02 m. This indicates that most of the atmospheric processes which influence the energy balance change on timescales on which a 1 m deep MLO can already adapt, so there is not much difference to experiments with even smaller MLO depths. Table 7 further shows that equilibrium mean SSTs are in a range of 0.4 K and that the skewness is very small for all MLO depths. This indicates that no further feedback factors dominate the system.

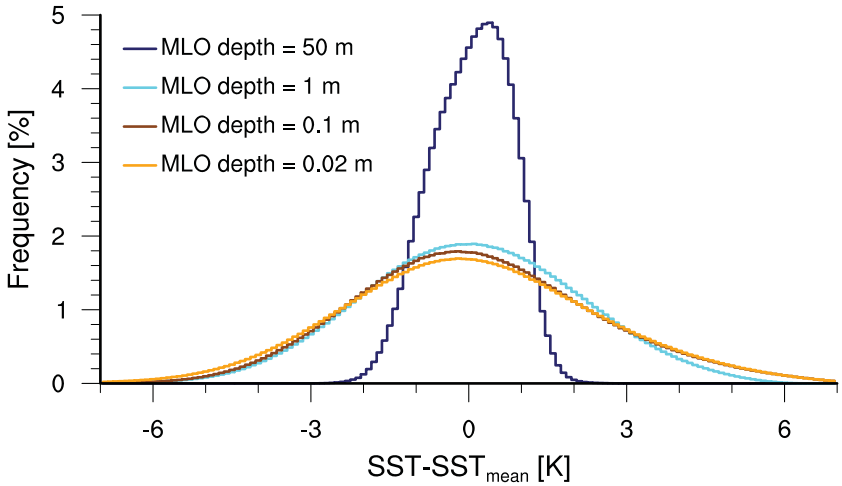

Figure 7: Histogram of daily averaged SSTs of all grid points in equilibrium relative to the global mean value for different mixed layer ocean depths (50 m, 1 m, 0.1 m and 0.02 m) of the experiments without a diurnal cycle of solar insolation. Each grid point is weighted by its area. The bin size is 0.1 K.

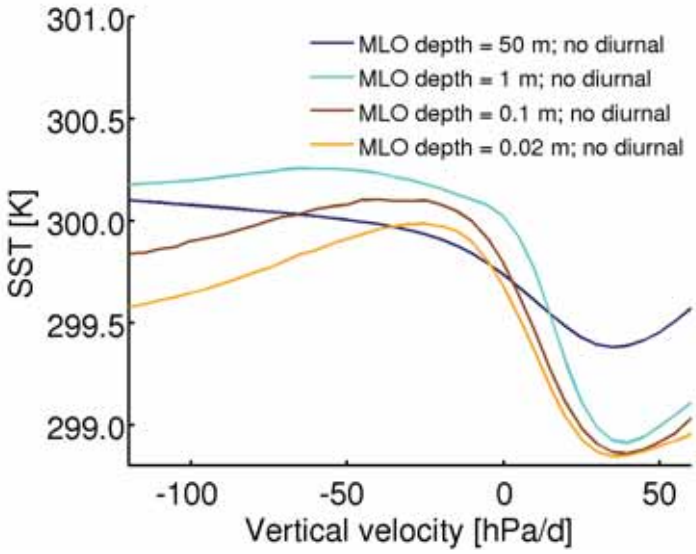

Figure 8: 6 hourly values of SST versus mass-weighted vertical velocity for different mixed layer ocean depths without a diurnal cycle of solar insolation. The SST is assigned to the vertical velocity at 5 hPa/d intervals.

Figure 8 illustrates the dependence of SST on vertical velocity. In general, the SSTs are higher in the upsidence regime than in the subsidence regime because convection triggers at the location with the highest surface temperature. This is not only because the atmosphere is least stratified there, but also because the latent heat flux increases over a warm ocean, moistening the atmospheric boundary layer and reducing convective inhibition (CIN). In the subsidence regime, the SST is in all experiments lowest at a vertical velocity of approximately 35 hPa/d (Figure 17 and Table 8), which can be associated with the downward motion resulting from clear-sky radiative cooling and dry adiabatic warming. Stronger subsidence indicates dynamically enforced downward motion, for example due to upper tropospheric convergence. As a consequence, both tropospheric and surface temperatures increase. The temperature gradient between the subsidence and upsidence regime is enhanced for the experiments with MLO depths of 1 m or smaller. The SST in the upsidence regime is of special importance since in the tropics the thermal structure is determined by the moist adiabatic lapse rate, which depends on the SST in the convective regions. Internal gravity waves ensure an efficient energy transport from the convectively heated areas to the subsidence areas. On a planet with Coriolis force, this transport would be restricted. In the experiments with small MLO depths, the SST decreases in areas of strong upward motion by approximately 0.5 K, while SSTs in the 50 m experiment slightly increase. Hence, the effect of deep clouds to decrease the incoming shortwave radiation dominates, which results in a negative energy imbalance and in an efficient cooling of surfaces with small heat capacity. In addition, upward motion is not necessarily induced by high SSTs, but by high surface moist entropy. A consequence of the surface cooling

is that the convective clusters move faster. The autocorrelation of vertical velocities, calculated analogous to Figure 4 with 6 hourly data, decreases continuously with decreasing MLO depth (Appendix Figure A.1). The calculated lifetime in the 0.02 m experiment is a quarter less than in the 50 m experiment.

Although SSTs differ in the upsidence regime by about 0.5 K, Figure 9 shows that atmospheric properties are almost independent of MLO depth for the experiments without a diurnal cycle. This leads to the conclusion that a 0.5 K SST difference is too small to have an influence on the atmospheric properties. The only differences are a somewhat less pronounced humidity minimum in the middle troposphere and a slightly enhanced cloud fraction in the upper troposphere for small MLO depths. However, these changes are so marginal that one can conclude that the enhanced surface coupling due to decreased heat capacity of the surface has little effect on the equilibrium mean atmospheric properties.

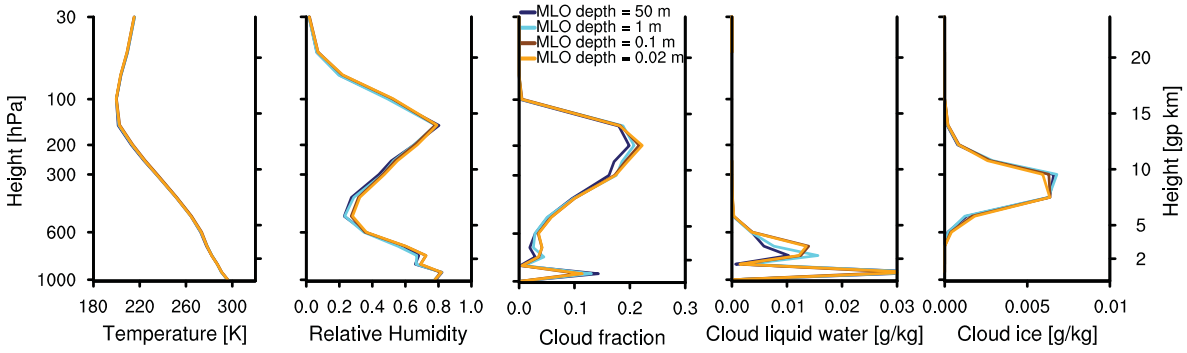

Figure 9: Vertical equilibrium profiles of atmospheric properties for different mixed layer ocean depths without a diurnal cycle of solar insolation.

4.1.2 Sensitivity of RCE climate to the diurnal cycle

In the RCE experiments with a diurnal cycle of insolation, atmospheric properties can both be altered by the enhanced coupling to the surface and by the increasing diurnal SST amplitude with decreasing MLO depth (Figure 11). Table 7 shows that equilibrium mean SSTs vary more in the experiments with a diurnal cycle than in the experiments without. This is especially true if the MLO depth is smaller than 1 m. While the equilibrium mean SST is still similar in the experiments with MLO depths of 50 m, 5 m and 1 m, it increases by more than 1 K in the experiment with an MLO depth of 0.1 m and decreases by more than 2 K in the experiment with an MLO depth of 0.02 m. Figure 10 and Table 7 give a first explanation for this strong SST decrease. For an MLO depth of 0.02 m, the distribution of monthly mean SSTs is negatively skewed with $\xi_{\mathrm{SST}} = -0.7$, indicating that there must be a positive feedback mechanism leading to very small monthly mean temperatures. Another consequence of the strong increase of negative skewness is an increase of standard deviation. This is particularly striking in

comparison to the experiments without a diurnal cycle. Besides, it is counterintuitive that the spatial standard deviation is smaller in the 0.1 m experiment than in the 1 m experiment.

	with diurnal cycle				*without diurnal cycle*			
MLO depth	SST [K]	σ_{SST} [K]	ξ_{SST}	P [mm/d]	SST [K]	σ_{SST} [K]	ξ_{SST}	P [mm/d]
50 m	300.1	0.8	-0.1	4.1	299.6	0.6	-0.2	4.0
5 m	299.5	2.2	-0.2	4.0	-	-	-	-
1 m	299.8	4.0	0.1	4.0	299.5	4.2	0.0	4.0
0.1 m	301.3	3.5	0.1	4.4	299.3	5.2	0.2	4.0
0.05 m	300.1	6.6	-0.6	4.3	-	-	-	-
0.02 m	298.6	9.2	-0.7	4.4	299.2	5.8	0.1	4.0

Table 7: First three moments of daily mean SST and mean precipitation for different MLO depths with and without a diurnal cycle. σ_{SST} and ξ_{SST} denote the spatial standard deviation and skewness of the daily mean SST fields averaged over all time steps in equilibrium.

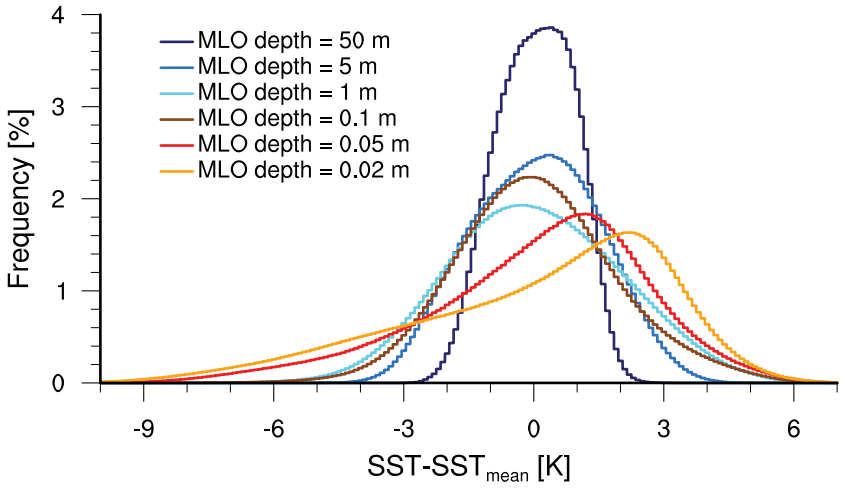

Figure 10: Histogram of daily averaged SST perturbations at all grid points relative to the global mean value for different mixed layer ocean depths (50 m, 5 m, 1 m, 0.1 m, 0.05 m and 0.02 m) of the experiments with a diurnal cycle, considering only the time period in equilibrium. Each grid point is weighted by its area. The bin size is 0.1 K.

Figure 11 depicts the diurnal cycle of SST, precipitation and vertically integrated cloud water for decreasing MLO depths. In all experiments, the SST maximum is reached in the afternoon or early evening, so there is a phase shift compared to the incoming solar radiation. The solar radiation is the initial driver of the diurnal cycle and maximizes at noon. The diurnal SST amplitude is 0.04 K in the 50 m experiment and 1.8 K in the 1 m experiment, but about 11 K in the 0.1 m experiment and 15 K in the 0.02 m experiment. Therefore, only for MLO depths smaller than 1 m, the diurnal SST range is strong enough to have an impact on atmospheric processes. Over land, it is more common to measure the 2 m temperature than the skin temperature. The diurnal 2 m temperature range (DTR) is about 6 K in the 0.1 m

experiment and 10 K in the 0.02 m experiment. On earth, the DTR varies approximately by 6-10 K in wet tropical areas over land, but in dry tropical regions, the DTR can be larger than 15 K [1]. According to Jackson and Forster (2010), the mean diurnal temperature range over the global land surface is 11 K. In dry climates, the diurnal temperature range is larger because the surface can cool more effectively at night through longwave radiation and warm more effectively during the day because solar insolation increases and latent heat fluxes are smaller, which would cool the surface especially during the day. In all of the experiments with MLO depths of 0.1 m or smaller, the DTR agrees well with diurnal temperature ranges in the tropics over land.

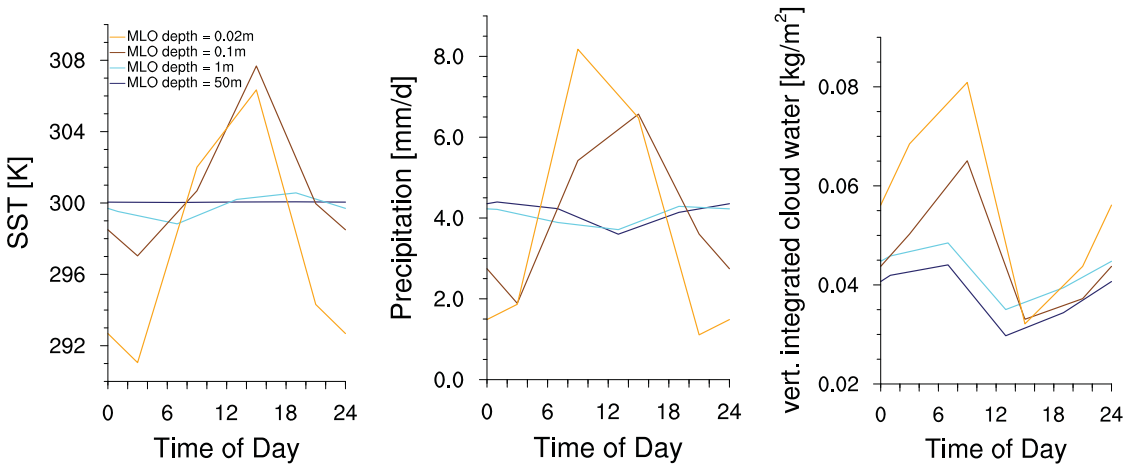

Figure 11: Diurnal cycle of temperature, precipitation and vertically integrated cloud water for different mixed layer ocean depths. The values are averaged over 6 hours, with the data point located at the center of the output interval.

The diurnal cycle of precipitation illustrates that only for MLO depths of 0.1 m or smaller, the diurnal SST amplitude is strong enough to have a substantial impact on atmospheric processes. In the experiments with an MLO depth of 1 m or greater, there is a precipitation maximum at night and a minimum at noontime, with an amplitude that is less than 20 % of the mean precipitation rate. This is consistent with measurements on earth over the oceans (Bowman et al., 2005). Kraus (1963) argues that the nocturnal maximum is due to the stabilizing effect of solar heating of cloud tops during the day and the destabilizing effect of nighttime radiative cooling at cloud tops. In accordance with that, diurnal temperatures change most in the 300 hPa level, which is dominated by high clouds. In the experiments with an MLO depth of 0.1 m or smaller, precipitation peaks during the day and the contrast of day- and nighttime precipitation increases strongly. The experiments differ concerning the time of day, at which the precipitation peaks. While precipitation peaks in the 0.1 m experiment in the afternoon, it peaks in the 0.02 m experiment already in the morning, with a

[1] Source: www.weatherbase.com

value that is 4 times as large as at night. Hence, precipitation peaks too early in this setup compared to the real tropics over land. Precipitation peaking too early during the day is a common problem in GCMs (e.g. Bechtold et al., 2004, Lawrence and Slingo, 2005). The problem is related to the inability of GCMs to reproduce the gradual growth of deep clouds over approximately three hours. Instead, precipitation is in phase with convective available potential energy (CAPE) and CIN, which is consistent with the CAPE closure used in the bulk mass-flux scheme (Bechtold et al., 2004). In the RCE setups with small MLO depths, there is not much cloud water left in the afternoon because of the heavy rain in the morning. Hence, precipitation decreases although the atmosphere is most conditionally unstable in the afternoon. In the 0.1 m experiment, it rains less in the morning because the SST does not increase as strongly as in the 0.02 m experiment, resulting in slightly less moist convection. However, time is poorly resolved, so the time seperation between the precipitation maxima in the 0.1 m and 0.02 m experiment might be exaggerated by the output interval.

Another noteworthy fact is that global mean precipitation is approximately the same in the experiments with MLO depths of 0.1 m or less (Table 7). This signifies that precipitation is not coupled to global mean SSTs, which decrease from 301.3 K in the 0.1 m experiment to 298.6 K in the 0.02 m experiment, but to daily maximum SSTs, which are similar. Hence, the moist adiabatic lapse rates and the atmospheric cooling rates are also similar and lead to the same convective response. During the night, a 0.02 m deep MLO cools more effectively than a 0.1 m deep MLO. This phenomenon is known in the scientific community as rectification (Cronin and Emanuel, 2012). The SST increase during the day is dampened because latent and sensible heat fluxes act against the warming, while the surface can cool at night efficiently as a nocturnal inversion builds up, suppressing turbulent heat fluxes. The rectification is one reason for the strong decrease of equilibrium mean SSTs from the 0.1 m to the 0.02 m experiment.

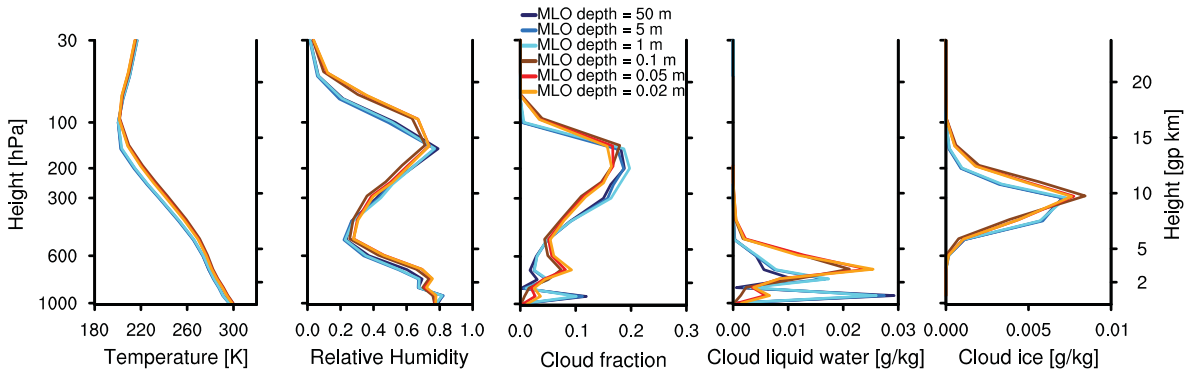

Figure 12: Vertical equilibrium profiles of atmospheric properties for different MLO depths.

The vertical atmospheric profiles in Figure 12 emphasize the importance of the diurnal cycle of SSTs on atmospheric processes. While the vertical profiles are similar for an MLO depth of 1 m or larger, a transition occurs for smaller MLO depths resulting from the strong diurnal cycle of SSTs and the shift of precipitation maximum from night- to daytime (Figure 11). In those experiments, the upper tropospheric temperatures increase relative to the experiments with deeper MLOs, illustrating the coupling to the daily maximum SST and therefore a decrease of lapse rate which is linked to a change of the moist adiabat. As a consequence of the increased upper tropospheric temperatures, the relative humidity profiles are shifted upward. Besides, there are more stratus clouds at 700 hPa while there are fewer high clouds and fewer boundary layer clouds. This is consistent with a shift of the peak in cloud liquid water from the boundary layer to the 700 hPa layer. The reduction of boundary layer clouds can be explained with a strong diurnal temperature cycle not only at the surface, but also in the atmospheric boundary layer. Because of that, the boundary layer height increases and moisture is mixed through a deeper layer. Hence, the probability of a temperature inversion near the surface with high fog is strongly reduced. The reduction of boundary layer clouds is the main reason for the strong SST increase in the 0.1 m experiment, since low clouds have a strong cooling effect.

In the aquaplanet setup of ECHAM, shallow convection terminates approximately at 700 hPa (Möbis and Stevens, 2012). If not all conditions are fulfilled for deep convection, especially if the total derivative of vertically integrated specific humidity is not larger than the latent heat flux, the convection remains shallow. This often leads to a 700 hPa cloud peak in the subsidence regime which appears exaggerated relative to what is observed, and likely represents too much detrainment from shallow convection. In this setup, the increase of 700 hPa layer clouds is also an indirect consequence of the diurnal SST amplitude and the decrease of boundary layer clouds. On the one hand, the height of the capping inversion above the boundary layer is moved upward if the diurnal SST amplitude is large, on the other hand, the coupling of SST to 700 hPa cloud amount increases because boundary layer clouds are missing. This situation introduces a positive feedback mechanism, where 700 hPa layer clouds lead to surface cooling which strengthens the capping inversion. Besides, the inversion is strengthened by internal gravity waves which ensure an efficient energy transport in the free troposphere from the convectively heated areas to the subsidence areas. This reasoning is additionally substantiated by Figure 13. It shows that very low temperatures in the 0.02 m experiment can be associated with a high 700 hPa cloud fraction and a temperature inversion at the same height, while there are hardly any clouds at the other levels. The climatic importance of these stratus clouds is further increased as they are almost the only clouds forming in subsidence areas (Figure 14). Besides the pronounced peak of clouds in the 700 hPa layer, the cold SST and strong subsidence area both share a temperature inversion at 700 hPa and a very dry middle troposphere.

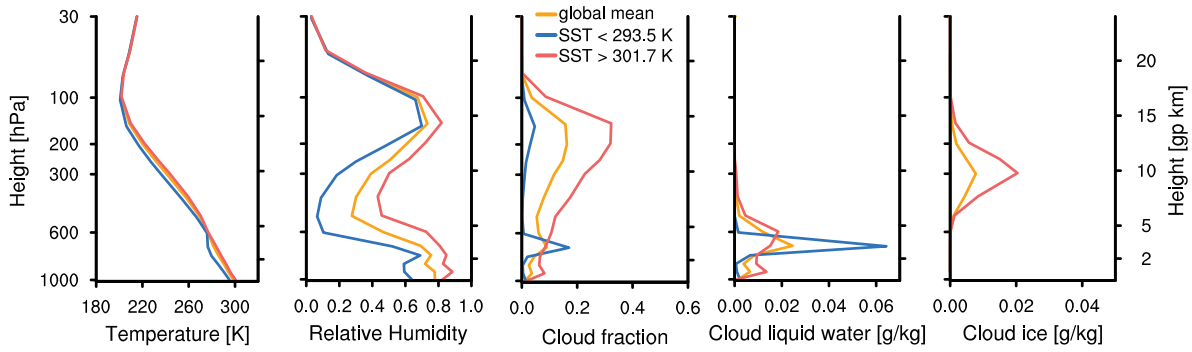

Figure 13: Vertical equilibrium profiles of atmospheric properties in the experiment with an MLO depth of 0.02 m over a cold (monthly mean SST < 293.5 K) or warm (monthly mean SST > 301.7 K) surface in comparison to the global mean atmospheric profiles. The threshold values are the 5$^{\text{th}}$ and 95$^{\text{th}}$ percentile of the monthly mean SST distribution.

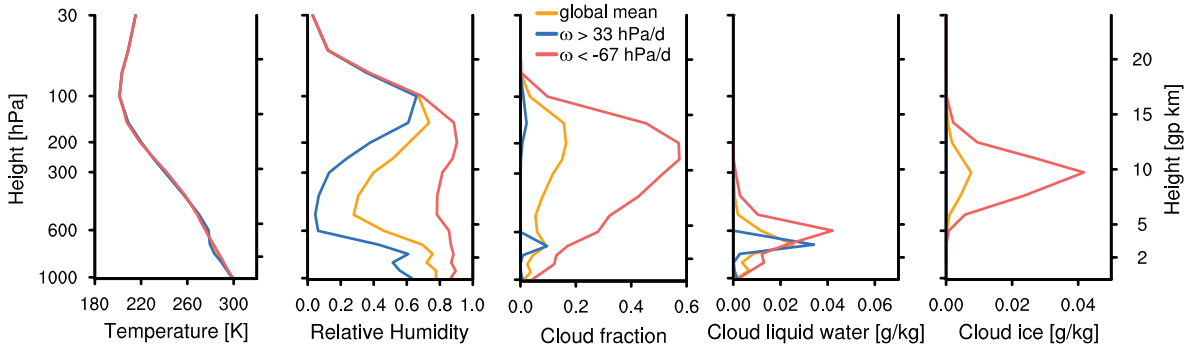

Figure 14: Vertical equilibrium profiles of atmospheric properties in the experiment with an MLO depth of 0.02 m over strong subsidence ($\omega > 33$ hPa/d) or upsidence ($\omega <$ -67 hPa/d) regions in comparison to the global mean atmospheric profiles. The threshold values are the 5$^{\text{th}}$ and 95$^{\text{th}}$ percentile of the distribution of the monthly averaged mass-weighted vertical velocity ω, which is defined in Section 2.2.

After taking a brief look at Figure 15, the high degree of similarity of the vertical profiles for very strong subsidence and very low SSTs is no longer surprising because the lowest SSTs occur in the regions of strongest downward velocities in the 0.05 m and 0.02 m experiments. This contrasts with the observed warming for $\omega > 35$ hPa/d in the experiments without a diurnal cycle (Figure 8). In the 0.05 m and 0.02 m experiments, the free tropospheric warming does not influence the SST because the strong 700 hPa inversion decouples the free troposphere from the surface. The strong subsidence also results in an extremely dry middle troposphere, which is clearly visible in Figure 13 and Figure 14, enabling an effective cooling of the 700 hPa cloud tops. The high degree of similarity of the vertical temperature profiles in different circulation regimes (Figure 14) indicates that internal gravity waves spread energy very efficiently from

convectively heated upsidence areas to subsidence areas. Another interesting difference to the simulations without a diurnal cycle is the lack of cooling in the upsidence regime, even for very small MLO depths. This indicates that the properties of clouds, convection and upward motion have changed.

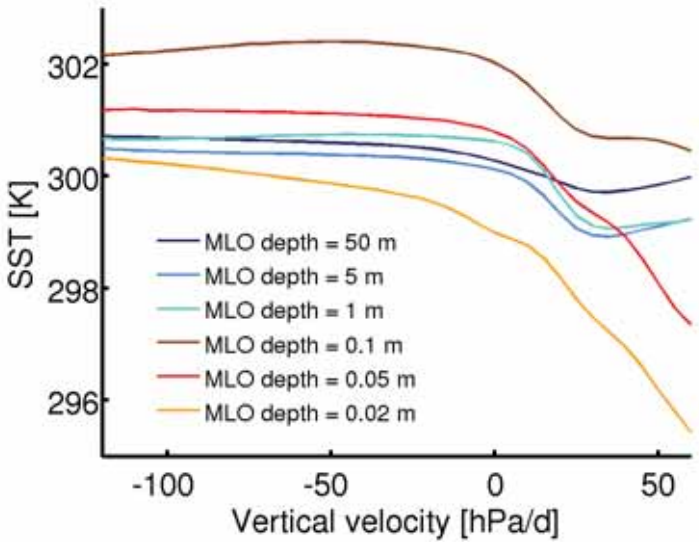

Figure 15: Daily values of SST versus mass-weighted vertical velocity for different mixed layer ocean depths. The SST is assigned to the vertical velocity at 5 hPa/d intervals.

The connection of 700 hPa layer clouds and of the SST is illustrated in Figure 16. The vertical cross sections of cloud cover and wind field, centered at the location with the minimum monthly mean SST, show that in the experiments with MLO depths of 50 m, 5 m and 1 m, 700 hPa layer clouds have little influence on the SST, as there are other cloud layers below. In the experiment with an MLO depth of 0.1 m, 0.05 m and 0.02 m, 700 hPa layer clouds have the potential to dominate the SST in the subsidence regime, as the boundary layer clouds are gone due to the enhanced diurnal SST amplitude and as there are no clouds above. However, at the location of minimum SST, there are no 700 hPa layer clouds in the 0.1 m experiment. This can be explained with dry and warm subsiding air masses leading to cloud dissipation. This effect is also evident in the 0.05 m and 0.02 m experiments, but it is dominated by the processes which create a strong 700 hPa inversion. Because of that, the positive feedback between 700 hPa clouds and SST enables very small monthly mean SSTs. This is the reason for the observed negative skewness of the distribution of monthly mean SSTs in the 0.05 m and 0.02 m experiments (Figure 10 and Table 7). In addition to the rectification argument, this feedback mechanism provides another reason why the equilibrium mean SST drops when the MLO depth decreases from 0.1 m to 0.02 m.

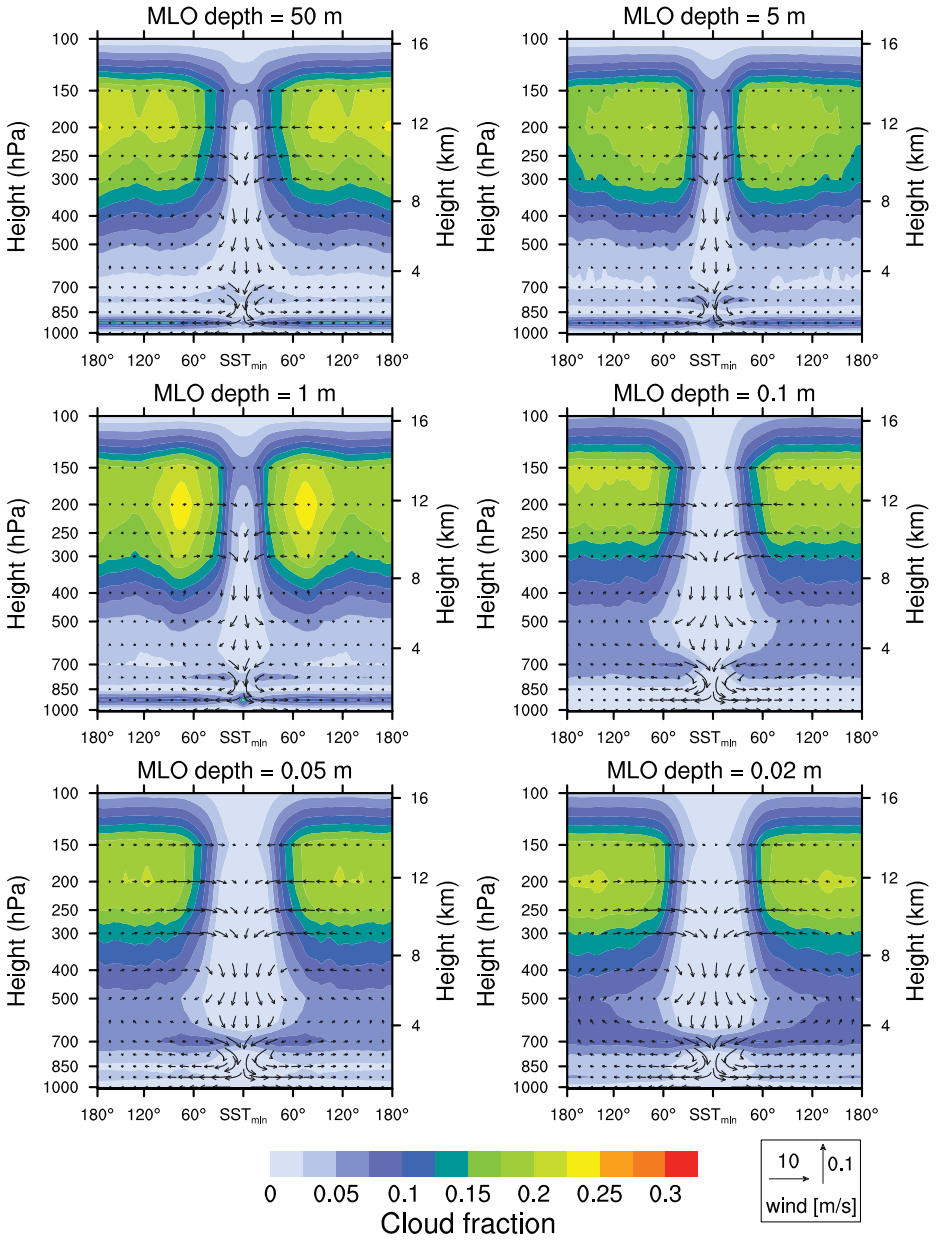

Figure 16: Vertical cross sections of mean cloud cover and wind field for MLO depths of 50 m, 5 m, 1 m, 0.1 m, 0.05 m and 0.02 m. The cross sections are centered at the location with the minimum monthly mean SST and show the vertical profiles along that longitude. The cycle is closed with the longitude on the other side of the planet. The vertical velocity is scaled with a factor of 100. The data is averaged over all time steps in equilibrium.

The dependence of the large-scale circulation on MLO depth is illustrated in Figure 17. All distributions of mass-weighted vertical velocity are negatively skewed with the highest statistical weight located in the subsidence regime. The most likely vertical velocity is determined by the ratio of the clear-sky cooling rate and the lapse rate of dry static energy. The lapse rate

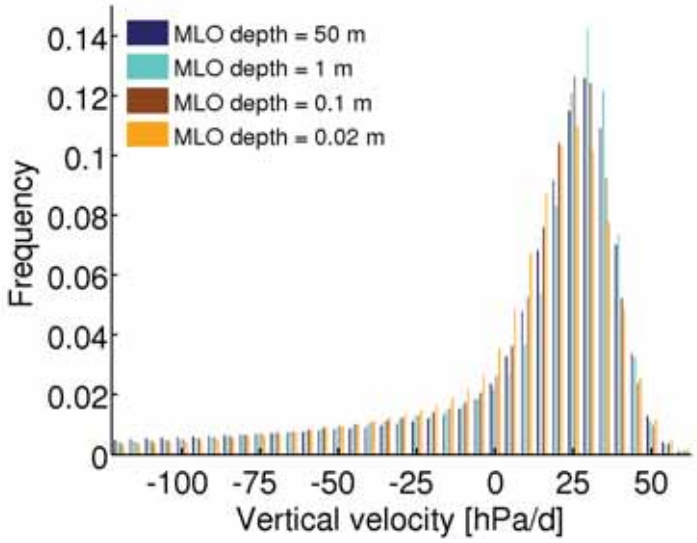

Figure 17: Histogram of the mass-weighted vertical velocity for different MLO depths, using daily data and considering all days in equilibrium. The data are binned by 5 hPa d^{-1}.

MLO depth	$T_s - T_{200}$ [K]	$\omega_{p_{max}}$ [1]	$A_{\omega \geqslant 0}$	$A_{\omega<0}$	$\overline{\omega \geqslant 0}$ [1]	$\overline{\omega < 0}$ [1]	OC [1]
50 m	85.6	30	0.74	0.26	26	-74	100
5 m	85.5	30	0.74	0.26	27	-79	106
1 m	85.0	30	0.73	0.27	27	-73	100
0.1 m	80.0	25	0.73	0.27	25	-67	93
0.05 m	79.8	25	0.72	0.28	23	-60	83
0.02 m	78.6	25	0.73	0.27	23	-62	85

Table 8: Difference between 200 hPa (T_{200}) and surface temperature (T_s), vertical velocity at the highest statistical weight $\omega_{p_{max}}$ binned by 5 hPa d^{-1}, area $A_{\omega \geqslant 0}$ with descending air and $A_{\omega<0}$ ascending air, mean vertical velocity of descending air $\overline{\omega \geqslant 0}$ and ascending air $\overline{\omega < 0}$ and strength of overturning circulation OC, which is defined as difference of $\overline{\omega \geqslant 0}$ and $\overline{\omega < 0}$. The separation in dynamical regimes is based on daily values.
[1] Values are given in hPa d^{-1}.

decreases in the experiments with a strong diurnal cycle because daily maximum temperatures increase and change the moist adiabat. The lapse rate decrease is also evident in the decrease of temperature difference between surface and 200 hPa temperatures (Table 8). Consequently, the highest statistical weight is shifted from 30 hPa d^{-1} for the experiments with MLO depths of 1 m or larger to 25 hPa d^{-1} for the experiments with MLO depths of 0.1 m or less. For the same reason, the mean vertical velocity of descending air decreases. Not only the velocity of descending air decreases, but also the velocity of ascending air decreases since latent heat is transported more efficiently into the atmosphere. Hence, the overturning circulation weakens (Table 8), which is a common feature in a warmer climate (Bony et al., 2013b). However, Bony

et al. (2013b) relate the weakening of overturning circulation to a decrease of radiative cooling in response to increasing CO_2 concentrations, while in this case it is related to a change of the effective lapse rate. The decrease of mean upsidence and subsidence velocity are not totally coupled because the area of ascending air increases slightly. Hence, the mean vertical velocity decreases more in the upsidence than in the subsidence regime. The increase of upsidence area can be explained with a strong triggering of convection by the high surface temperatures during the day, though the high stability of the atmosphere impedes strong upward motion.

4.1.3 Influence of MLO depth on climate sensitivity

The influence of MLO depth on climate sensitivity is investigated with another experiment series, in which the experiments with and without a diurnal cycle are repeated with quadrupled CO_2 concentrations. The equilibrium climate sensitivity (ECS) is defined as the equilibrium temperature increase after doubling the CO_2 concentration. As a good approximation, this is equivalent to half of the SST difference of the experiments with quadrupled (SST_{4xCO_2}) and preindustrial (SST_{ctrl}) CO_2 concentrations:

$$\Delta T_{2xCO_2} \simeq \frac{1}{2}(SST_{4xCO_2} - SST_{ctrl}). \tag{12}$$

Table 9 and Figure 18a give an overview about the equilibrium mean SSTs and the climate sensitivities for different MLO depths. In general, the ECS ranges between 1.6 and 2.4 K. The ECS of 2.2 K in the experiment with a 50 m deep MLO and a diurnal cycle agrees well with the ECS of 2.1 K which Popke et al. (2013) found with a higher resolution (T63), but otherwise the same ECHAM6 RCE model setup. The similar ECS also justifies the applied model setup with the low resolution (T31). However, in RCE, the ECS is only about half as large as in the standard ECHAM6 configuration, for which $\Delta T_{2xCO_2} = 3.4$ K. If only the surface temperature changes of the tropical oceans are considered, the ECS reduces to 2.6 K (Popke et al., 2013), but is still larger than the ECS in all RCE experiments. Explanations for this discrepancy are that the enhanced warming of the continents and the extratropics is felt by the tropical ocean and that low-cloud feedbacks are substantially weaker in RCE (Popke et al., 2013).

Another factor that needs to be considered is atmospheric energy leakage, which is a known issue in all ECHAM6 versions until ECHAM 6.2 (Stevens et al., 2013). Unfortunately, the energy leakage depends among others on temperature and can therefore alter the ECS. As the energy leakage is between 0.5 and 0.9 $W\,m^{-2}$ stronger in the $4xCO_2$ experiments than in the control experiments, the climate sensitivity would be without the energy leakage a few tenths of degrees higher. This effect is neglected in this section but will be considered in Section 4.2.2 because energy leakage changes more in the experiments with increasing evaporation resistance. Nevertheless, energy leakage might explain some of the ECS discrepancy in the RCE and standard configuration.

	with diurnal cycle			*without diurnal cycle*		
MLO depth	SST_{ctrl}	SST_{4xCO_2}	ΔT_{2xCO_2}	SST_{ctrl}	SST_{4xCO_2}	ΔT_{2xCO_2}
50 m	300.1	304.5	2.2	299.6	304.2	2.3
5 m	299.5	303.7	2.1	-	-	-
1 m	299.8	304.5	2.4	299.5	303.7	2.1
0.1 m	301.3	304.5	1.6	299.3	304.1	2.4
0.05 m	300.1	304.1	2.0	-	-	-
0.02 m	298.6	303.4	2.4	299.2	304.1	2.4

Table 9: Equilibrium global mean SST and climate sensitivity for different MLO depths with and without a diurnal cycle. SST_{ctrl} and SST_{4xCO_2} denote surface temperatures with preindustrial and quadrupled CO_2 concentrations and ΔT_{2xCO_2} is the climate sensitivity calculated according to Equation 12. The values are given in K.

Without a diurnal cycle, the MLO depth has little influence on atmospheric processes in the experiments with preindustrial and quadrupled CO_2 concentrations (Figure 9 and Figure A.3 in the Appendix), resulting in similar climate sensitivities between 2.1 and 2.4 K. Figure 18b shows that the planetary albedo increases with decreasing MLO depth both in the experiments with preindustrial and quadrupled CO_2 concentrations. This indicates that the cloud cover slightly increases if the atmosphere is closely coupled to the surface. Indeed, the total cloud cover increases from 59 % in the 50 m control experiment to 63 % in the 0.02 m control experiment. However, the increase in cloud cover also leads to a decrease of outgoing longwave radiation (OLR), which roughly balances the reduction of shortwave insolation at the surface (Appendix Figure A.5). Because of that, the cloud feedback as well as the water vapor and lapse rate feedback are in the setup without a diurnal cycle approximately independent of MLO depth (Figure 19). The feedbacks are calculated with the PRP module, which is explained in Section 2.2. The absolute values of water vapor and lapse rate feedback are about 3 $W m^{-2} K^{-1}$, which is more than expected from previous studies. For example, the water vapor feedback calculated by Klocke et al. (2013) with the PRP module in ECHAM5.4 is 1.78 $W m^{-2} K^{-1}$, while the lapse rate feedback is only -0.42 $W m^{-2} K^{-1}$. However, these are global mean values. In the tropics, higher absolute values are reasonable since there is more water vapor in the atmosphere.

With a diurnal cycle, the ECS remains approximately constant for an MLO depth of 1 m or more, where the diurnal SST amplitude does not influence atmospheric processes yet. For an MLO depth of 0.1 m, the ECS is smallest, before it strongly increases if the MLO depth is further reduced. In the experiments with quadrupled CO_2 concentrations, the equilibrium SSTs are scattered less than in the control experiments. Consequently, the climate sensitivity is smallest in the experiment where the equilibrium SST maximizes in the control experiments, namely for an MLO depth of 0.1 m. With quadrupled CO_2 concentrations, the equilibrium SST does not increase in the 0.1 m experiment relative to the 1 m experiment although it

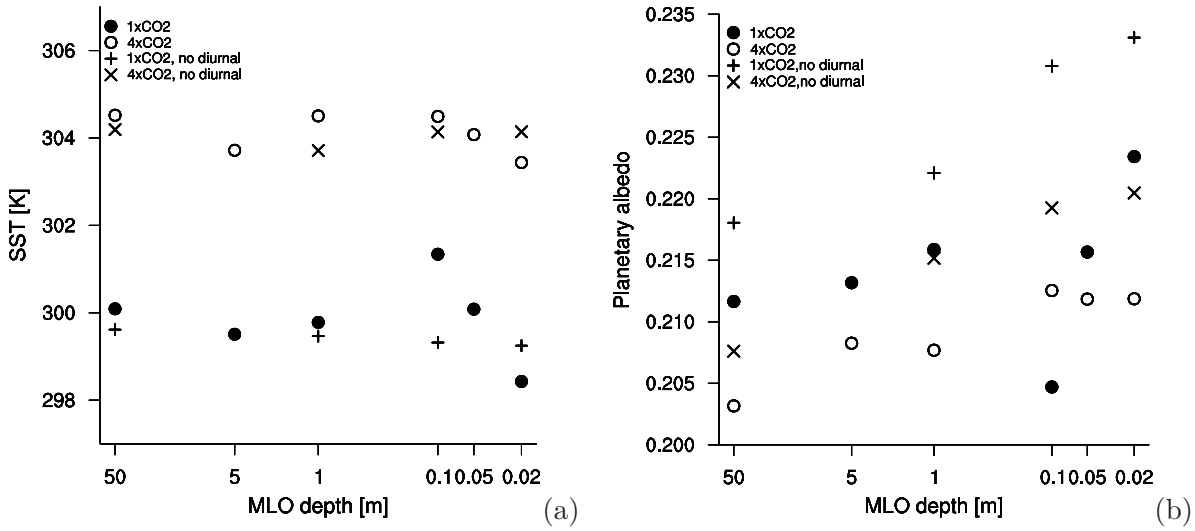

Figure 18: Equilibrium mean SSTs of the experiments with preindustrial and quadrupled CO_2 concentrations (a) and planetary albedo (b) for different MLO depths on a logarithmic scale. The experiment series with and without a diurnal cycle are presented both.

increases in the control experiments by 1.5 K. The explanation is that there are hardly any boundary layer clouds for any MLO depth in the 4xCO_2 experiments (Appendix Figure A.2), while they are removed in the control experiments because boundary layer height increases and moisture is mixed through a deeper layer due to the increasing influence of the diurnal SST amplitude. Figure 19 shows that the cloud feedback decreases in the 0.1 m experiment from 0.8 W m^{-2} K^{-1} to 0.2 W m^{-2} K^{-1} mainly because the shortwave cloud feedback becomes negative, indicating that the small ECS in the 0.1 m experiment is related to the dissipation of boundary layer clouds in the control experiment. In the experiments with MLO depths larger than 0.1 m, the positive shortwave cloud feedback from the dissipation of boundary layer clouds compensates a negative shortwave cloud feedback from increased cloud fraction in the low troposphere.

The 700 hPa clouds reduce the equilibrium mean SST in the experiments with increased CO_2 concentration less effectively as the atmosphere is more opaque, leading to a weaker inversion because the 700 hPa cloud tops cool less efficiently. The reduced SST-cloud coupling is underlined by the fact that only in the 0.02 m experiment, the SST distribution calculated analogously to Figure 10 is negatively skewed (Appendix Figure A.4). This demonstrates that 700 hPa clouds have a stronger cooling effect in the control experiments and therefore lead to an increase of climate sensitivity in the 0.05 m and 0.02 m experiments. The influence of 700 hPa clouds on shortwave fluxes is also evident in the change of planetary albedo (Figure 18b). While in the control experiments the planetary albedo is smallest in the 0.1 m experiment and increases strongly for smaller MLO depths, it increases in the 4xCO_2 experiments with the onset of the diurnal cycle and stays constant afterwards. Figure 20 illustrates the planetary

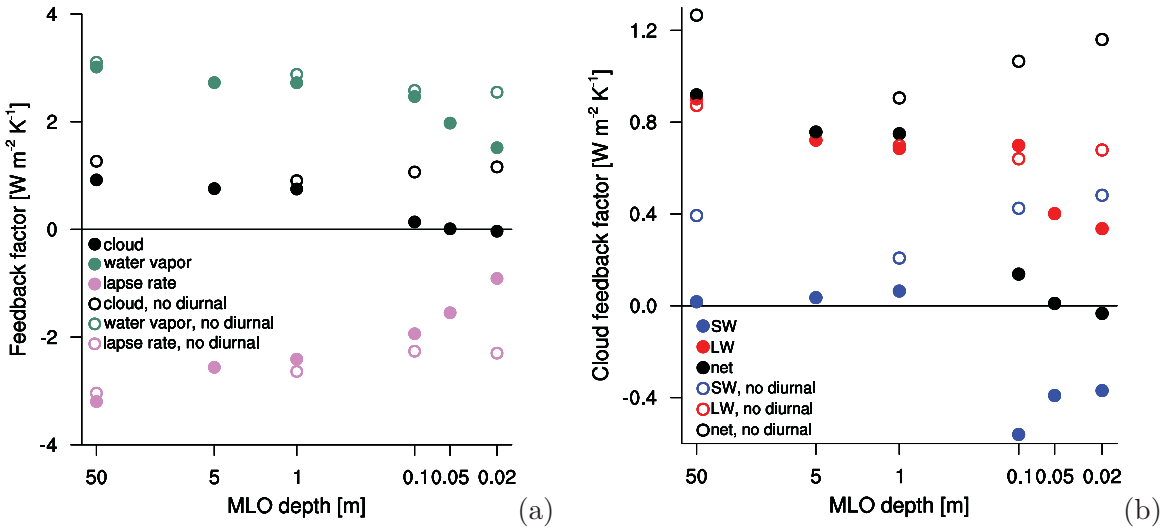

Figure 19: Net water vapor, lapse rate and cloud feedback factor (a) and shortwave and longwave cloud feedback factor (b) for different MLO depths on a logarithmic scale. The experiment series with and without a diurnal cycle are presented both.

albedo in the subsidence and in the upsidence regimes. On the one hand, the strong increase of planetary albedo in the control experiments with MLO depths of less than 0.1 m is caused by changes in the subsidence regime, emphasizing the important role of the 700 hPa clouds. On the other hand, the increase of planetary albedo in the 4xCO_2 experiments with the onset of the diurnal SST cycle is only visible in the upsidence regime. This is related to enhanced triggering of deep convection during the day. Although this effect is also apparent in the control experiments, it is strongest in the 4xCO_2 experiments, signifying a negative shortwave cloud feedback from deep clouds. This feedback may be another reason for the very small ECS in the 0.1 m experiment. Another reason for the increase of planetary albedo in the experiments with a strong diurnal cycle is the slight increase of the upsidence area, as discussed in Section 4.1.2.

Figure 19 also depicts a decrease of the absolute value of lapse rate and water vapor feedback with decreasing MLO depth in the experiments with a diurnal cycle. The reduction is strongest for small MLO depths, while the sum of the two feedbacks stays approximately constant. The reduction of the absolute value of both of these feedbacks can partly be explained with the diurnal cycle of SST (Figure 21). Since nearly all of the convection is initialized during the day in the 0.1 m and 0.02 m experiment, only the maximum temperatures during the day are relevant for the formation of deep convection and for the atmospheric temperature profile, which depends on the moist adiabat. Because of that, it would be more reasonable to scale the lapse rate and water vapor feedback with the daily maximum temperature increase, than with the global mean temperature increase. Figure 21 illustrates that ECS is smaller than the global mean ECS in the afternoon, where surface temperatures maximize (Figure 11). This trend

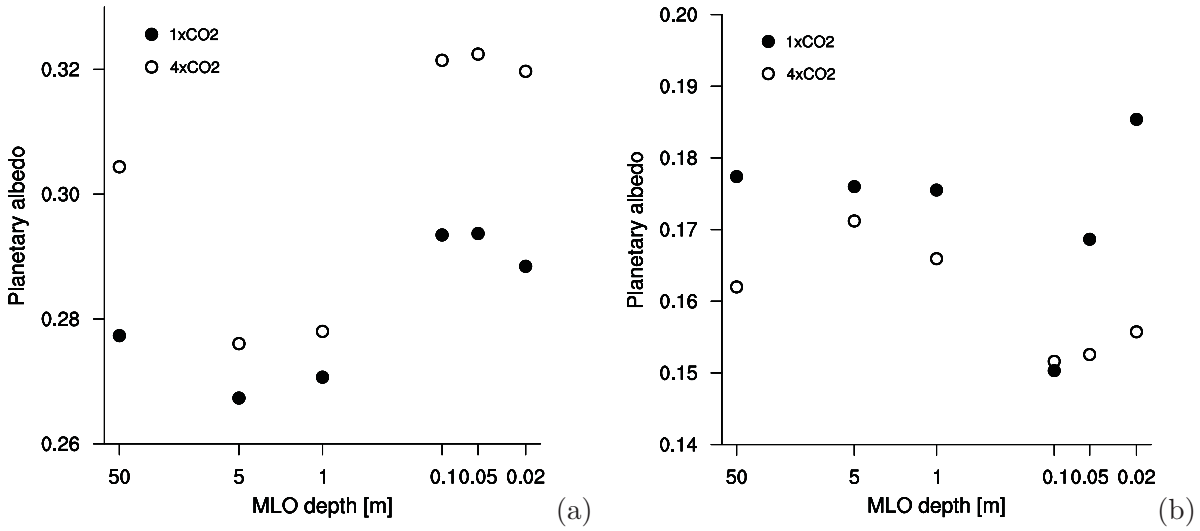

Figure 20: Planetary albedo in the upsidence regime (a) and in the subsidence regime (b) for the experiments with a diurnal cycle and different MLO depths on a logarithmic scale.

increases with decreasing surface heat capacity. That can be explained with more evaporation from a warmer ocean during the day in the 4xCO_2 experiments. Cao et al. (1992) also argue that DTR decreases in a warming climate because surface evaporation increases in particular during the day. As a consequence, if the lapse rate and water vapor feedback factor were weighted with the daily maximum temperature instead of the daily mean temperature, they would not decrease so strongly with decreasing MLO depth.

Another reason why DTR decreases with increasing CO_2 concentrations is that an opaque atmosphere can cool less efficiently at night, while maximum temperatures are coupled to convection and remain approximately constant. This rectification mechanism becomes more important with decreasing MLO depth. However, it is not evident that the high climate sensitivities at night lead to a net increase of climate sensitivity since this might be balanced by small climate sensitivities during the day.

All in all, it can be concluded that in a setup with a diurnal cycle, a reduction of MLO depth results in an increase of climate sensitivity because a strong surface-cloud interaction leads to low SSTs in the control experiments. The increase of climate sensitivity is masked by a one-off drop of shortwave cloud feedback as boundary layer clouds dissipate in the control experiments with a strong diurnal cycle. The strong 700 hPa cloud feedback is probably a model artefact related to the parameterization of convection because 700 hPa clouds are less pronounced in reality. However, in principle a positive cloud feedback caused by a decreased coupling of low clouds to the surface for increased CO_2 concentration is possible in reality as well. The cloud feedback related to the dissipation of boundary layer clouds is also transferable to the earth system. Stratocumulus, for example, is most apparent over cold ocean areas.

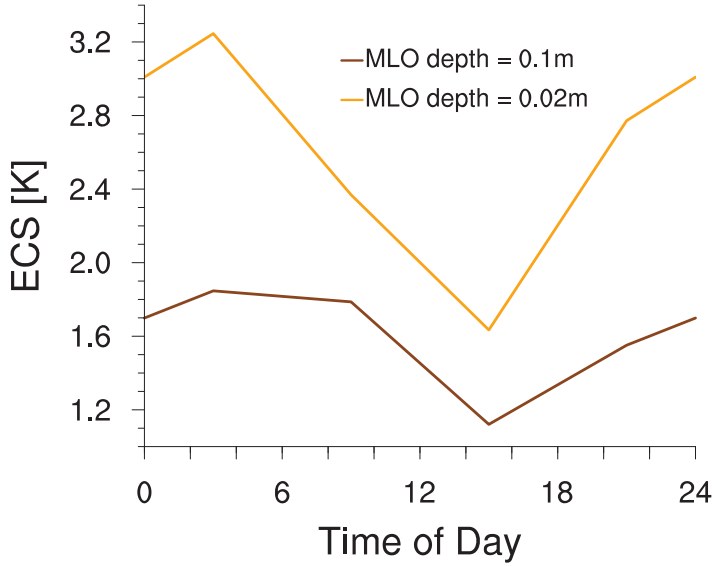

Figure 21: Diurnal cycle of equilibrium climate sensitivity (ECS) for MLO depths of 0.1 m and 0.02 m. The values are averaged over 6 hours, with the data point located at the center of the output interval.

4.2 Dependence of RCE climate on evaporation resistance

After reducing the MLO depth and therefore the heat capacity of the surface, the second step towards a "land-like" planet is the introduction of an artificial evaporation resistance. Thus, evaporation from the ocean becomes harder, so the ocean loses one of its main characteristics. In fact, it is best to think instead of an oily ocean in which the water has to pass a layer of oil in order to be able to evaporate. The definition of the evaporation resistance parameter rsoil and the technical details of its implementation in ECHAM6 are explained in Section 2.2. It can be interpreted as additional evaporation resistance, so for rsoil = 1, evaporation is twice as difficult as before, for rsoil = 3, it is four times as difficult as before and so on and so forth. The soil-moisture feedback is not incorporated in the model because the available water at the surface does not depend on precipitation rates. A change of evaporation rate alters on the one hand the surface energy budget and on the other hand the water supply in the atmosphere. The consequences of these alterations are analyzed in this chapter, focusing on phenomenological characteristics in Section 4.2.1 and on the response to a quadrupling of CO_2 concentrations in Section 4.2.2.

4.2.1 Phenomenology

At the outset of the experiments with enhanced evaporation resistance, it was already expected that the latent heat flux would decrease considerably. Nevertheless, the influence on the surface energy budget and the change of atmospheric processes under drier conditions were

unclear. Besides, it was unknown for which evaporation resistance the surface fluxes would be "land-like", so a definition via the resulting Bowen ratio seems straightforward. The Bowen ratio is the ratio of sensible to latent heat fluxes. On earth, the Bowen ratio strongly depends on water supply. In the MPI-ESM simulations for the Coupled Model Intercomparison Project 5 (CMIP5, Giorgetta et al., 2013), the Bowen ratio is about 1:1 in the tropics over land between 30° N and 30° S. In the humid inner regions between 15° N and 15° S, the Bowen ratio is about 1:2, while in the outer regions of the tropics between 30° N and 15° N, the Bowen ratio is about 2:1. In arid regions like in the Sahara desert, the latent heat flux approaches zero, so the Bowen ratio builds up towards infinity. To summarize, the Bowen ratio is in a wide range in the tropics over land, with a lower limit of about 1:2 in very humid regions and basically no upper limit in arid regions. Consequently, the surface fluxes start to be "land-like" for rsoil = 3, where the Bowen ratio is about 1:3 (Figure 22). For rsoil = 7, the Bowen ratio is approximately the same as the mean value in the tropics over land. The surface fluxes for rsoil $\geqslant$ 15 represent tropical dry regions.

Figure 22 also indicates that the reduction of latent heat flux with increasing evaporation resistance is mainly compensated by a rise of longwave radiation, and only secondary by a rise of sensible heat flux. Assuming that surface wind speeds do not change much, the sensible heat flux can only increase if the temperature difference between the surface and lowest model level increases. The net longwave radiation can increase either due to rising SSTs or due to decreasing longwave back radiation of the atmosphere. The latter strongly depends on the amount of water vapor and cloud water in the atmosphere.

Table 10 shows that the global mean SST increases until it maximizes at rsoil = 15, which is followed by an SST decrease. On the contrary, precipitation decreases all the time, though at first slowly, then with a decrease rate of 50 % for rsoil > 7. Vertically integrated water vapor increases at first slightly before it decreases rapidly for rsoil > 3. The different decrease rates of precipitation and integrated water vapor indicate a dependence on the SST. The obvious reason for the precipitation decrease is of course the external forcing of the increasing evaporation resistance, though from an atmospheric perspective it can be explained with less radiative cooling. Concerning the net outgoing longwave radiation, it can be concluded that for small evaporation resistances, the OLR increases because the emitted longwave radiation from the surface increases due to rising SSTs, while for large evaporation resistances OLR increases because longwave back radiation of the atmosphere decreases resulting from decreasing water vapor concentrations. The latter mechanism allows SSTs to decrease while the OLR increases.

The vertical profiles in Figure 23 illustrate that extensive changes occur in the low troposphere beneath 600 hPa in response to an increase of evaporation resistance. Since latent heat fluxes decrease, the ascending air is drier and has to cool more until it finally saturates at the lifting condensation level (LCL). Hence, the LCL rises and relative humidity decreases below the LCL. Consequently, convective heating decreases beneath the LCL and the temperature lapse

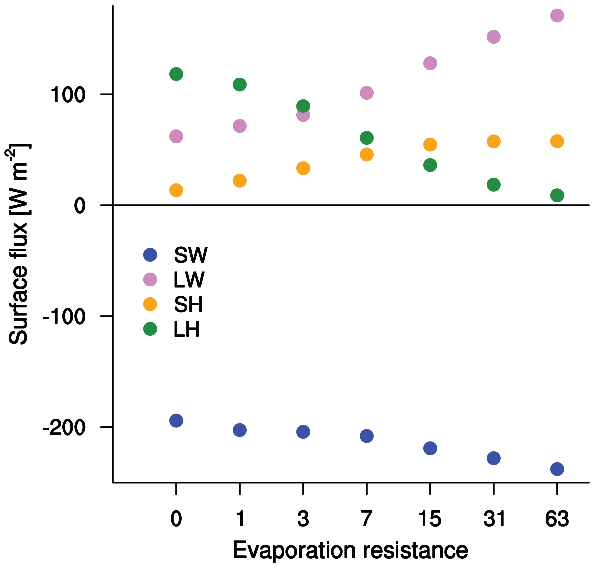

Figure 22: Mean equilibrium surface fluxes for different evaporation resistances. SW and LW denominate the net shortwave and longwave radiation at the surface and SH and LH stand for sensible and latent turbulent heat fluxes. Upward fluxes are defined to be positive.

Evaporation resistance	0	1	3	7	15	31	63
SST [K]	300.1	303.5	306.7	308.5	309.2	308.1	306.7
Precipitation [mm/d]	4.1	3.8	3.1	2.1	1.3	0.6	0.3
vert. int. water vapor [kg m^{-2}]	36.1	40.2	41.3	34.5	24.5	14.5	8.8

Table 10: Mean equilibrium SST, precipitation and vertically integrated water vapor for different evaporation resistances.

rate tends to become dry adiabatic. Besides, this leads to an increase of the effective emission height at which radiation penetrating to the surface is emitted. Thus, the atmosphere cools less, which is one argument for the decrease of precipitation. Above the LCL, the direct influence of increasing evaporation resistance reduces and is only evident in comparatively low temperatures. Because of that, the peak in cloud ice and cloud fraction move downward and tropopause height reduces. The latter accords to the fixed anvil temperature (FAT) hypothesis (Hartmann and Larson, 2002). Since tropopause height reduces, the peak of relative humidity located at the tropopause is also shifted downward. For high evaporation resistances, the bimodal relative humidity profile becomes monomodal because of the strong relative humidity decrease below the LCL. Hence, the boundary layer clouds dissipate rapidly and are gone for rsoil $\geqslant 3$.

Furthermore, it is conspicuous that cloud liquid water strongly decreases until there is no liquid water left, while cloud ice changes only marginally. This can mainly be explained

with the strong decrease of relative humidity in the lower troposphere, where liquid water accumulates, while in the ice cloud regions, relative humidity does not change much.

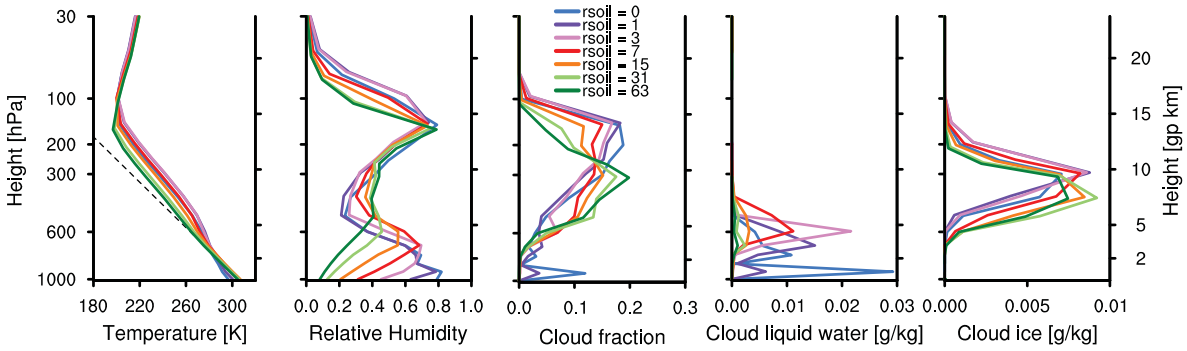

Figure 23: Vertical equilibrium profiles of atmospheric properties for different evaporation resistances. The black dashed line in the temperature profile represents the dry adiabatic lapse rate, starting at the surface temperature of the experiment with rsoil = 63.

Not only the mean properties change with increasing evaporation resistance, but also the horizontal distribution of these properties changes. The random snapshots of monthly mean precipitation and surface wind field in Figure 24 already lead to the assumption that a transition to a single cluster climate occurs, which means that the degree of convective self-aggregation increases. Besides, the cluster seems to be surrounded by an area of weak winds for rsoil > 7, which means that the surface wind field does not converge at the center of the cluster anymore, but at the borders of the weak wind area. However, random snapshots are not statistically significant. Because of that, the precipitation maximum is detected for each time step and the properties are sampled along the longitude of maximum precipitation, closing the cycle with the longitude on the other side of the planet and moving the grid point with maximum precipitation to the center. The resulting distributions of precipitation, vertically integrated water vapor, SST and surface pressure are presented in Figure 25, while the vertical profiles of potential temperature along this cycle are depicted together with the wind field in Figure 26. For all these images, the representativeness is increased by averaging the data points with the same longitudinal distance to the maximum value. This is possible because the RCE version of ECHAM is isotropic because of the homogeneous boundary conditions in ECHAM-RCE. Furthermore, the represented area depends on the distance to P_{max}, maximizing at a distance of 90 ° to P_{max}.

The change of circulation towards one single cluster reveals itself in the strong reduction of precipitation for rsoil $\geqslant 3$ in areas that are located more than 90° south or north of the grid point with maximum precipitation (Figure 25a). The overturning circulation strengthens for rsoil $\geqslant 3$ (Figure 26). This suggests that for rsoil $\leqslant 1$, there are many other clusters that weaken the individual overturning circulation of the cluster with strongest precipitation, while

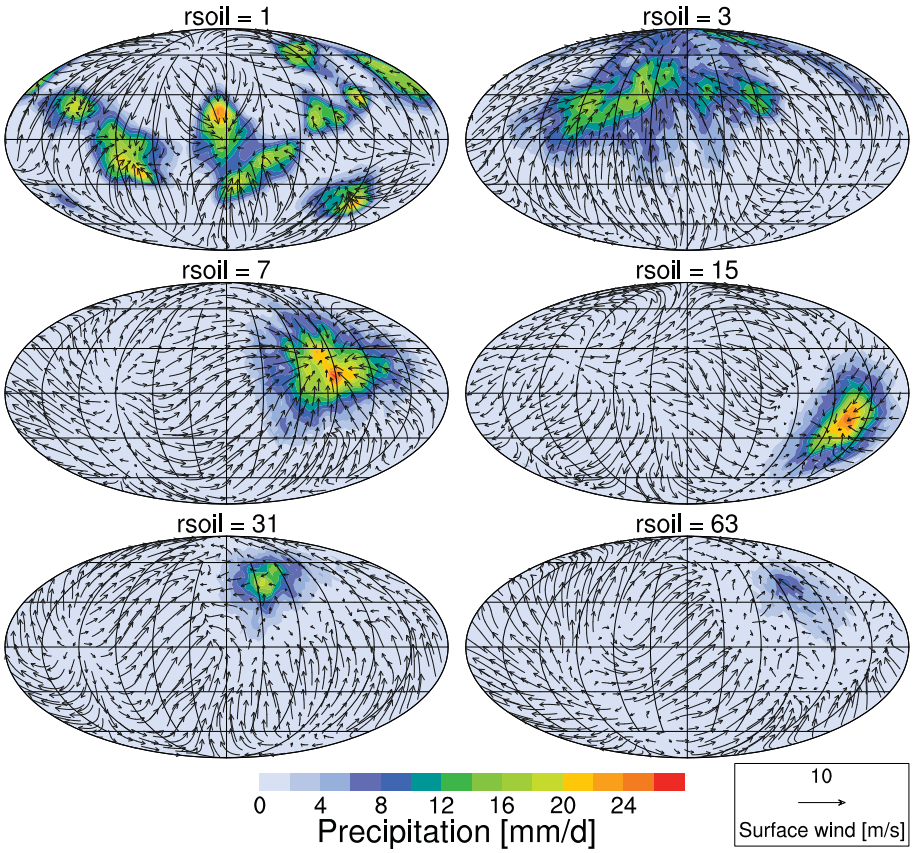

Figure 24: Random snapshots of monthly mean precipitation and surface wind field for evaporation resistance values of 1, 3, 7, 15, 31 and 63.

for rsoil $\geqslant 3$, there is only one area with strong upsidence, which is balanced by subsidence everywhere else. The strengthening of the overturning circulation for rsoil $\geqslant 3$ is also apparent in the vertical cross section of the wind field in Figure 26. One consequence of the transition to the single cluster climate is, that for rsoil $= 7$ the precipitation maximum is higher than for rsoil $= 0$, although the global mean precipitation has approximately halved due to enhanced evaporation resistance. Convective aggregation could also be the reason for the rapid decrease of water vapor in the atmosphere for rsoil $\geqslant 3$. In cases with aggregated deep convection, Tobin et al. (2012) found a drier mid and upper troposphere in the convection-free environment when using several satellite datasets and reanalysis. Figure 25b shows that the difference of vertically integrated water vapor in the convective and non-convective area increases, if convection aggregates. Hence, a drying of the convection-free environment is also evident in RCE. It can be explained with more efficient precipitation within the convective cluster because more of the condensed water falls out as rain and less is detrained to the environment (Khairoutdinov and Emanuel, 2010).

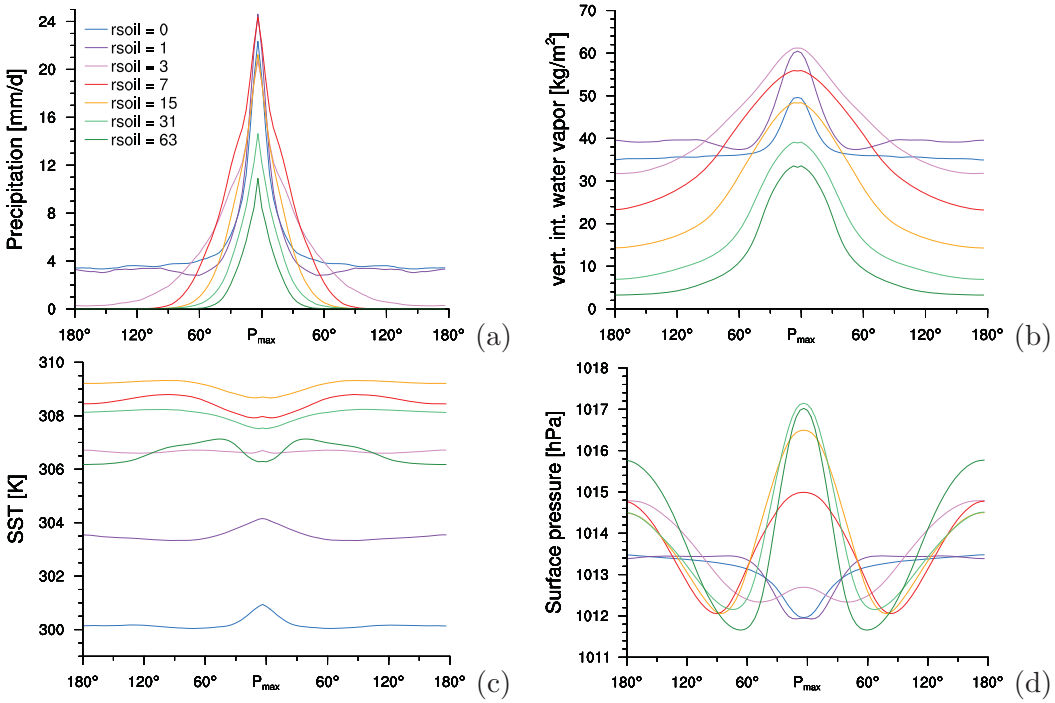

Figure 25: Precipitation (a), vertically integrated water vapor (b), SST (c) and surface pressure (d) sampled along the longitude of maximum precipitation for different evaporation resistances. The cycle is closed with the longitude on the other side of the planet and the grid point with maximum precipitation is moved to the center. The data is averaged over all time steps in equilibrium. Representativeness is increased by averaging the data points with the same longitudinal distance to the maximum value.

An important task is to specify the circumstances in which self-aggregation occurs. Muller and Held (2012) find an upgradient horizontal transport of moist static energy (MSE) with self-aggregation. However, Figure 27 does not suggest that an upgradient transport of moist static energy occurs for any evaporation resistance. Nevertheless, it is possible that convection aggregates because eddies ensure an upgradient horizontal transport of MSE. But more probable is that in these experiments radiative cooling plays a key-role for self-aggregation. In general, high clouds warm the atmosphere and low clouds cool the atmosphere. One reason is that high clouds are colder and hence emit less longwave radiation. Since low clouds strongly decrease with increasing evaporation resistance, the net cloud radiative effect of the atmosphere, $\mathrm{CRE_{atm}}$, increases. Figure 28 shows that $\mathrm{CRE_{atm}}$ increases for rsoil $\leqslant 3$ from 7 to 17 $\mathrm{W\,m^{-2}}$ because of changes in longwave radiation. Consequently, the cloud radiative effect acts as a source of MSE in convectively active atmospheric regions relative to clear sky areas. Hence, there are good reasons why the increase of $\mathrm{CRE_{atm}}$ is the most important trigger of self-aggregation in these experiments. Nonetheless, some additional experiments will be necessary in order to prove this theory. The atmospheric warming due to the increase

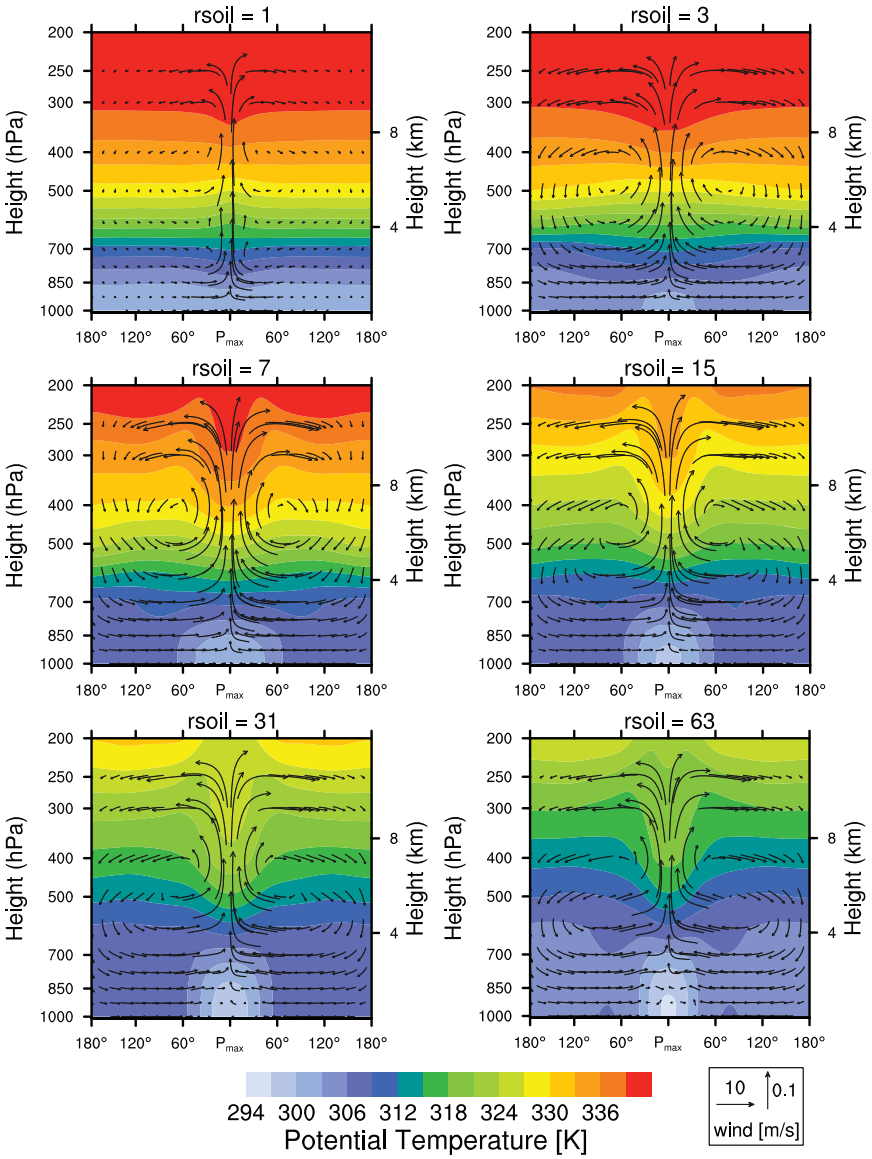

Figure 26: Vertical cross sections of mean potential temperature and wind field for evaporation resistance values of 1, 3, 7, 15, 31 and 63. Like in Figure 25, the cross sections are centered at the location with the highest monthly mean precipitation and show the vertical profiles along that longitude, closing the cycle with the longitude on the other side of the planet. The vertical velocity is scaled with a factor of 100. The data is averaged over all time steps in equilibrium.

of $\mathrm{CRE_{atm}}$ also leads to a decrease of precipitation since precipitation balances atmospheric cooling. A hypothesis of Khairoutdinov and Emanuel (2010) is that self-aggregation is mostly dependent on SST. They find self-aggregation with a full-physics CRM if the fixed SST is larger than 297 K. However, the SST is for all evaporation resistances higher than 297 K, which

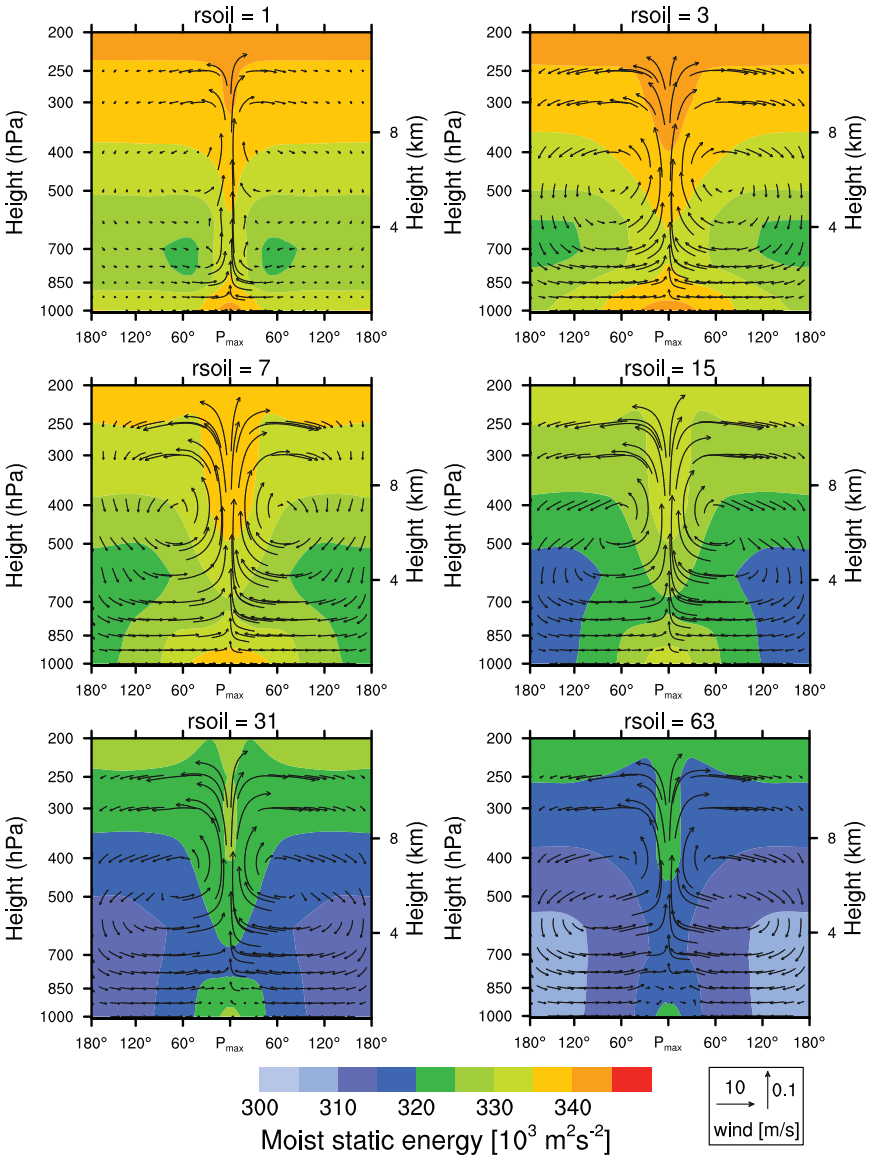

Figure 27: Vertical cross sections of mean moist static energy and wind field for evaporation resistance values of 1, 3, 7, 15, 31 and 63. The data is averaged analogously to Figure 26.

indicates that this is not the dominant mechanism. Nevertheless, it would be interesting to know whether convection would aggregate for rsoil $\geqslant 3$ without the strong SST increase. Besides, an important question is whether hysteresis is possible in these experiments. The evaporation resistance experiments were initialized with the experiment with the next smaller evaporation resistance. To make sure that the only reason for an unaggregated climate for rsoil $\leqslant 1$ is not that it is initialized in an unaggregated state, the experiment with rsoil $= 0$ is repeated with rsoil $= 7$ as initialization. The single cluster breaks up quite rapidly, so at least in this case no hysteresis is evident.

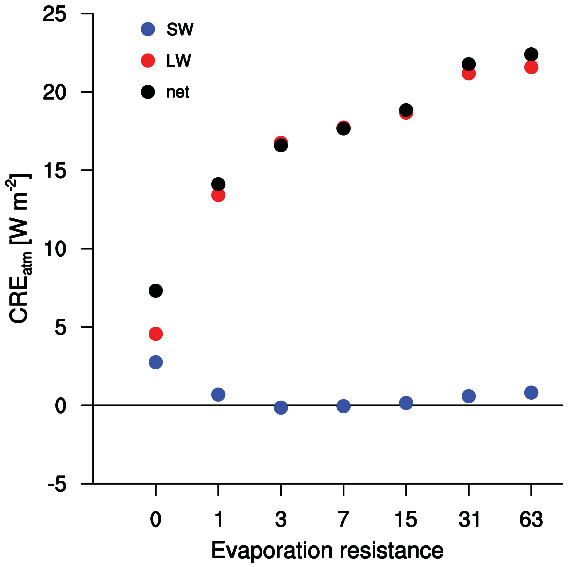

Figure 28: Shortwave (SW), longwave (LW) and net cloud radiative effect of the atmosphere ($\mathrm{CRE_{atm}}$) for different evaporation resistances. Positive values indicate that the atmosphere receives energy.

Figure 26 also shows that especially in the upper part of the updraft, the potential temperature is higher than in other regions on the same level due to convective heating. The strength of this signal is interesting because one would expect that internal gravity waves smooth out any perturbation rather instantaneously like in Figure 14, especially in the upper troposphere where the influence of friction is small.

As a consequence of the small amount of water vapor in the low troposphere, some of the rain falling through this dry air evaporates, moistening and cooling these layers. This effect is known as virga. The temperature decrease in the affected areas is apparent in Figure 26. The temperature decrease in the low troposphere also affects surface temperatures. For rsoil $\geqslant 7$, there is a local SST minimum at the location of maximum precipitation (Figure 25c). Because of the cold pool, the surface wind field does not converge anymore at the center of the precipitation cluster, but at the edges of the cold pool. This change of dynamics is reflected in the change of surface pressure (Figure 25d). In the experiments without a cold pool, the pressure minimum is in the center of the cluster. This is because the rising air masses drive the circulation, leading to surface convergence and upper-tropospheric divergence. As there is less friction in the upper troposphere, the upper-tropospheric divergence is more efficient than the convergence at the surface, leading to low surface pressure. This changes with increasing evaporation resistance because convergence does not occur anymore at the surface, but above the cold pool. Further, the cold air in the virga region has a high density, leading to a pressure maximum at the location of maximum precipitation. The pressure minimum is shifted to the edge of the cold pool, which is the new location of surface convergence.

The strong virga effect also feeds the assumption that most of the precipitation does not reach the surface. This implies that the main source of atmospheric humidity is not the surface, but the layers in which the rain evaporates. This is another reason why the surface wind does not converge at the center of the cluster anymore.

Another interesting side effect is that for all evaporation resistances, the convective clusters move over all of the sphere, always trying to get to the location with the highest surface temperature. This changes for rsoil = 63 because the precipitation cluster gets so small that, on average, the location of highest surface temperature is only in 40 ° distance to the maximum precipitation area, while the surface convergence, which marks the edge of the convective area, occurs on average in 60 ° distance (Figure 25). So on the one hand, there are always warm areas within the convective area where the cluster can move to, on the other hand, the strong winds from the subsidence regions inhibit a movement of the precipitation cluster over the edge of the convective area. Besides, the location of maximum surface temperature does not play a key role for high evaporation resistances anymore as most of the precipitable water in the atmosphere is not gained by evaporation from the surface, but from virga. For all these reasons, the location of the edge of the convective area is stationary for rsoil = 63.

4.2.2 Climate sensitivity regarding evaporation resistance

The influence of evaporation resistance on climate sensitivity is investigated with another experiment series, in which the experiments are repeated with quadrupled CO_2 concentrations. Table 11 gives an overview of the resulting climate sensitivities. In contrast to the MLO depth experiments, the energy leakage is not in all 4xCO_2 experiments stronger than in the control experiments. For rsoil $\geqslant$ 15, there is an energy source instead of a leakage and for rsoil $\geqslant$ 31, the difference in atmospheric energy imbalance of the 4xCO_2 and control experiment ΔR is positive. Hence, in this case, the revised climate sensitivity is smaller than before. Because of these strong transitions, the effect of energy sources or sinks in the atmosphere on climate sensitivity needs to be considered in order to ensure comparability.

The revised climate sensitivity can be calculated by dividing ΔR by the total feedback factor λ:

$$\Delta T_{2\mathrm{xCO_2,revised}} = \Delta T_{2\mathrm{xCO_2}} + \frac{\Delta R}{2\lambda}. \tag{13}$$

ΔR is divided by 2 because it is the difference of energy leakage of the experiments with quadrupled and preindustrial CO_2 concentrations. In this case, λ is calculated with the CO_2 forcing F, which was calculated with the PRP module (Mauritsen et al., 2013):

$$\lambda = \frac{F}{\Delta T_{4\mathrm{xCO_2}}}. \tag{14}$$

Evaporation resistance	0	1	3	7	15	31	63
SST_{ctrl} [K]	300.1	303.5	306.7	308.5	309.2	308.1	306.7
SST_{4xCO_2} [K]	304.5	307.5	309.8	313.8	316.6	314.2	311.3
ΔT_{2xCO_2} [K]	2.2	2.0	1.6	2.7	3.7	3.0	2.3
ΔR [W m^{-2}]	-0.9	-0.8	-0.6	-0.5	-0.6	0.3	0.3
λ [W m^{-2} K^{-1}]	-1.2	-1.4	-1.8	-1.1	-0.8	-1.0	-1.5
$\Delta T_{2xCO_2,revised}$ [K]	2.6	2.3	1.7	2.9	4.1	2.9	2.2

Table 11: Equilibrium global mean SST and climate sensitivity for different evaporation resistances. SST_{ctrl} and SST_{4xCO_2} denote surface temperatures with preindustrial and quadrupled CO_2 concentrations and ΔT_{2xCO_2} is the climate sensitivity calculated according to Equation 12. ΔR is the difference in atmospheric energy imbalance of the 4xCO_2 and control experiment and λ is the total feedback factor. $\Delta T_{2xCO_2,revised}$ is the climate sensitivity with consideration of the contribution of energy leakage, calculated according to Equation 13.

Independent of whether or not the energy leakage is considered in ECS, there is a clear trend. Up to rsoil = 3, the ECS decreases, then it strongly increases up to rsoil = 15, which is followed by a strong decrease for very dry climates (Figure 29b). The water vapor, lapse rate and cloud feedback factors, which were calculated with the PRP module (Mauritsen et al., 2013), all show an overall decrease of magnitude with increasing evaporation resistance (Figure 29c). This is not surprising since all of these feedback factors depend in some way on the amount of water vapor in the atmosphere. The ratio of integrated water vapor increase to temperature increase in the 4xCO_2 experiments maximizes for rsoil = 1 and decreases strongly afterwards. The water vapor feedback shows the same behavior.

The decrease of climate sensitivity up to a minimum ECS at rsoil = 3 can mainly be associated with a decrease in cloud feedback, as the changes in water vapor and lapse rate feedback approximately balance each other. Figure 29d shows that from rsoil = 0 to rsoil = 1, the reduction of cloud feedback is due to a reduction of shortwave cloud feedback. This reduction can be associated with boundary layer clouds, which induce a positive cloud feedback for rsoil = 0, while they are gone in all other control experiments with increased evaporation resistance. The further reduction of cloud feedback from rsoil = 1 to rsoil = 3 can be linked to a reduction of longwave cloud feedback and to the transition to a single cluster climate. Figure 30 illustrates for rsoil = 1 that the fraction of deep clouds over the cluster with maximum precipitation increases strongly when quadrupling CO_2 concentrations, leading to a strong longwave cloud feedback. This can be explained with a transition to a single cluster climate in the 4xCO_2 experiment, which is why the vertical wind profiles in Figure 30 show an increase of overturning circulation. For rsoil = 3, no cloud cover changes are evident apart from a small increase of cloud fraction in 100 hPa, which can be related to a slight increase of tropopause height. Although the transition to a single cluster climate already occurred in the control experiment, the cluster's structure is still a little bit scattered leading to some precipitation

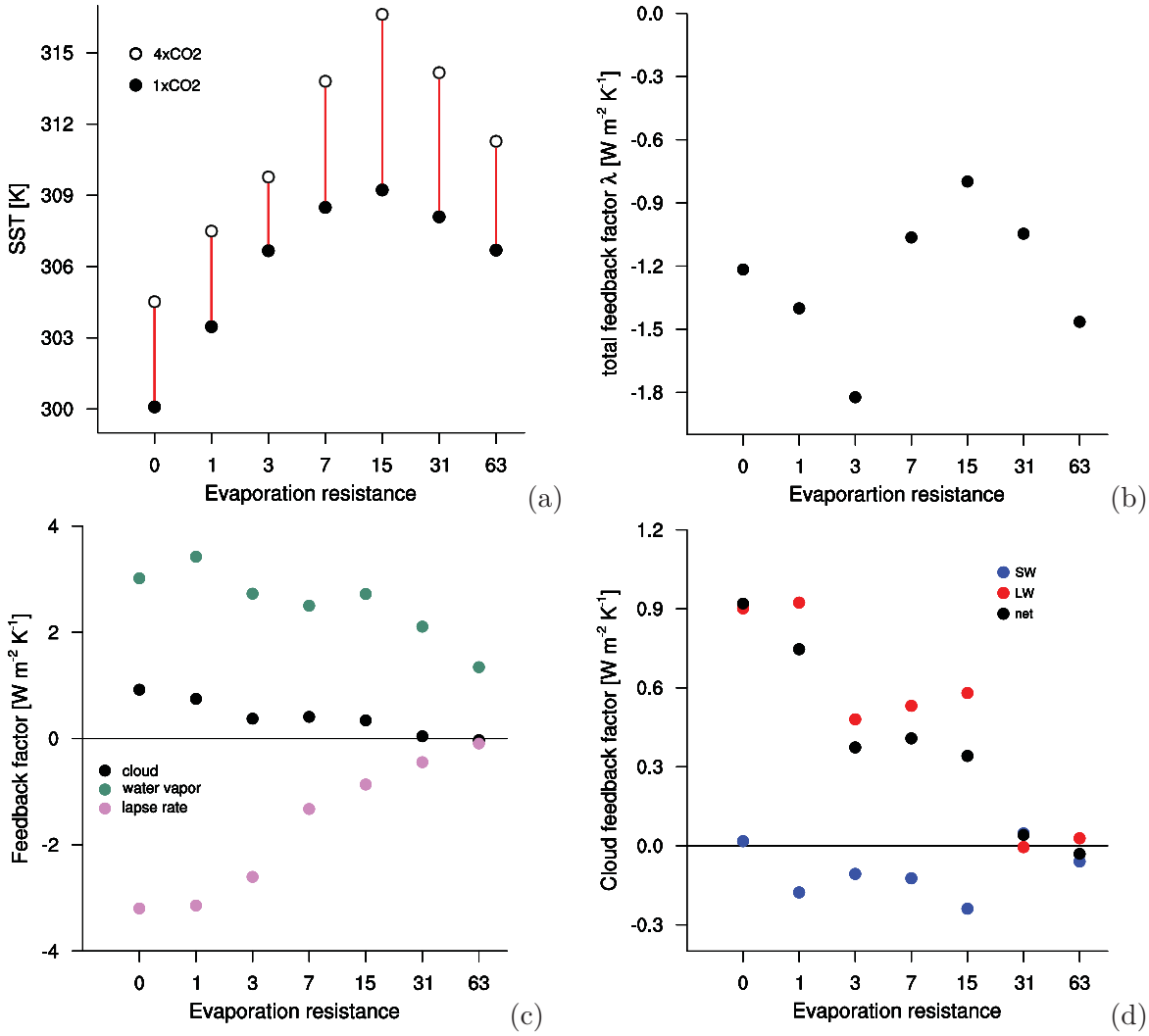

Figure 29: Equilibrium mean SSTs of the experiments with preindustrial and quadrupled CO_2 concentrations (a), the total feedback factor λ (b), the contribution of the net feedback factors (c) and the distribution of the cloud feedback factor in shortwave and longwave feedback factors (d) for different evaporation resistances. The red line between the 1xCO_2 and 4xCO_2 SST visualizes the climate sensitivity.

far away from the cluster (Figure 25a). With quadrupled CO_2 concentrations, the deep clouds are centered more in one location, which is why their radiative impact reduces.

The strong increase of ECS from rsoil = 3 to rsoil = 15 can be related to a strong decrease of the negative lapse rate feedback, while the water vapor feedback does not change much (Figure 29c). The decrease of lapse rate feedback can be associated with a reduction of relative humidity. As a result, the atmosphere is less often saturated and the global mean lapse rate is closer to the dry adiabat. As the dry adiabat does not depend on temperature, unlike the moist adiabat, the lapse rate changes less when quadrupling CO_2 concentrations. Joshi et al.

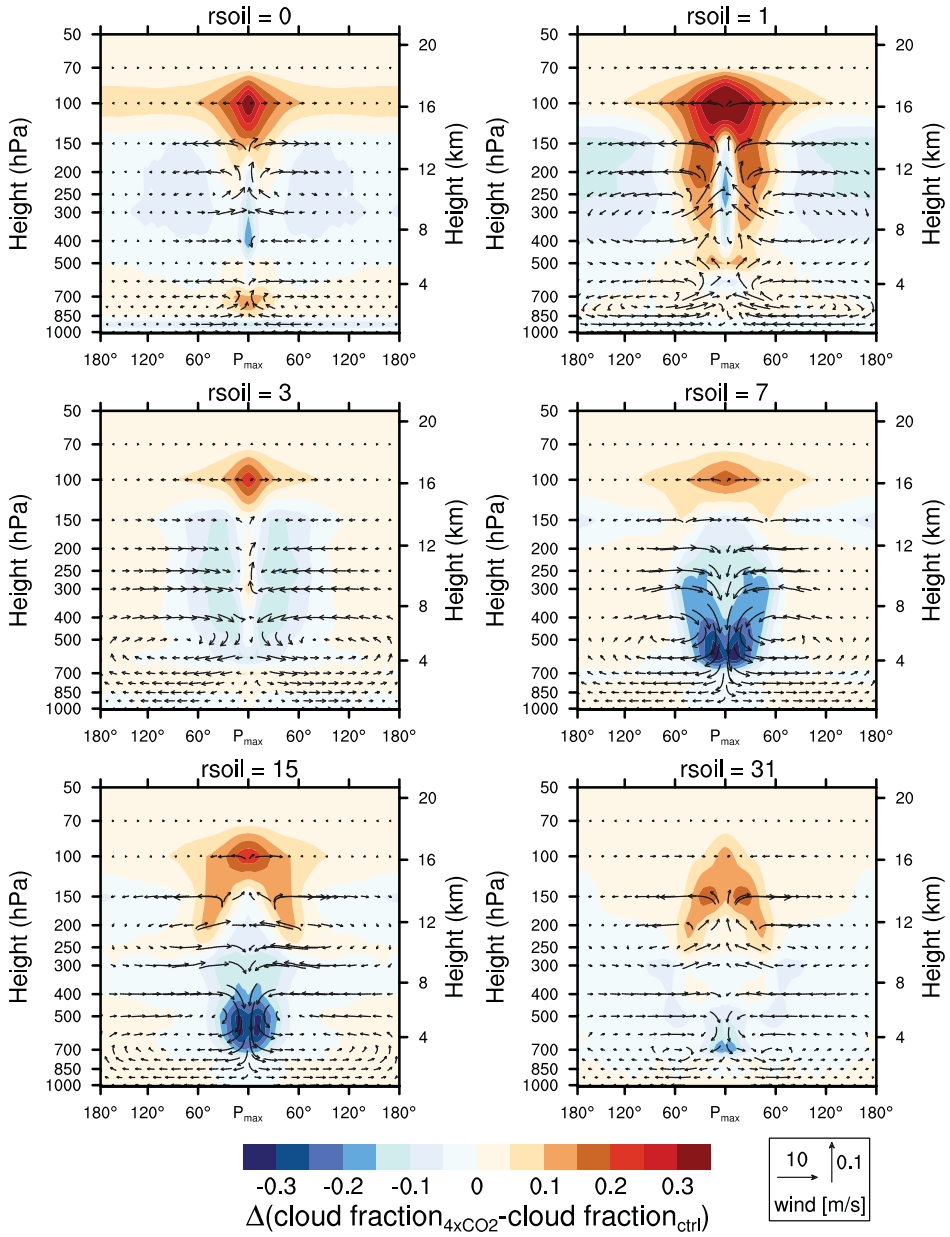

Figure 30: Vertical cross sections of the change of cloud fraction and wind field when quadrupling CO_2 concentrations for evaporation resistance values of 0, 1, 3, 7, 15 and 31. The data is averaged analogously to Figure 26.

(2008) identified this mechanism as the main mechanism that amplifies CO_2 induced warming over land.

For evaporation resistances between rsoil = 3 and rsoil = 15, the water vapor feedback does in contrast to the lapse rate feedback not decrease because the decrease of relative humidity is compensated by a temperature increase, especially in the troposphere below 600 hPa (Figure 23

and Figure A.6 in the Appendix). After the reduction of atmosphere's longwave opaqueness to a critical value, the energy balance at the surface does not have to be sustained by increasing SSTs anymore, but can be sustained by more effective longwave emission from the surface. This does not only lead to decreasing SSTs for rsoil $\geqslant 15$, but also to a strong decrease of water vapor feedback, as the atmosphere now dries and cools at the same time. Because of that, the decrease of water vapor feedback dominates the decrease of lapse rate feedback, leading to a reduction of ECS for rsoil $\geqslant 15$. In addition, the climate sensitivity drops because the longwave cloud feedback reduces. Figure 30 shows that this is related to deep cloud fraction increasing less in the 150 hPa layer instead of the 100 hPa layer. Hence, these clouds are somewhat warmer and have a smaller impact on longwave radiation.

Applied to the real tropics, these results suggest that the land-sea warming contrast might be most amplified in semi-arid regions with Bowen ratios of approximately 2:1, where the air is rarely satisfied with water vapor, but where the amount of water vapor in the atmosphere still suffices for a strong water vapor feedback. However, it is important to remember that a semi-arid climate is not possible in the RCE setup because the definition requires precipitation below potential evapotranspiration. Potential evapotranspiration is equal to evaporation in the RCE setup since the water reservoir is infinite. In equilibrium RCE climate, evaporation and precipitation have to balance each other. Hence, RCE climate with rsoil = 15 resembles a semi-arid climate only in certain aspects, for example concerning the Bowen ratio.

4.3 Combined effect of reduced MLO depth and enhanced evaporation resistance

Major daily variations of SSTs due to a strong decrease of MLO depth can alter atmospheric processes (Section 4.1). These changes might strongly depend on the atmospheric structure. Consequently, the probability is quite high that the influence of the diurnal cycle on atmospheric processes changes non-linearly if it is combined with increasing evaporation resistances (Section 4.2). Hence, experiments with increasing evaporation resistance and with an MLO depth of 0.1 m are analyzed in this section. At an MLO depth of 0.1 m, the diurnal cycle of surface temperature is comparable to the diurnal cycle in the tropics over land. Attempts to combine a 0.02 m deep MLO with increasing evaporation resistance failed because these experiments turned out to be quite unstable due to high wind speeds in the highest model levels, especially for high evaporation resistances. For an MLO depth of 0.1 m, only the experiments with rsoil $\geqslant 31$ and quadrupled CO_2 concentrations are unstable. For rsoil = 63, at least the experiment with doubled CO_2 concentrations is stable.

4.3.1 Phenomenology

The comparison of Table 10 and Table 12 reveals that the general qualitative development of equilibrium mean SSTs with increasing evaporation resistance is almost independent of MLO depth. In both experiments, the SST reaches a maximum value at rsoil = 15. For larger evaporation resistances, the atmosphere is dry enough to decrease longwave back radiation of the atmosphere substantially, which results in a significant SST drop. However, the equilibrium mean SSTs differ quantitatively. With an MLO depth of 0.1 m, the SST increases more strongly, resulting in a maximum value which is 3.8 K higher than with an MLO depth of 50 m.

Evaporation resistance	0	1	3	7	15	31	63
SST [K]	301.3	303.9	308.1	311.2	313.0	307.9	305.0
Precipitation [mm/d]	4.4	3.7	3.1	2.3	1.5	0.6	0.3
vert. int. water vapor [kg m^{-2}]	46.5	45.8	50.4	48.6	44.0	20.9	11.4

Table 12: Mean equilibrium SST, precipitation and vertically integrated water vapor of the experiments with an MLO depth of 0.1 m and different evaporation resistances.

The global mean surface fluxes with an MLO depth of 0.1 m (Figure 31) are nearly indistinguishable from the surface fluxes with an MLO depth of 50 m (Figure 22). A small difference is that for rsoil $\leqslant 7$, the sensible heat flux increases more strongly than the net longwave radiation. This is an indirect consequence of the diurnal SST amplitude because the turbulent heat fluxes are triggered during the day. Besides, the amplification of evaporation during the day leads on average to more water vapor in the atmosphere (Table 12), which inhibits an effective radiative cooling of the surface. This is the reason why the surface warms more than in the experiments with a 50 m deep slab ocean. The SST increase in turn influences the sensible heat flux because the mean temperature difference between surface and lowest model level increases, resulting in an increase of sensible heat flux. For rsoil > 15, the SST drop leads to a reduction of sensible heat flux, although the latent heat flux further declines.

Like the surface fluxes, the equilibrium mean vertical atmospheric profiles seem to be nearly independent of MLO depth when increasing evaporation resistance (Figure 23 and Figure 32). Both for an MLO depth of 50 m and 0.1 m, the relative humidity decreases mainly in the lower troposphere beneath 600 hPa, the upper tropospheric peak of relative humidity and cloud fraction is shifted downward and the tropopause height reduces, while the lapse rate tends to become dry adiabatic for large evaporation resistances. Besides, cloud liquid water reduces strongly while cloud ice does not decrease, but is shifted downward. The only striking difference is that there are no boundary layer clouds in any of the experiments with 0.1 m MLO depth because of the diurnal SST amplitude, as explained in Section 4.1.2. Another difference is that the gap between the profiles for rsoil $\geqslant 31$ and the other profiles widens, illustrating a strong climate transition as the thermal optical depth of the atmosphere decreases.

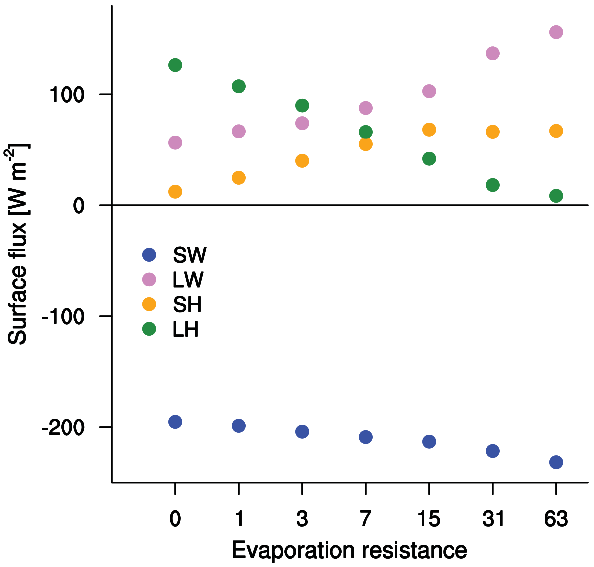

Figure 31: Mean equilibrium surface fluxes of the experiments with an MLO depth of 0.1 m and different evaporation resistances. SW and LW denominate the net shortwave and longwave radiation at the surface and SH and LH stand for sensible and latent turbulent heat fluxes. Upward fluxes are defined to be positive.

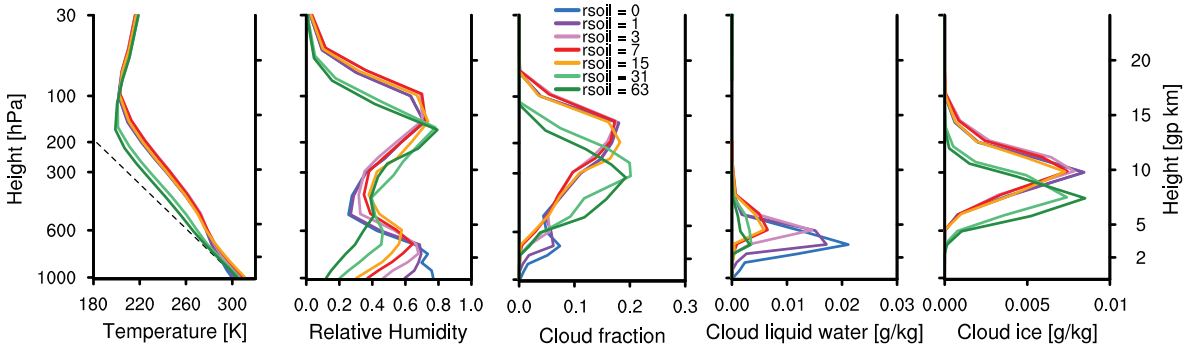

Figure 32: Vertical equilibrium profiles of atmospheric properties in the experiments with an MLO depth of 0.1 m and different evaporation resistances. The black dashed line in the temperature profile represents the dry adiabatic lapse rate, starting at the surface temperature of the experiment with rsoil = 63.

Some properties which obviously depend on evaporation resistance as well as MLO depth are the diurnal surface temperatures and water related properties like precipitation and evaporation. With increasing evaporation resistance, the SST amplitude increases from 11 K to 18 K because on the one hand, the air is drier and the surface can cool more efficiently at night and warm during the day due to solar insolation, and on the other hand, there is less evaporation which otherwise would cool the surface particularly in the afternoon (Figure 33). Consequently, SSTs increase relatively to the 50 m experiments most strongly in the afternoon.

The decrease of evaporation in the afternoon is also the reason for an increase of evening temperatures relative to morning temperatures. Hence, evening precipitation increases slightly compared to morning precipitation since the atmosphere is less stratified in comparison to smaller evaporation resistances.

Nevertheless, precipitation peaks in all experiments in the afternoon although daily mean precipitation decreases strongly with increasing evaporation resistance. Concerning the timing of precipitation, it is interesting that there is more precipitation than evaporation in the morning (Figure 33). This shows that the most important trigger of precipitation is not supersaturation due to a strong latent heat flux at the surface, but an increase of surface temperatures, which trigger convection because CIN is compensated. In the afternoon, precipitation further increases because the maximum surface temperatures trigger even more convection. In addition, the latent heat flux maximizes in the afternoon.

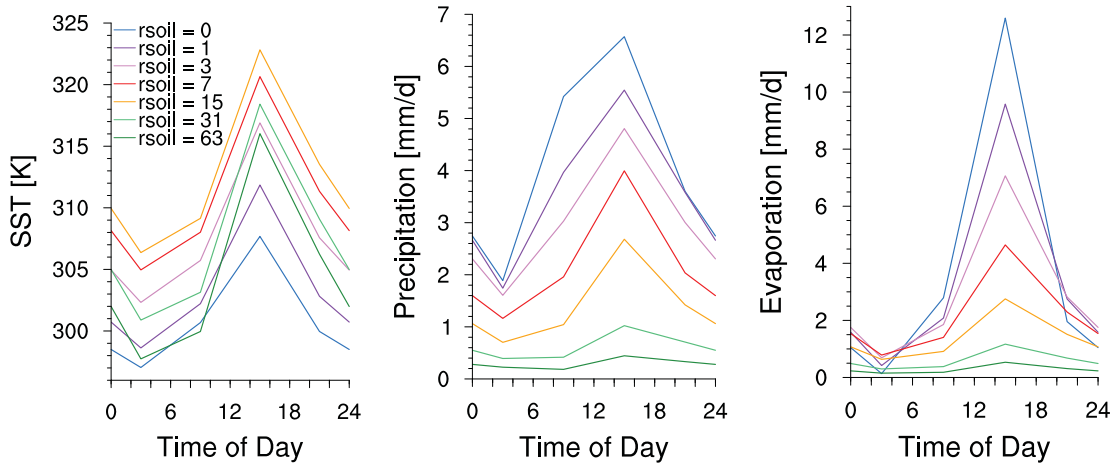

Figure 33: Diurnal cycle of temperature, precipitation and evaporation for different evaporation resistances and an MLO depth of 0.1 m. The values are averaged over 6 hours, with the data point located at the center of the output interval.

The transition to a climate state with only one cloud cluster occurs for rsoil = 3 (Figure 34a), hence self-aggregation seems to be independent of the MLO depth because the transition occurs in the experiments with an MLO depth of 50 m also for rsoil = 3 (Figure 25a). Nonetheless, there are some differences regarding the single cluster climates. First of all, the convective area of the single cluster is larger, resulting in a broader distribution of precipitation and vertically integrated water vapor (Figure 34). This can be explained with increased SST perturbations. Especially at the edges of the convective area, the SST is very high. As a result, convection is triggered in this region and broadens the distribution of precipitation and water vapor. Figure A.8 in the Appendix also illustrates in comparison to Figure 26 that within the convective region, the area with upward motion increases. Consistently, the cold pool beyond the cluster also increases in size. Because convection is triggered through high surface

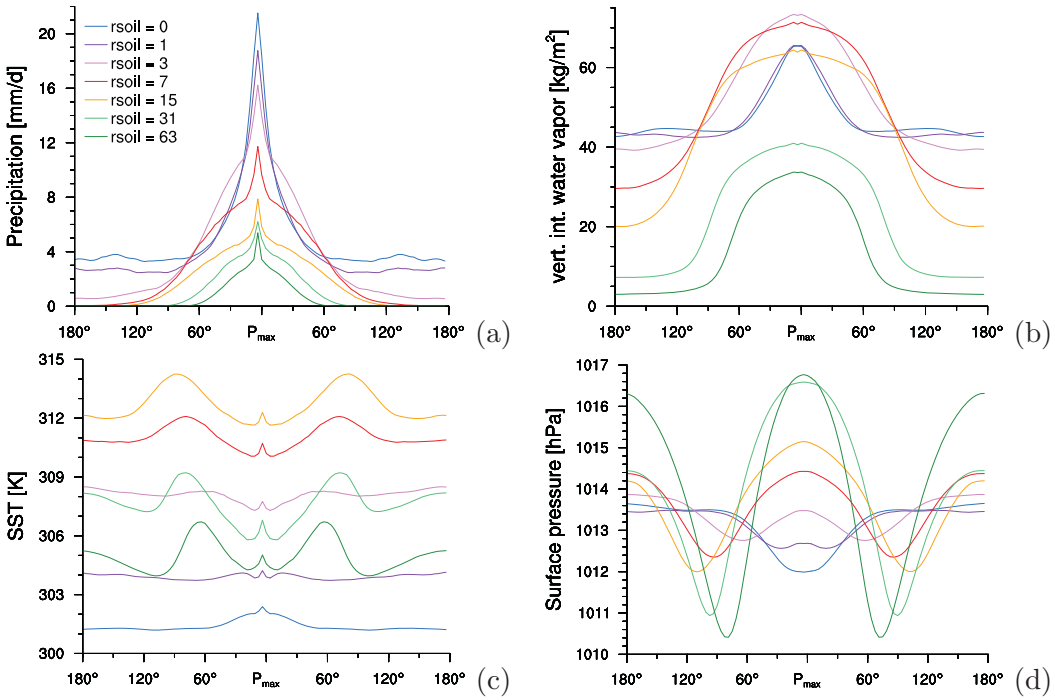

Figure 34: Precipitation (a), vertically integrated water vapor (b), SST (c) and surface pressure (d) sampled along the longitude of maximum precipitation for an MLO depth of 0.1 m and different evaporation resistances. The data is averaged analogously to Figure 25.

temperatures more often, the potential temperature increases more strongly with height. This is equivalent to a decrease of lapse rate depicted in Figure 32, especially for rsoil $\leqslant$ 15.

4.3.2 Climate sensitivity regarding the combined effect of reduced MLO depth and enhanced evaporation resistance

In principal, the dependency of climate sensitivity on evaporation resistance does not change when decreasing the MLO depth from 50 m to 0.1 m (Table 13). In both experiment series, the climate sensitivity first decreases for rsoil $\leqslant 3$, then increases strongly for rsoil $\leqslant 15$ and then decreases again. A point to notice here is that for rsoil $\geqslant 31$, the experiments with quadrupled CO_2 concentrations are unstable because the single cluster breaks up. Simultaneously, the water vapor concentration in the atmosphere strongly increases and the surface temperature increases rapidly until a threshold value is exceeded and the model run terminates. Whether the single cluster breaks up because the system becomes unstable or whether the system becomes unstable because the single cluster breaks up is difficult to distinguish. The only indication how climate sensitivity changes for rsoil $\geqslant 31$ gives the experiment with doubled CO_2 concentrations and rsoil = 63.

Evaporation resistance	0	1	3	7	15	63
SST_{ctrl} [K]	301.3	303.9	308.1	311.2	313.0	305.0
SST_{4xCO_2} [K]	304.5	306.7	310.6	314.9	322.2	307.2 [1]
ΔT_{2xCO_2} [K]	1.6	1.4	1.2	1.8	4.6	2.2
ΔR [$W\,m^{-2}$]	-0.5	-0.5	-0.4	-0.4	-0.8	0.1 [1]
λ [$W\,m^{-2}\,K^{-1}$]	-1.7	-2.0	-2.3	-1.6	-0.7	-1.3
$\Delta T_{2xCO_2,revised}$ [K]	1.7	1.5	1.3	1.9	5.2	2.1

Table 13: Equilibrium global mean SST and climate sensitivity for different evaporation resistances and an MLO depth of 0.1 m. SST_{ctrl} and SST_{4xCO_2} denote surface temperatures with preindustrial and quadrupled CO_2 concentrations and ΔT_{2xCO_2} is the climate sensitivity calculated according to Equation 12. ΔR is the difference in atmospheric energy imbalance of the 4xCO_2 and control experiment and λ is the total feedback factor. $\Delta T_{2xCO_2,revised}$ is the climate sensitivity with consideration of the contribution of energy leakage, calculated according to Equation 13.
[1] These values account to a doubling of CO_2 concentrations.

Although the general tendencies of climate sensitivity are the same for both MLO depths when increasing evaporation resistance, an important difference is that the tendencies are stronger in the experiments with an MLO depth of 0.1 m, especially if the revised climate sensitivities including the effect of energy leakage are considered (calculated according to Equation 12).

The tendencies of the feedback factors, which were calculated with the PRP module (Mauritsen et al., 2013), are quite different (Figure 35). For an MLO depth of 50 m, all feedbacks decrease with increasing evaporation resistance, though the slope changes (Figure 29). In contrast to that, the lapse rate feedback increases in magnitude for rsoil $\leqslant 3$ and the water vapor feedback even increases up to rsoil = 15. The increase of both feedbacks is related to the

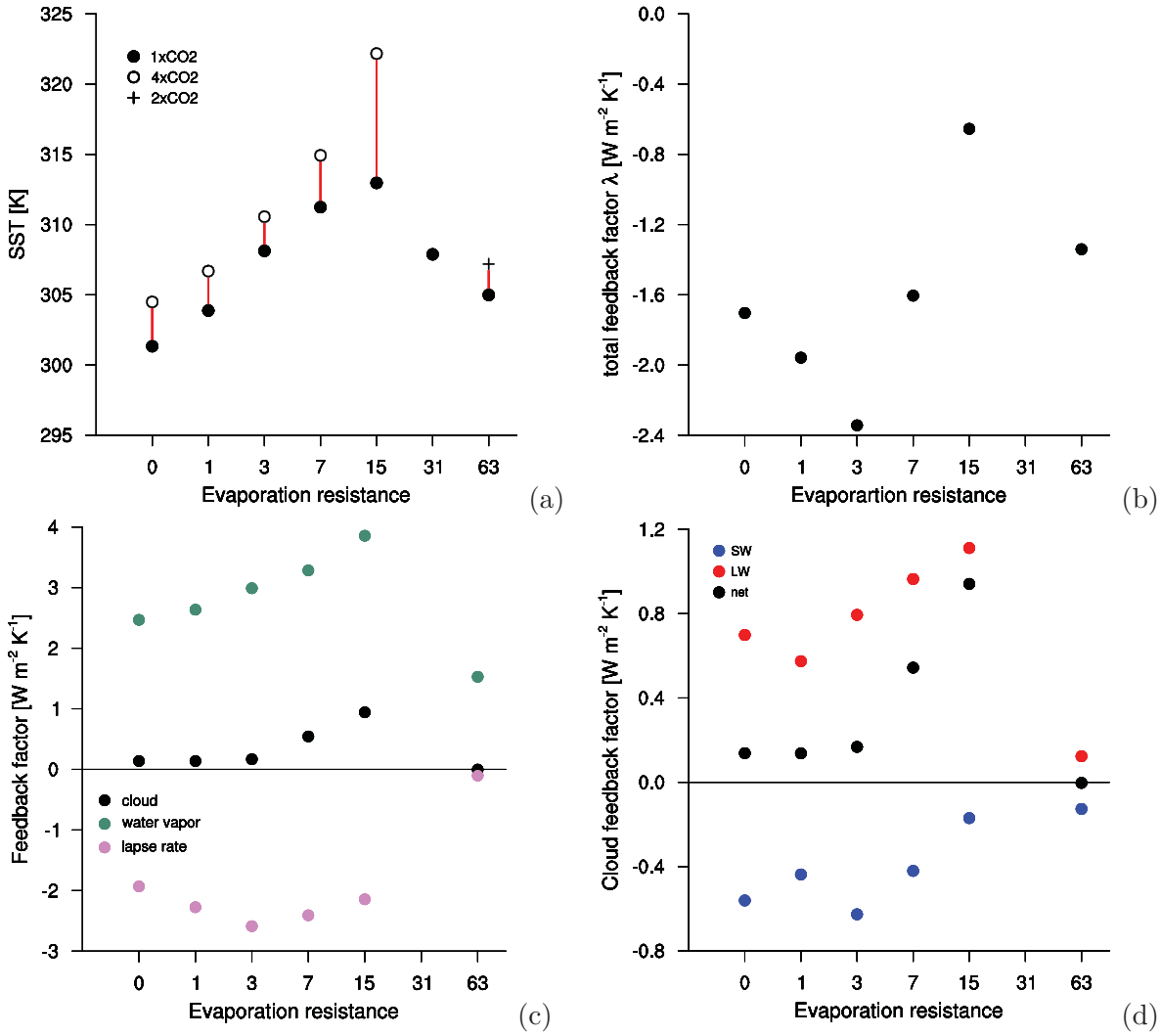

Figure 35: Equilibrium mean SSTs of the experiments with preindustrial and quadrupled CO_2 concentrations (a), the total feedback factor λ (b), the contribution of the net feedback factors (c) and the distribution of the cloud feedback factor in shortwave and longwave feedback factors (d) for the experiments with an MLO depth of 0.1 m and different evaporation resistances.

strong SST increase and especially the even stronger increase of daily maximum temperatures which trigger deep convection. Consequently, the moist adiabat and water vapor concentration both change.

The ECS decreases for rsoil $\leqslant 3$ because the increase of the negative lapse rate feedback slightly dominates the increase of water vapor feedback. For rsoil $\leqslant 3$, the cloud feedback factor does not change at all because there are no boundary layer clouds in any of the experiments. Furthermore, the transition to a single cluster climate occurs both for control and quadrupled CO_2 concentrations at rsoil $= 3$, so there is no cloud feedback related to this transition. As a

consequence of the simultaneous transition, the overturning circulation does not increase in any 4xCO$_2$ experiment relative to the control experiment, which is visualized in Figure 36.

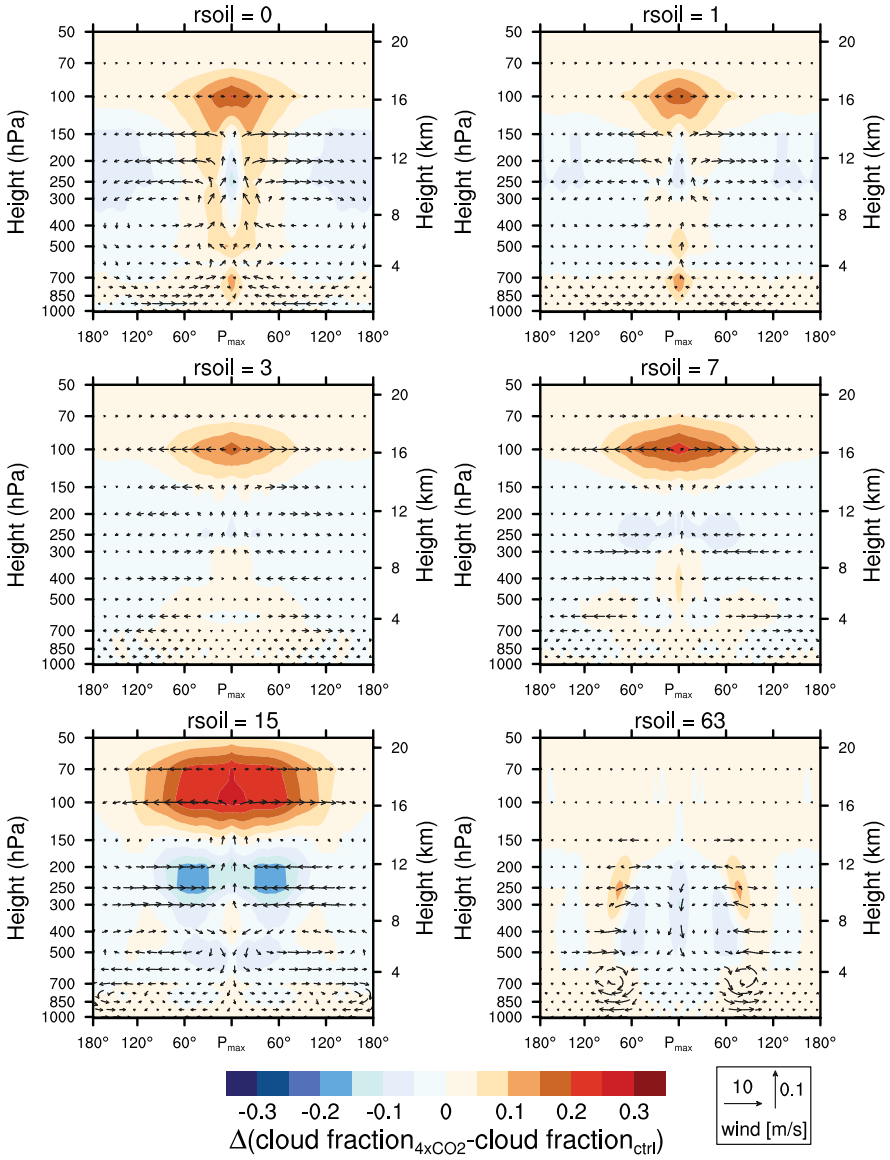

Figure 36: Vertical cross sections of the change of cloud fraction and wind field when quadrupling CO_2 concentrations for an MLO depth of 0.1 m and for evaporation resistance values of 0, 1, 3, 7, 15 and 63. The data is averaged analogously to Figure 26.

The strong increase of ECS from rsoil = 3 to rsoil = 15 can be related to an increase of water vapor and cloud feedback and to a decrease of the negative lapse rate feedback. Hence, all depicted feedback factors contribute to the ECS increase. Lapse rate feedback and water vapor feedback changes do not cancel each other in this case because the vertically integrated water vapor increases in the 4xCO$_2$ experiments from 63 to 103 kg m^{-2} although the relative

humidity decreases (Figure 32 and Figure A.7 in the Appendix). The increase of cloud feedback can be related both to an increase of longwave feedback and to a decrease of the negative shortwave cloud feedback. The latter one decreases because the atmosphere dries especially below 600 hPa, which is where the shortwave cloud feedback dominates. The increase of the longwave cloud feedback can be explained with a strong increase of cloud fraction between 70 and 100 hPa (Figure 36) because the tropopause height is elevated to the 70 hPa level in the $4xCO_2$ experiment with rsoil = 15 (Appendix Figure A.7).

For rsoil $\geqslant$ 15, all feedback factors strongly decrease. The water vapor feedback decrease dominates the lapse rate feedback decrease and the cloud feedback reduces to zero, as the atmosphere both dries and cools. Hence, for rsoil $\geqslant$ 15, the tendencies are equivalent for the 50 m and 0.1 m experiment series. Nonetheless, the climate transition is very strong and the instability of the $4xCO_2$ experiments indicates that the climate is close to a runaway climate.

Another issue is that deep convection and therefore all feedback factors couple to daily maximum temperatures. Climate sensitivities regarding daily maximum temperatures are smaller than on the daily mean if the diurnal cycle is strong, as already shown in Figure 21. Hence, the magnitude of the feedbacks scaled with daily maximum temperatures would be somewhat larger. Nevertheless, this does not change when increasing evaporation resistance and thus this fact is only of minor importance in this section.

5 RCE climate with idealized continents

With the ECHAM-RCE setup, it is also possible to vary the MLO depth and evaporation resistance within the model, so some regions are specified with different surface characteristics than others. However, the surface boundary conditions become heterogeneous, so the equilibrium is not anymore purely radiative-convective because there is an influence of the large-scale circulation. Nevertheless, such a model is quite interesting to analyze. Cronin and Emanuel (2012) did a similar study with a CRM, changing only the heat capacity of the surface. Their idealized island has a 5 cm deep slab ocean which is surrounded by a 1 m deep ocean. Their main result is that the precipitation over the idealized island almost doubles.

In the experiments which are presented in this section, the MLO depth is reduced from 50 m to 0.1 m and the evaporation resistance is enhanced to rsoil = 15 in the area of the idealized continent. The area of the idealized continent encompasses 15 grid points latitudinal (56.25°) and 11 grid points longitudinal (41.25°), centered at the equator. In one experiment, every grid point with land is completely surrounded by ocean, so the continent becomes an idealized Maritime Continent. In the other experiment, the continent is homogeneous and is called for simplicity North Africa because it has approximately the size of North Africa. Figure 37 gives a first impression what the resulting climate looks like. Temperatures are highest over the idealized continents, leading to surface wind convergence and, especially over the Maritime Continent, to enhanced precipitation. The inhomogeneities over the ocean are due to a not sufficiently long averaging period.

	North Africa			Maritime Continent			
	continent	ocean	global	land	continent	ocean	global
SST [K]	305.8	300.4	300.7	305.6	302.3	300.6	300.7
P [mm/d]	6.0	3.9	4.0	4.6	7.2	4.0	4.2

Table 14: Equilibrium SST and precipitation (P) over idealized continents shaped like North Africa and the Maritime Continent and over the ocean. The ocean between the islands of the Maritime Continent is regarded as part of the continent.

In both experiments, the land surface is approximately 5 K warmer than the ocean (Table 14) because of the increased evaporation resistance. Nonetheless, the surface is more than 6 K cooler than in the experiment with the same land properties all over the globe (0.1 m MLO depth and rsoil = 15, Table 12). Since the shape of the idealized continents is so different, the dominant mechanism leading to the similar surface temperatures cannot be temperature

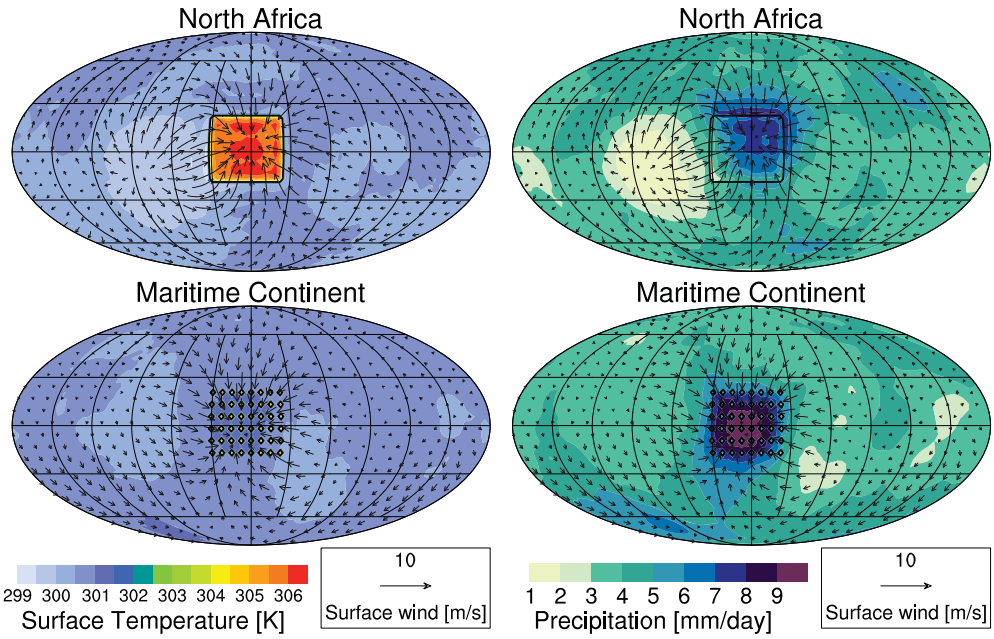

Figure 37: Mean field of surface temperature (left) and precipitation (right) together with the surface wind field for all time steps in equilibrium.

advection from the cold ocean. Instead, the similar surface temperatures can be explained with internal gravity waves, spreading perturbations very efficiently all over the sphere since there is no Coriolis force. Consequently, the upper-tropospheric temperatures over continent and ocean are almost indistinguishable (Figure 38). Besides, a comparison of cloud forcing at TOA reveals that clouds have a cooling effect over the idealized continents (-14 $\mathrm{W\,m^{-2}}$ over North Africa and -12 $\mathrm{W\,m^{-2}}$ over the land of the Maritime Continent), but in the experiment with the idealized land surface everywhere, clouds have a warming effect of 3 $\mathrm{W\,m^{-2}}$ because high clouds dominate due to the dry low troposphere.

Another very interesting feature of the resulting climate is that 600 hPa level clouds are pronounced over the idealized continents, although these clouds are not evident over the ocean between the islands of the Maritime Continent. Instead, there are boundary layer clouds in this area. Since the islands have the same vertical profile of relative humidity as the ocean grid points between the islands (Figure 38), the decrease of 600 hPa clouds is not related to the relative humidity profile. Instead, the 600 hPa clouds are triggered by the strong diurnal cycle over land. As their persistence is so short, they are independent of the cloud fraction over the ocean between the islands. The clouds in 300 hPa persist much longer, which is one reason why the cloud fraction is the same over the islands and over the ocean between the islands.

An important characteristic of island climate is land-sea-breeze. On earth, an island is warmer during the day and colder at night, so there is convergence of surface wind over the island during the day and divergence at night. However, Table 15 shows that it is warmer

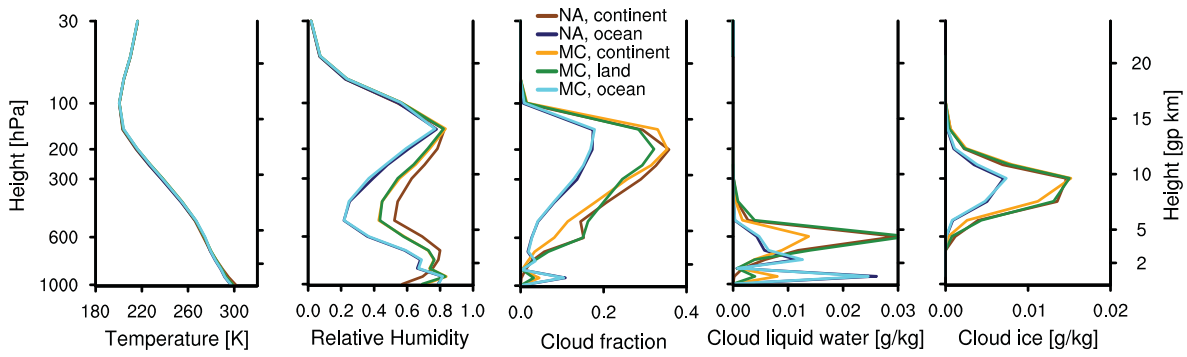

Figure 38: Vertical equilibrium profiles of atmospheric properties over the idealized continents North Africa (NA) and the Maritime Continent (MC). The regions are defined identical to Table 14.

over the idealized continents than over the surrounding ocean at every time of day as the enhanced evaporation resistance inhibits efficient cooling. Consequently, there is always surface convergence over the idealized continents. Over the idealized continent shaped like North Africa, precipitation peaks in the afternoon, as one would expect from an idealized continent. Yet over the Maritime Continent, precipitation peaks at night, which is typical over the ocean. The reason is that the area covered with land is quite small, so although the most precipitation occurs there in the afternoon (8.0 mm/d), the ocean grid points in between the islands still dominate overall. The precipitation is strongest at these grid points because they profit on the one hand from the nearby warm islands which cause large-scale surface convergence over the Maritime Continent and on the other hand from high latent heat fluxes because evaporation is not restricted.

	North Africa				Maritime Continent			
Time of Day	3	9	15	21	3	9	15	21
SST [K]	300.6	302.7	313.7	306.2	300.7	301.4	304.8	302.6
P [mm/d]	4.7	5.2	7.7	6.3	7.7	6.4	7.0	7.7
ω [hPa/d]	-35	-25	-35	-43	-27	-24	-26	-28

Table 15: SST, precipitation (P) and mass-weighted vertical velocity (ω) over idealized continents shaped like North Africa and the Maritime Continent for different times of day. The data is averaged over 6 hours, so e.g. 3 corresponds to times between 0:00 and 6:00. The ocean between the islands of the Maritime Continent is regarded as part of the land.

6 Summary, conclusion and outlook

In an attempt to better understand the different responses of land and ocean climates to changing greenhouse gas concentrations, the comprehensive general circulation model ECHAM6 has been modified to simulate RCE. The modifications include turning off the rotation of the planet, specifying spatially homogeneous solar insolation and defining a mixed-layer ocean without ocean heat transport as lower boundary. In the control setup, the ocean is 50 m deep. Some additional minor changes ensure spatially homogeneous boundary conditions. Hence, the radiative-convective equilibrium climate is determined by the fully fledged GCM physics package.

The model setup matches the ECHAM6-RCE composition used by Popke et al. (2013) to determine the influence of the convection scheme and the role of the hydrological cycle. However, Popke et al. (2013) did not only use an older model version (ECHAM-6.0.13), but also an enhanced resolution (T63L47) and decreased forecast time step (450 s). In this study, simulations are performed with ECHAM-6.1.05 with a time step of 900 s and low resolution (T31L47). In this way, the computational costs of one experiment are relatively small. 48 experiments are carried out in order to investigate the influence of thermodynamic surface properties on climate and climate change, thereof 27 with preindustrial, 20 with quadrupled and one with doubled CO_2 concentrations.

On earth, the assumptions and simplifications of RCE are most appropriate in the tropics because Coriolis force and horizontal temperature gradients are weak. A comparison of RCE climate and CMIP5 climate simulations with ECHAM6 reveals that all significant features of the tropical atmosphere are well reproduced by RCE. This includes the atmospheric temperature profile and a bimodal vertical relative humidity distribution characterized by high near-surface and upper-tropospheric humidities with a dry mid troposphere in between. Furthermore, cloud and condensate profiles are also well reproduced, with one peak near 900 hPa and another near 700 hPa. These main climate features are preserved in low resolution (T31L47). Although cluster size and autocorrelation of mass-weighted vertical velocity increase compared to T63 experiments, a resolution dependence of the vertical atmospheric profiles is not evident. In addition, the equilibrium climate sensitivities agree well, with 2.2 K in T31 and 2.1 K in T63 (Popke et al., 2013). However, this is only half of the climate sensitivity of the full model and also less than the climate sensitivity over the tropical ocean. This can partly be explained with low-cloud feedbacks, which are substantially weaker in RCE (Popke et al., 2013).

Since the SST is not fixed, regionally inhomogeneous surface temperatures develop, either due to radiative effects of clouds and convection or due to perturbed turbulent fluxes of latent or sensible heat. Consequently, convection aggregates in regions of high SSTs because the atmosphere is least stratified there. Due to the negative net cloud radiative effect, the surface below the cloud cools and the cluster propagates to another, warmer region or dissipates. The rising motion in the convective regions is balanced by subsidence in wide areas, forming an overturning circulation with surface winds from the subsidence to the convective areas which are of similar magnitude as on earth in the tropics.

A decrease of MLO depth both alters the coupling to the atmosphere and increases the daily SST amplitude. The influence of the increased coupling is investigated with an experiment series without a diurnal cycle. The SST distribution broadens if the MLO depth is reduced to 1 m, but does not change much if the MLO depth is reduced further. Consequently, the inertness of a 1 m deep MLO is already so small that SSTs can adapt to all radiative imbalances. Nevertheless, there is no evidence that this enhanced coupling of SSTs and convection alters RCE climate, especially since the vertical profiles of atmospheric properties are almost identical and climate sensitivity does not change much.

On the contrary, the diurnal cycle has no effect on atmospheric processes for an MLO depth of 1 m or larger. While the diurnal SST range is smaller than 2 K with a 1 m deep ocean, the diurnal SST ranges by 11 K with a 0.1 m deep ocean and by 15 K with a 0.02 m deep ocean. Hence, convection is triggered during the day and the precipitation maximum is not only moved from nighttime to daytime, but also increases in amplitude. For a 0.1 m deep MLO, precipitation peaks in the afternoon, as one would expect in the tropics over land. However, if the MLO depth is further decreased to 0.02 m, the peak is shifted to the morning because already in the morning, convection is so strong that most condensate precipitates. This is a common problem in GCMs which is related to the inability of GCMs to reproduce the gradual growth of deep clouds (Bechtold et al., 2004).

Global mean surface temperature and climate sensitivity are more or less independent of the MLO depth as long as the ocean is at least 1 m deep. When the diurnal SST cycle starts altering atmospheric processes, the boundary layer height increases and the moisture is mixed through a deeper layer, leading to a dissipation of boundary layer clouds. Since low clouds have a strong negative shortwave radiative effect, the dissipation of boundary layer clouds leads to a 1.5 K SST increase and to a one-off decrease of climate sensitivity as boundary layer clouds only exist in the control experiments. Another consequence of the boundary layer cloud dissipation is that the radiative effect of clouds above the boundary layer increases, especially in the subsidence regime. A positive feedback mechanism evolves in which 700 hPa clouds induce a temperature inversion and their negative radiative effect leads to surface cooling, amplifying the inversion. For an MLO depth of less than 0.1 m, this feedback mechanism dominates the cloud dissipation effect of dry and warm subsiding air. Consequently, a negatively skewed

SST distribution is observed and the global mean SST decreases by 2.7 K. Since the cloud tops cool less effectively in a more opaque atmosphere, the feedback mechanism is weaker with quadrupled CO_2 concentrations and climate sensitivity increases. DTR decreases if CO_2 concentrations increase because a more opaque atmosphere can cool less efficiently at night, while maximum temperatures are coupled to convection and do not increase so much.

After reducing the heat capacity of the surface, an artificial resistance rsoil that partially suppresses evaporation from the ocean is introduced as a second step towards a "land-like" planet. The resultant decrease of latent heat flux is primarily balanced by an increase of net shortwave radiation, and secondary by an increase of sensible heat flux. Consequently, precipitation decreases and the Bowen ratio increases, reaching "land-like" values for rsoil $\geqslant 3$. For small evaporation resistances, rising surface temperatures lead to an increase of net shortwave radiation. For rsoil > 15, surface temperatures drop again because longwave back radiation of the atmosphere decreases due to a reduction of water vapor concentrations and therefore of opaqueness. In response to the increase of evaporation resistance, relative humidity decreases below 600 hPa, the atmospheric lapse rate approaches the dry adiabat, the tropopause height drops and the amount of cloud liquid water in the atmosphere reduces strongly while cloud ice amount does not change.

The horizontal distribution of atmospheric properties changes for rsoil $\geqslant 3$ because a transition to a climate with only one precipitation cluster occurs, leading to a drying in the subsidence regime. In the convective regime, a cold pool builds up in the low troposphere due to virga, moistening and cooling the air. Consequently, surface convergence does not occur in the center of the cluster, but at its edges. The self-aggregation is not related to an upgradient transport of moist static energy by the mean flow, though there might be an upgradient transport by eddies. The most important trigger of self-aggregation is probably the strongly increasing net cloud radiative effect of the atmosphere, a source of moist static energy in the convective regime. Beyond that, it cannot be excluded that self-aggregation mainly occurs because surface temperatures increase. In this regard, it would be interesting to know whether convection still aggregates in an experiment with rsoil $= 127$, or whether the expected SST decrease opposes self-aggregation. In any case, it would be interesting to analyze the influence of evaporation resistance without strong surface temperature adaptations. With interactive SSTs, one solution would be an adjustment of surface albedo.

The climate sensitivity evolution with increasing evaporation resistance can be divided in three sections. In the first section, climate sensitivity decreases because cloud feedback reduces since boundary layer clouds disappear in the control experiments. In the second section, climate sensitivity increases because the reduction of the negative lapse rate feedback dominates. In the third section, climate sensitivity decreases again because the decreasing water vapor feedback dominates. Water vapor and lapse rate feedback are not necessarily closely coupled because the lapse rate feedback is dominated by changes of the moist adiabat

in the low troposphere, while water vapor is of the highest radiative importance in the upper troposphere.

The combination of an MLO depth of 0.1 m with increasing evaporation resistance does not lead to fundamentally different results. The diurnal temperature range increases from 11 K to 18 K due to the drying of the atmosphere and due to the reduction of latent heat fluxes. Climate sensitivity evolves similar to the experiments with a 50 m deep MLO, although the feedbacks which are responsible for this evolution change.

Concerning the real tropics over land, it can be concluded that climate change has the potential to be strongest in semi-arid regions, at least if advection and internal gravity waves have little influence on the atmospheric profiles. The influence of internal gravity waves is proportional to the Rossby radius of deformation. Hence, Coriolis force needs to be sufficiently strong, which requires some distance from the equator.

With idealized continents, convection predominantly occurs over the continent or rather over the ocean between the islands of the Maritime Continent. Due to the model configuration, the surface of the idealized continents is warmer than the ocean at every time of day, leading to convergence of surface wind over the island all the time. The surface is more than 6 K cooler in comparison to the experiment with the same land properties all over the globe. This is not directly related to advection, but to internal gravity waves and a change of the CRE. A very interesting question is whether the change of CRE and therefore of surface temperature is only related to the transport of moisture from the large ocean area to the continent, or whether the surface temperature would also decrease so much if the Maritime Continent covered the whole globe. With such a model setup, the influence of surface inhomogeneities in general could be analyzed.

This study demonstrates that RCE is a very interesting framework for studying tropical climate in an idealized setup, at least in locations where advection does not dominate the atmospheric properties. Even if that is not the case, RCE simulations can help to disentangle the influence of radiative-convective and large-scale dynamical processes. Besides, RCE simulations can be used for various case studies like investigating the influence of certain surface properties or of self-aggregation on climate in a GCM. A better understanding of self-aggregation on a global scale could also lead to a better understanding of the Madden-Julian Oscillation (MJO). Thus, RCE simulations enhance understanding both of atmospheric processes and of model behavior. Because of the simple setup, RCE experiments are well suited for model intercomparison studies and they have the potential to close the gap between LES and GCM simulations, making it easier to improve GCM parameterizations of convection with LES simulations.

A Additional Figures

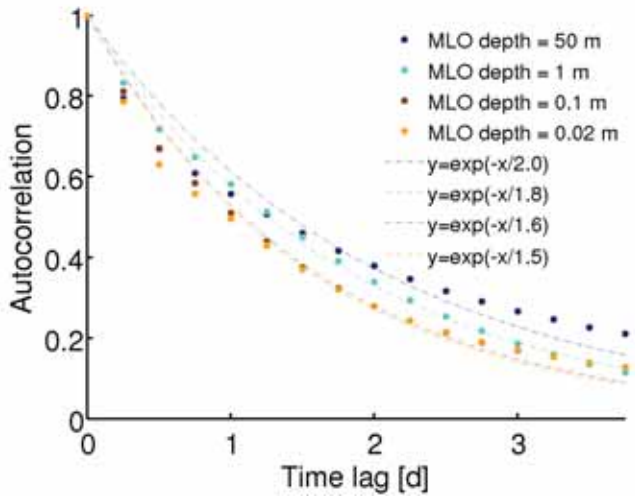

Figure A.1: Autocorrelation function of the mass-weighted vertical velocity with 6 hourly data for different MLO depths without a diurnal cycle of solar insolation. From the sample for the first four days, the best fitting exponential decay functions are calculated with the least squares method.

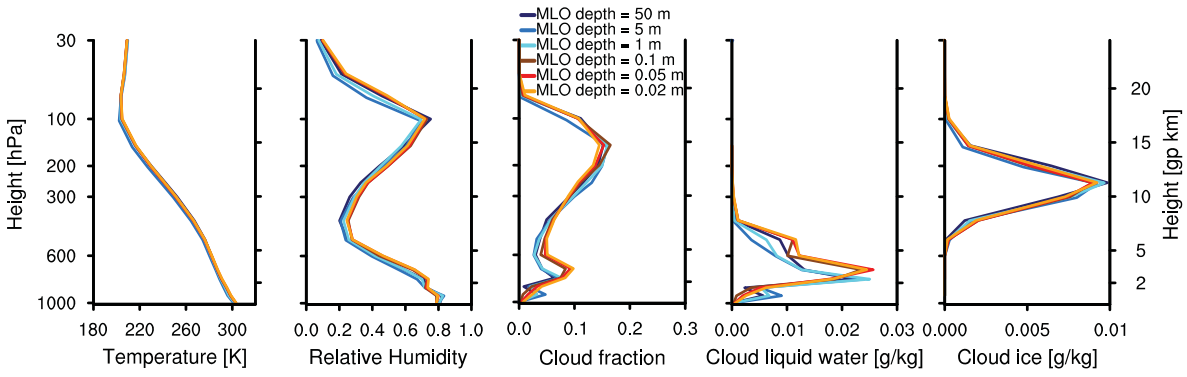

Figure A.2: Vertical equilibrium profiles of atmospheric properties in the experiments with quadrupled CO_2 concentrations for different MLO depths.

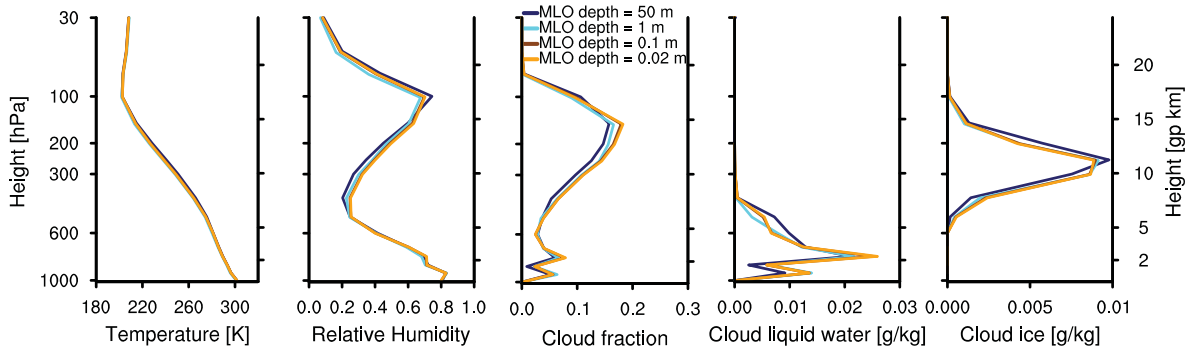

Figure A.3: Vertical equilibrium profiles of atmospheric properties in the experiments with quadrupled CO_2 concentrations and without a diurnal cycle for different MLO depths.

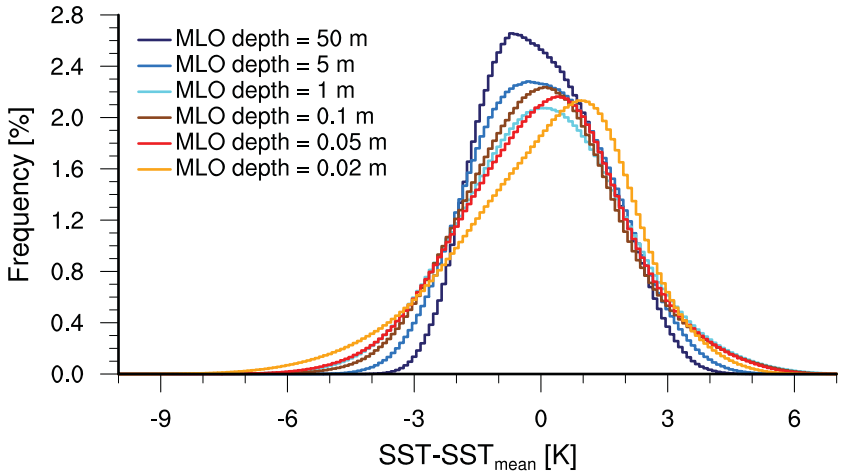

Figure A.4: Histogram of daily averaged SST perturbations at all grid points relative to the global mean value for different mixed layer ocean depths (50 m, 5 m, 1 m, 0.1 m, 0.05 m and 0.02 m) of the experiments with a diurnal cycle and quadrupled CO_2 concentrations, considering only the time period in equilibrium. Each grid point is weighted by its area. The bin size is 0.1 K.

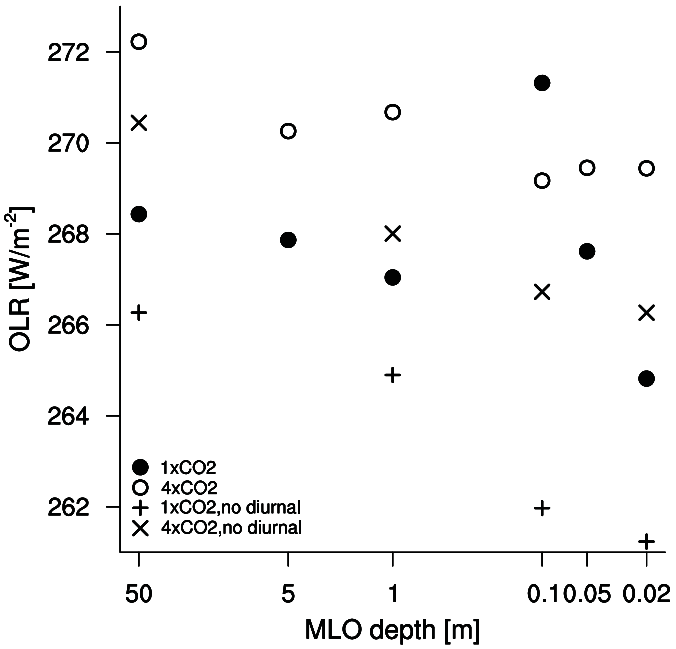

Figure A.5: Equilibrium mean outgoing longwave radiation (OLR) of the experiments with preindustrial and quadrupled CO_2 concentrations for different MLO depths on a logarithmic scale. The experiment series with and without a diurnal cycle are both presented.

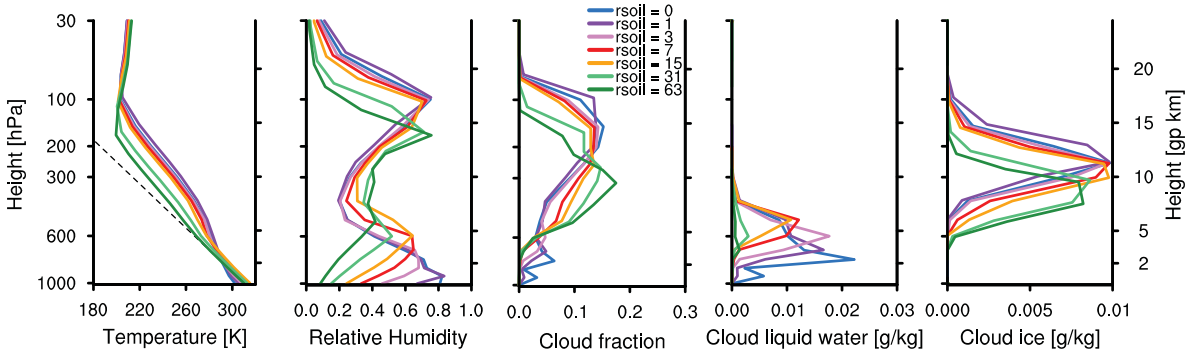

Figure A.6: Vertical equilibrium profiles of atmospheric properties in the experiments with quadrupled CO_2 concentrations, with an MLO depth of 50 m and with different evaporation resistances. The black dashed line in the temperature profile represents the dry adiabatic lapse rate, starting at the surface temperature of the experiment with rsoil = 63.

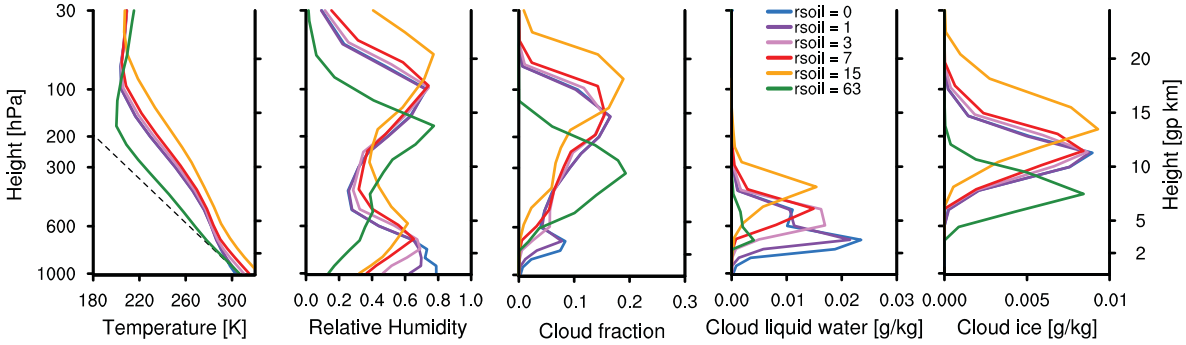

Figure A.7: Vertical equilibrium profiles of atmospheric properties in the experiments with an MLO depth of 0.1 m and with different evaporation resistances. The CO_2 concentrations are quadrupled for rsoil $\leqslant 15$ and doubled for rsoil $= 63$. The black dashed line in the temperature profile represents the dry adiabatic lapse rate, starting at the surface temperature of the experiment with rsoil $= 63$.

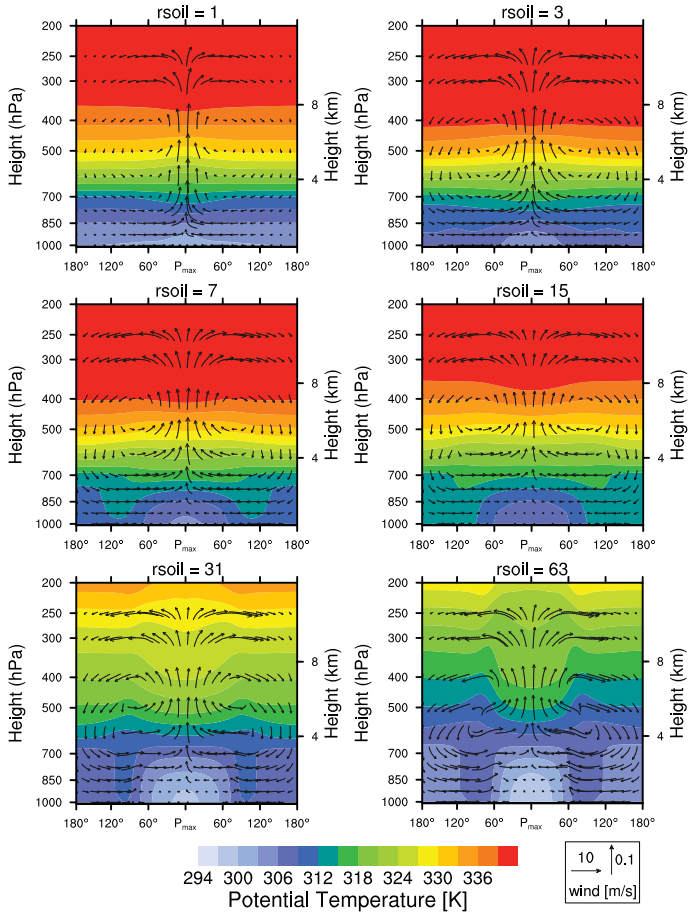

Figure A.8: Vertical cross sections of mean potential temperature and wind field for an MLO depth of 0.1 m and evaporation resistance values of 1, 3, 7, 15, 31 and 63. The data is averaged analogously to Figure 26.

List of Figures

List of Tables

References

Bechtold, P., J.-P. Chaboureau, A. Beljaars, A. K. Betts, M. Köhler, M. Miller, and J.-L. Redelsperger (2004). The simulation of the diurnal cycle of convective precipitation over land in a global model. *Quarterly Journal of the Royal Meteorological Society* 130.604, pp. 3119–3137.

Bony, S., B. Stevens, I. H. Held, J. F. Mitchell, J.-L. Dufresne, K. A. Emanuel, P. Friedlingstein, S. Griffies, and C. Senior (2013a). Carbon Dioxide and Climate: Perspectives on a Scientific Assessment. *Climate Science for Serving Society.* Ed. by G. R. Asrar and J. W. Hurrell. Springer, pp. 391–413.

Bony, S., G. Bellon, D. Klocke, S. Sherwood, S. Fermepin, and S. Denvil (2013b). Robust direct effect of carbon dioxide on tropical circulation and regional precipitation. *Nature Geoscience* 6.6, pp. 447–451.

Bowen, I. S. (1926). The Ratio of Heat Losses by Conduction and by Evaporation from any Water Surface. *Physical Review* 27 (6), pp. 779–787.

Bowman, K. P., J. C. Collier, G. R. North, Q. Y. Wu, E. H. Ha, and J. Hardin (2005). Diurnal cycle of tropical precipitation in Tropical Rainfall Measuring Mission (TRMM) satellite and ocean buoy rain gauge data. *Journal of Geophysical Research* 110.D21.

Cao, H. X., J. F. B. Mitchell, and J. R. Lavery (1992). Simulated diurnal range and variability of surface temperature in a global climate model for present and doubled CO2 climates. *Journal of Climate* 5 (9), pp. 920–943.

Chandrasekhar, S. (1957). *An Introduction in the Study of Stellar Structure.* Dover.

Cronin, T. W. and K. A. Emanuel (2012). Rectification of the diurnal cycle over small islands in radiative-convective equilibrium. *Extended Abstracts, 30th Conf. on Hurricanes and Tropical Meteorology.* Ponte Vedra Beach, FL, Amer. Meteor. Soc., P3.8.

Giorgetta, M. A., J. Jungclaus, C. H. Reick, S. Legutke, J. Bader, M. Boettinger, et al. (2013). Climate and carbon cycle changes from 1850 to 2100 in MPI-ESM simulations for the

coupled model intercomparison project phase 5. *Journal of Advances in Modeling Earth Systems* 5.3, pp. 572–597.

Hartmann, D. L. and K. Larson (2002). An important constraint on tropical cloud - climate feedback. *Geophysical Research Letters* 29.20, pp. 12–1–12–4.

Held, I. M. (2005). The Gap between Simulation and Understanding in Climate Modeling. *Bulletin of the American Meteorological Society* 86.11, pp. 1609–1614.

Held, I. M. and B. J. Soden (2006). Robust Responses of the Hydrological Cycle to Global Warming. *Journal of Climate* 19, pp. 5686–5699.

Held, I. M., M. Zhao, and B. Wyman (2007). Dynamic radiative-convective equilibria using GCM column physics. *Journal of the Atmospheric Sciences* 64.1, pp. 228–238.

Iacono, M. J., J. S. Delamere, E. J. Mlawer, M. W. Shephard, S. A. Clough, and W. D. Collins (2008). Radiative forcing by long-lived greenhouse gases: Calculations with the AER radiative transfer models. *Journal of Geophysical Research-Atmospheres* 113.D13.

Jackson, L. S. and P. M. Forster (2010). An Empirical Study of Geographic and Seasonal Variations in Diurnal Temperature Range. *Journal of Climate* 23.12, pp. 3205–3221.

Joshi, M. M., J. M. Gregory, M. J. Webb, D. M. H. Sexton, and T. C. Johns (2008). Mechanisms for the land/sea warming contrast exhibited by simulations of climate change. *Climate Dynamics* 30.5, pp. 455–465.

Khairoutdinov, M. F. and K. A. Emanuel (2010). Aggregated convection and the regulation of tropical climate. *Extended Abstracts, 29th Conf. on Hurricanes and Tropical Meteorology*. Tucson, AZ, Amer. Meteor. Soc., P2.69.

Klocke, D., J. Quaas, and B. Stevens (2013). Assessment of different metrics for physical climate feedbacks. *Climate Dynamics* 41.5-6, pp. 1173–1185.

Kraus, E. B. (1963). The diurnal precipitation change over the sea. *Journal of the Atmospheric Sciences* 20.6, pp. 551–556.

Lawrence, D. M. and J. M. Slingo (2005). Weak land-atmosphere coupling strength in HadAM3: The role of soil moisture variability. *Journal of Hydrometeorology* 6.5, pp. 670–680.

Lindzen, R. S., A. Y. Hou, and B. F. Farrell (1982). The role of convective model choice in calculating the climate impact of doubling CO2. *Journal of the Atmospheric Sciences* 39.6, pp. 1189–1205.

Lohmann, U. and E. Roeckner (1996). Design and performance of a new cloud microphysics scheme developed for the ECHAM general circulation model. *Climate Dynamics* 12.8, pp. 557–572.

Manabe, S. and R. F. Strickler (1964). Thermal equilibrium of the atmosphere with a convective adjustment. *Journal of the Atmospheric Sciences* 21.4, pp. 361–385.

Manabe, S. and R. T. Wetherald (1967). Thermal Equilibrium of the Atmosphere with A Given Distribution of Relative Humidity. *Journal of the Atmospheric Sciences* 24.3, pp. 241–259.

Mauritsen, T., B. Stevens, E. Roeckner, T. Crueger, M. Esch, M. A. Giorgetta, H. Haak, J. H. Jungclaus, D. Klocke, D. Matei, U. Mikolajewicz, D. Notz, R. Pincus, H. Schmidt, and L Tomassini (2012). Tuning the climate of a gobal model. *Journal of Advances in Modeling Earth Systems* 4.M00A01.

Mauritsen, T., R. G. Graversen, D. Klocke, P. L. Langen, B. Stevens, and L. Tomassini (2013). Climate feedback efficiency and synergy. *Climate Dynamics* 41.9-10, pp. 2539–2554.

Möbis, B. and B. Stevens (2012). Factors controlling the position of the Intertropical Convergence Zone on an aquaplanet. *Journal of Advances in Modeling Earth Systems* 4.M00A04.

Muller, C. J. and I. M. Held (2012). Detailed Investigation of the Self-Aggregation of Convection in Cloud-Resolving Simulations. *Journal of the Atmospheric Sciences* 69.8, pp. 2551–2565.

Nordeng, T. E. (1994). Extended versions of the convective parameterization scheme at ECMWF and their impact on the mean and transient activity of the model in the tropics. *Tech. Rep. ECMWF* 206.

Popke, D. (2012). Climate, climate change and the constraints on precipitation in a radiative-convective equilibrium version of ECHAM6. *Master thesis,* Max Planck Institute for Meteorology, University of Hamburg, Hamburg.

Popke, D., B. Stevens, and A. Voigt (2013). Climate and climate change in a radiative convective equilibrium version of ECHAM6. *Journal of Advances in Modeling Earth Systems* 5.1, pp. 1–14.

Ramanathan, V. and J. A. Coakley (1978). Climate Modeling Through Radiative-Convective Models. *Reviews of Geophysics and Space Physics* 16.4, pp. 465–489.

Roeckner, E., L. Duemenil, E. Kirk, F. Lunkeit, M. Ponater, B. Rockel, R. Sausen, and U. Schlese (1989). The Hamburg version of the ECMWF model (ECHAM). *Research Activities in Atmospheric and Oceanic Modelling* WMO/TD-322.

Roeckner, E., G. Bäuml, L. Bonaventura, R. Brokopf, M. Esch, M. Giorgetta, S. Hagemann, I. Kirchner, L. Kornblueh, E. Manzini, A. Rhodin, U. Schlese, U. Schulzweida, and A. Tompkins (2003). The atmospheric general circulation model ECHAM5 - Part I. *Report* 349.

Soden, B. J., A. J. Broccoli, and R. S. Hemler (2004). On the use of cloud forcing to estimate cloud feedback. English. *Journal of Climate* 17.19, pp. 3661–3665.

Stevens, B. and S. Bony (2013). What Are Climate Models Missing?. *Science* 340.6136, pp. 1053–1054. eprint: `http://www.sciencemag.org/content/340/6136/1053.full.pdf`.

Stevens, B., M. Giorgetta, M. Esch, T. Mauritsen, T. Crueger, S. Rast, et al. (2013). Atmospheric component of the MPI-M Earth System Model: ECHAM6. *Journal of Advances in Modeling Earth Systems* 5.2, pp. 146–172.

Stocker, T. (2011). *Introduction to Climate Modelling*. Ed. by K. Hutter. Advances in Geophysical and Environmental Mechanics and Mathematics. Springer.

Sundqvist, H., E. Berge, and J. E. Kristjansson (1989). Condensation and Cloud Parameterization studies with a mesoscale numerical weather prediction model. *Monthly Weather Review* 117.8, pp. 1641–1657.

Tiedtke, M. (1989). A Comprehensive Mass Flux Scheme For Cumulus Parameterization in Large-Scale Models. *Monthly Weather Review* 117.8, pp. 1779–1800.

Tobin, I., S. Bony, and R. Roca (2012). Observational Evidence for Relationships between the Degree of Aggregation of Deep Convection, Water Vapor, Surface Fluxes, and Radiation. *Journal of Climate* 25, pp. 6885–6904.

Tompkins, A. M. and G. C. Craig (1998a). Radiative-convective equilibrium in a three-dimensional cloud-ensemble model. *Quarterly Journal of the Royal Meteorological Society* 124.550, pp. 2073–2097.

– (1998b). Time-scales of adjustment to radiative-convective equilibrium in the tropical atmosphere. *Quarterly Journal of the Royal Meteorological Society* 124.552, B, pp. 2693–2713.

Wetherald, R. T. and S. Manabe (1988). Cloud feedback processes in a general circulation model. *Journal of the Atmospheric Sciences* 45, pp. 1397–1416.

Danksagung

Ich danke Bjorn Stevens und Jürgen Bader für die erstklassige Betreuung meiner Masterarbeit, für all die guten Ideen, Hinweise, Ratschläge und Denkanstöße, die sich im Laufe vielfältiger Diskussionen ergeben haben, sowie für die Einführung in die wissenschaftliche Gemeinde, nicht nur innerhalb des Max Planck Instituts für Meteorologie, sondern auch darüber hinaus, zum Beispiel bei der EUCLIPSE Konferenz. Thorsten Mauritsen und den anderen Mitgliedern der Climate Dynamics Gruppe danke ich für die inspirierenden und horizonterweiternden Diskussionen während unserer Gruppentreffen. Außerdem danke ich Thorsten für die Implementierung der PRP Methode in ECHAM und die hilfreichen Erklärungen dazu. Ein großes Dankeschön geht an Dagmar Popke, nicht nur für die ausgezeichnete Arbeit, auf der meine Masterarbeit aufbaut, sondern auch für all die Hilfe, die schon vor meinem Studium bei der Wahl meines Studienortes angefangen hat. Für hilfreiche Kommentare und gute Ideen bezüglich self-aggregation danke ich Cathy Hohenegger und Caroline Muller. Für die ausgezeichnete Einführung in ECHAM und die eine oder andere Hilfestellung während meiner Arbeit danke ich Sebastian Rast und für die Lösung aller organisatorischer Probleme danke ich Angela Gruber. Malte Rieck und Katrin Lonitz danke ich nicht nur für die angenehme Atmosphäre im Büro, sondern auch für all die kleinen Tipps und Hilfestellungen.

Ich danke meiner ganzen Familie und insbesondere meinen Eltern für die bedingungslose Unterstützung und klugen Ratschläge, nicht nur während meiner Masterarbeit, sondern während meines gesamten Studiums. Die Sicherheit, ein finanziell sorgenfreies Studium absolvieren zu können, ist ebenfalls nicht hoch genug anzurechnen.

Ich danke dem Meteorologischen Institut der Universität Hamburg für ein reibungsfreies Studium und insbesondere für die Ermöglichung des Auslandaufenthalts an der University of Oklahoma in einem Austauschprogramm. Meinem Semester danke ich für die unglaublich vielseitigen und spannenden fünf Jahre, aus denen sich viele Freundschaften entwickelt haben, die sicher auch noch lange halten werden. Danke auch für die vielen entspannten und kurzweiligen Mittagspausen, die für den nötigen Ausgleich zur Arbeit gesorgt haben. Last but not least danke ich Hoyke und Marvin für die tolle Zeit in der WG, die durchaus auch von der ein oder anderen wissenschaftlichen Diskussion geprägt war und fast zur Gründung einer eigenen Partei geführt hätte.

Erklärung zur Eigenständigkeit

Ich versichere, dass ich diese Arbeit selbstständig verfasst habe und keine anderen als die angegebenen Hilfsmittel benutzt habe - insbesondere keine im Literaturverzichnis nicht aufgeführten Internet-Quellen. Die Arbeit habe ich in keinem weiteren Prüfungsverfahren eingereicht. Die eingereichte schriftliche Fassung entspricht der auf dem elektrionischen Speichermedium.

Ich stimme einer Veröffentlichung dieser Arbeit in der Institutsbibliothek zu.

Tobias Becker	Ort, Datum

Die gesamten Veröffentlichungen in der Publikationsreihe des MPI-M
„Berichte zur Erdsystemforschung“,
„Reports on Earth System Science“,
ISSN 1614-1199

sind über die Internetseiten des Max-Planck-Instituts für Meteorologie erhältlich:

http://www.mpimet.mpg.de/wissenschaft/publikationen.html